The Search for Stellar Coronal Mass Ejections

Thesis by
Jackie Villadsen

In Partial Fulfillment of the Requirements for the
degree of
Doctor of Philosophy

CALIFORNIA INSTITUTE OF TECHNOLOGY
Pasadena, California

2017
Defended December 16, 2016

Jackie Villadsen
ORCID: 0000-0003-3924-243X

ACKNOWLEDGEMENTS

Thank you to my advisor, Gregg Hallinan, for being an enthusiastic and generous advisor, a champion of all of your students, and an example of the sort of mentor I would like to be. You are good at identifying and praising what your students are doing well, which was a very effective source of motivation for me. I would also like to thank Tony Readhead, my advisor for my first two years at Caltech, whose enthusiasm for science attracted me to Caltech and to radio astronomy. Thank you to Lynne Hillenbrand, for chairing my thesis committee, for helpful conversations, and for your support for the astronomy grad students. I would like to thank the other members of my candidacy and thesis committees, Judy Cohen, Shri Kulkarni, Tim Pearson, Sterl Phinney, and Dave Stevenson, for their enthusiasm and advice.

Thank you to Caltech staff for your helpfulness and generosity with your time: Althea, Anu, Cresilda, Efrain, Gita, Patrick, Sandy L., and everyone at the Caltech libraries, the graduate office (especially the thesis proofreader!), Center for Diversity, and Center for Teaching, Learning, Learning and Outreach. Thank you also to the many staff and visitors to the Owens Valley Radio Observatory who taught me radio astronomy and made it feel like home, including Cecil, Dale, Dan, Dave H., Dave W., Dick, Erik, Gelu, James, Kjell, Lori, Mark, Mary, Nikolaus, Russ, Sarah, and Stephen M. My research at Caltech and OVRO has been enabled by funding from the NSF Graduate Research Fellowship Program, the Starburst project NSF grant, the Troesh family's graduate fellowship, and the PEO International Scholar Awards. Thank you especially to local PEO members for their encouragement.

My time at Caltech was enriched by helpful conversations and support from many people, including my mentors Laura and Katey and my mentees Becky, Katie, and Lori; my productivity support group Erik, Sam, and Sunita; and Mandy. Thanks to my graduate class, Mike B., Sebastian, and Sirio, for being the people I would want to take with me to start a Mars colony; to my office mates, Allison and Gina, for closed-door conversations and everything you do to help other people; and to all the Caltech astronomy grad students, for taking me into your tight-knit community. Thanks to my fellow Readhead group members, who helped me get started in radio astronomy, including Chris, Jennifer, Kieran, Matthew, and Walter. Thanks to my Hallinan group members and stellar astronomy collaborators, including Sandy W., Stephen B., Navtej, Manuel, Michael R., Loko, and Moira. And my ardent thanks go to my fellow Hallinan students and friends, Kunal, Marin, Melodie, Michael E.,

Ryan, and Sebastian, who each deserve their own paragraph: Kunal for reminding me to stay level-headed, Marin for long chats about feminism and grad school and cats, Melodie for her generosity with supportive actions and sweet words, Michael for making everyone laugh, and Ryan for making my thesis possible. Thanks to Sebastian, especially, who has been my next-desk neighbor since first year, a generous, sincere friend who is always good for thoughtful conversations.

Completing my PhD is my biggest accomplishment to date. Something else that I am proud of, which happened concurrently, is mentoring a youth group focused on spirituality and community service. The youth and mentors of this group all mean so much to me: Genesis D., Angel, Jamileth, Itzel, Genesis C., Karla, Jose R., Jose Jr., Ian, Garrison. I would also like to thank other friends who have been part of heartfelt conversations about spirituality, including Jean, Lydia, Halima, Nina, Kurt, Bayan, Fiona, Stephanie and Jan, Tamar, Masha, Kunal, and Melodie. These conversations often touched on the role that the Bahá'í Faith has played in my life as a source of motivation for studying science. The Bahái teachings state, "The virtues of humanity are many but science is the most noble of them all.... God has created or deposited this love of reality in man." It has been a delight at Caltech to be among intellectually thirsty people who exemplify this love of reality.

Thank you to my roommates: Sunita, for being the person I talk to about everything; Sarah, for cat co-parenting, long conversations, and board games; Chengyun, for stargazing trips, excellent cooking, and Pokéwalks; and Snug and Gigi, for being our lovable and mischievous feline friends. Thank you to Masha (who was never my roommate but everyone thought she was) for spontaneous adventures and keeping me from taking myself too seriously. Thanks to Lauren and Tony as well for the wonderful three months that I lived with each of you, and thank you to Jean for taking in my cat for three months and being my thesis buddy. Thank you also to my friends who watched my favorite TV show with me (the Bachelor/ette), including Lauren, Katy, Tamar, Anna, Shannon, Masha, Melissa, Melodie, and Mike L.

Finally, I would like to thank my family: my grandparents, aunts, uncles, and cousins, many of whom share my enthusiasm for science and all of whom I love to spend time with. Thanks to my younger brother Andrew, for the love you show our family and for your thoughtful way of looking at the world. Thanks most of all to my parents, Glenn and Nancy, for encouraging me to take the harder physics class in high school, for sacrificing sleep and retirement savings for my education, and for even now dropping everything on a moment's notice to come support me.

ABSTRACT

Coronal mass ejections (CMEs) may dramatically impact habitability and atmospheric composition of planets around magnetically active stars, including young solar analogs and many M dwarfs. Theoretical predictions of such effects are limited by the lack of observations of stellar CMEs. This thesis addresses this gap through a search for the spectral and spatial radio signatures of CMEs on active M dwarfs.

Solar CMEs produce radio bursts with a distinctive spectral signature, narrow-band plasma emission that drifts to lower frequency as a CME expands outward. To search for analogous events on nearby stars, I worked on system design, software, and commissioning for the Starburst project, a wideband single-baseline radio interferometry backend dedicated to stellar observations. In addition, I led a survey of nearby active M dwarfs with the Karl G. Jansky Very Large Array (VLA), detecting coherent radio bursts in 13 out of 23 epochs, over a total of 58 hours. This survey's ultra-wide bandwidth (0.23-6.0 GHz) dynamic spectroscopy, unprecedented for stellar observations, revealed diverse behavior in the time-frequency plane. Flare star UV Ceti produced complex, luminous events reminiscent of brown dwarf aurorae; AD Leo sustained long-duration, intense, narrow-band "storms"; and YZ CMi emitted a burst with substructure with rapid frequency drift, resembling solar Type III bursts, which are attributed to electrons moving at speeds of order 10% of the speed of light.

To search for the spatial signature of CMEs, I led 8.5-GHz observations with the Very Long Baseline Array simultaneous to 24 hours of the VLA survey. This program detected non-thermal continuum emission from the stars in all epochs, as well as continuum flares on AD Leo and coherent bursts on UV Ceti, enabling measurement of the spatial offset between flaring and quiescent emission.

These observations demonstrate the diversity of stellar transients that can be expected in time-domain radio surveys, especially with the advent of large low-frequency radio telescopes. Wide bandwidth radio dynamic spectroscopy, complemented by high-resolution imaging of the radio corona, is a powerful technique for detecting stellar eruptions and characterizing dynamic processes in the stellar corona.

PUBLISHED CONTENT AND CONTRIBUTIONS

Villadsen, J., Hallinan, G., Bourke, S., Güdel, M., & Rupen, M. 2014, ApJ, 788, 112, 112, DOI: 10.1088/0004-637X/788/2/112, arXiv: 1405.2341 [astro-ph.SR], URL: http://adsabs.harvard.edu/abs/2014ApJ...788..112V, Reproduced by permission of the AAS. J.R.V. prepared the observing scripts for this project, conducted the data analysis, and wrote the manuscript.

TABLE OF CONTENTS

LIST OF ILLUSTRATIONS

LIST OF TABLES

Chapter 1

INTRODUCTION

On September 1, 1859, Richard Carrington and Richard Hodgson were observing sunspots at noon when they saw a blinding arc grow between the dark spots, the first observed solar flare. Late that night, a massive disturbance was recorded in Earth's magnetic field, and brilliant aurorae, bright enough to read by, lit up the sky even in equatorial countries such as Colombia. Decades later, the missing link between solar flares and magnetic storms on Earth became clear: coronal mass ejections (CMEs), eruptions of magnetized plasma from the outer solar atmosphere. White light from the Sun scatters off of CMEs, making them visible during eclipses and with solar coronagraphs. The discovery of CMEs in white light occurred in the early 1970s with the solar coronagraph on Skylab (MacQueen et al. 1974). Prior to this, radio spectroscopic observations had found evidence of sources propagating outward through the solar corona at speeds of thousands of km/s (solar Type II radio bursts, Wild et al. 1954) and the Culgoora radioheliograph had imaged coronal radio sources moving away from the Sun at comparable speeds (Figure 1.1, Riddle 1970). These observations came together into a coherent picture when solar type II radio bursts were found to be associated with the shock fronts formed by fast-moving coronal mass ejections (Gosling et al. 1976). These radio bursts are a means of detecting CMEs, signposts of the magnetic interaction between the Sun and Earth.

1.1 Impact of stellar activity on stellar evolution and planetary habitability

Solar flares and CMEs often occur together, especially for the most energetic events. The probability that a solar flare has an associated CME increases with the flare's intensity and duration, reaching 100% for the most energetic flares (Harrison 1995; Yashiro & Gopalswamy 2009). Magnetically active stars flare regularly with energy greater than the most energetic observed solar flare (10^{32} ergs in blue and UV light, Scalo et al. 2007), suggesting that they may also have a high rate of CMEs. Drake et al. (2013) and Osten & Wolk (2015) extend the observed solar flare-CME association rate to predict the CME mass loss rate of active stars, finding that it implies astronomical mass loss rates for active M dwarfs of 10^{-11} $M_\odot$/yr (1000 times the solar wind and 0.1 $M_\star$ over 3 Gyr) and would require some active stars to convert up to 10% of their luminosity into kinetic energy of stellar eruptions. Aarnio et al.

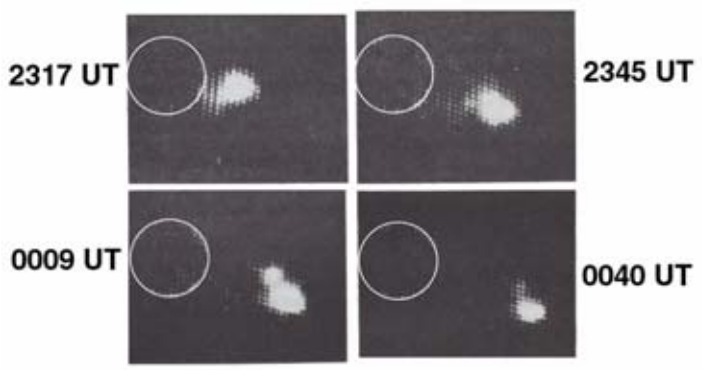

Figure 1.1 Culgoora radioheliograph images of an 80-MHz radio source moving away from the Sun (Riddle 1970) that predated the discovery of coronal mass ejections using a white light coronagraph. Figure from Howard (2006): copyright 2006 by the American Geophysical Union, reproduced with permission from publisher John Wiley and Sons, all rights reserved.

(2013) apply solar scaling relations to X-ray flare rates of young stars to predict that CMEs may control angular momentum evolution for pre-main sequence stars.

Stellar eruptions may have dramatic consequences for habitability and atmospheric composition of extrasolar planets. This is particularly the case for planets around M dwarfs, since M dwarfs spin down slowly compared to more massive stars, retaining their youthful strong magnetic activity for hundreds of millions of years to billions of years (West et al. 2008), long enough to shape the long-term evolution of planetary atmospheres. Based on the flare rate of active M dwarfs, they may produce CMEs at such a prodigious rate that the magnetosphere of an Earth-like planet would be permanently compressed by pressure from the CMEs down to almost the planet's surface (Khodachenko et al. 2007), enabling planetary atmospheres to be entirely eroded by CME-induced ion pickup (Lammer et al. 2007). If a planet manages to escape that fate, it would still be exposed to the strong energetic radiation associated with monthly 10^{34} erg flares (extrapolating flare rates from Lacy et al. 1976), and if such flares are associated with CMEs, protons accelerated at the CME shock fronts will interact chemically with the planetary atmospheres to almost entirely deplete ozone, exposing the planetary surface to a high flux of energetic radiation (Segura et al. 2010).

These predictions of the effects of stellar CMEs on stellar evolution and planetary habitability all rely on extrapolating relationships between solar flares and CMEs to apply to the extremely energetic flares of active stars, which occur in the context of

a much stronger stellar magnetic field. Extrapolation across flare energy, magnetic field strength, and dynamo type (for fully convective mid to late M dwarfs, compared to the partially convective Sun) is an inherently uncertain process, testing the limits of the solar-stellar connection. In the Sun, active regions with strong overlying magnetic fields are responsible for the few extremely energetic flares that have occurred without accompanying CMEs (Thalmann et al. 2016), suggesting that the strong magnetic fields of active stars may prevent stellar eruptions. Wood et al. (2005) measure stellar mass loss rates for nearby active stars that are lower than the solar mass loss rate, in contradiction to the flare-based predictions of Osten & Wolk (2015). This result suggests that the strong magnetic field of active stars may suppress stellar mass loss (Vidotto et al. 2016), or that the mass loss from active stars is highly directional, so that it was not detected by the line-of-sight Lyman α absorption measurements of Wood et al. (2005).

1.2 Magnetic activity of low-mass stars

The magnetic fields of low-mass main sequence stars are generated by dynamos, which rely on the presence of a convecting, conductive fluid in the outer layer of the star. The depth of the outer convective zone becomes deeper from spectral type F to M, until at mid-M, stars are fully convective. Fully convective stars require a different type of dynamo than the Sun's $\alpha - \Omega$ dynamo, which is rooted in the tachocline, the interface between the solid radiative core and the differentially rotating convective layer. Spectropolarimetric observations of fully convective mid M dwarfs indicate that, compared to partially convective stars, they have a greater fraction of their magnetic flux in the large-scale field (Reiners & Basri 2009a), in configurations that are stable on timescales of at least a year (Morin et al. 2008). These observations find that the large-scale magnetic fields of late M dwarfs fall in one of two distinct morphologies: strong (kilo-Gauss) axisymmetric dipolar fields (similar to the reconstructed large-scale field of mid-M dwarf V374 Peg shown in Figure 1.2) or weak non-axisymmetric fields (Morin et al. 2010), suggesting either that the fully convective dynamo causes stars to cycle between these two morphologies, or that the dynamo is bistable, causing a star to reside in one of the two states long-term. It is still an open question whether fully convective stars and substellar objects undergo polarity reversals and if so, how often this occurs and whether it is cyclic or chaotic. The possibility of long-term stability in the magnetic field configuration of fully convective stars is supported by photometric variability observations of mid-M dwarf V374 Peg that suggest its spot configuration is stable

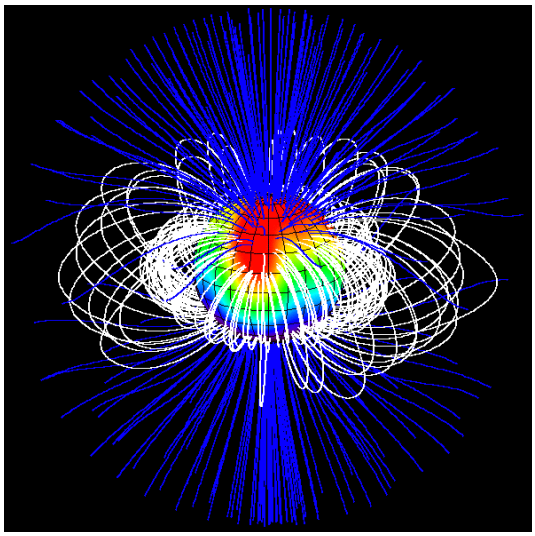

Figure 1.2 3D reconstruction by Moira Jardine of the large-scale magnetic field structure of M4 dwarf V374 Peg based on Zeeman Doppler Imaging by Donati et al. (2006).

over 16 years (Vida et al. 2016). Kitchatinov et al. (2014) argue that fully convective low-mass stars should have a long magnetic cycle, of order 100 years, due to their long magnetic diffusion timescale. In contrast, Route (2016) infers magnetic polarity reversals on a number of ultracool dwarfs based on changes in the sense of circular polarization of radio bursts. The sense of circular polarization of coherent radio bursts depends on the longitudinal (line of sight) magnetic field polarity in the source region, making coherent radio bursts a means of tracing magnetic field evolution.

The magnetic properties of stars are traced using both direct measurements of magnetic field properties via Zeeman splitting and radio polarization, and observations of the magnetic activity powered by the magnetic fields. In the former category (magnetic field measurements) are Zeeman splitting and radio polarization.

- *Zeeman splitting* (reviewed in Donati & Landstreet 2009): Measurements of magnetically-sensitive line splitting in Stokes I are sensitive to line-of-sight magnetic field amplitude averaged across the stellar disk, and in Stokes V are sensitive to net line-of-sight magnetic flux across the stellar disk, with regions of opposite polarity canceling out. Analysis of the Stokes I line profile is used to characterize the distribution of magnetic field strengths on the stellar surface (Shulyak et al. 2014), and periodic variation of the Stokes V line

profile as magnetic features rotate across the star is used to map stars' large-scale magnetic field in a technique known as Zeeman Doppler Imaging (ZDI).

- *Radio polarization* (reviewed in Dulk 1985): In the magnetized atmospheres of stars, transverse electromagnetic radiation separates into the o (ordinary) mode, whose dispersion relation is unaffected by interaction with the magnetic field, and the x (extraordinary) mode, which does interact with the magnetic field. This results in different opacities for the two modes for a number of emission mechanisms, so that magnetic field strength and direction can be measured from the polarization of incoherent continuum including free-free, gyroresonance (cyclotron), and gyrosynchrotron (mildly-relativistic synchrotron) emission. It also results in different growth rates for the two wave modes for coherent emission mechanisms, plasma radiation and the electron cyclotron maser, resulting in circular polarization of up to 100%. The o and x modes translate into circularly polarized emission, with the relationship between x and o mode and sense of circular polarization depending on the magnetic field orientation, so that magnetic field orientation and strength can be inferred from the combination of observing frequency and degree and sense of circular polarization.

- *Magnetic activity indicators*: Stellar emission that is powered by magnetic fields can be used to track time variation in the spatial distribution and strength of stellar magnetic fields. Such activity indicators are found across the electromagnetic spectrum, including but not limited to: emission lines from the hot chromosphere such as Hα and CaII H&K, thermal X-ray emission from hot coronal material confined by the star's magnetic field, photometric variability due to magnetic spot coverage, and intensity of thermal gyroresonance emission, which traces the coverage of magnetized coronal hotspots above active regions.

1.3 Radio emission from the Sun and stars

Radio emission from the Sun was first discovered during WWII independently by British, American, and Australian military radar engineers (Hey 1946; Southworth 1945; Orchiston 2005), although radio experiments to detect the Sun started as early as the late 1800s (Wilsing & Scheiner 1896). Even in quiescence the Sun is one of the brightest radio sources in the sky, with fluxes ranging from 10^4 to 10^6 Jy in the 0.1-1 GHz range. In contrast to optical flares, radio flares can increase the solar

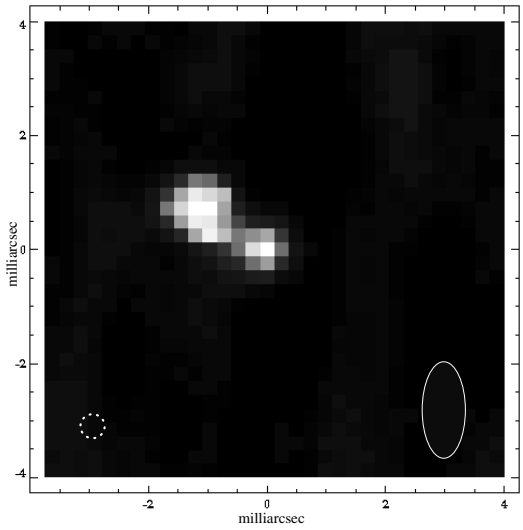

Figure 1.3 VLBI image of UV Ceti's 8.4-GHz flaring radio corona (Benz et al. 1998). The two emission lobes are separated by 4 photospheric diameters, requiring a strong large-scale stellar magnetic field to enable the mildly relativistic gyromagnetic emission at these high frequencies at such large heights above the photosphere. Credit: Arnold Benz, John Conway, and Manuel Güdel, A&A, vol. 331, p. 596-600, 1998, reproduced with permission © ESO.

radio flux by factors of 10 to 100 (and even more at lower frequencies).

Radio emission from the Sun and low-mass stars is powered by magnetic activity. Radio wavelengths become optically thick in the Sun's hot outer atmosphere, the heating of which is mediated by the Sun's magnetic field. Different wavelengths become opaque at different heights due to a number of types of opacity, so that multi-wavelength radio observations can be used to track the temperature, magnetic field strength and density across a wide range of heights in the outer solar atmosphere. Chapter 2 of this thesis (Villadsen et al. 2014) presents the first detection of thermal microwave emission from solar-type, low-activity stars, with brightness temperatures of 10^4 K at 35 GHz, consistent with the quiet Sun at those frequencies, which is a nearly uniform disk that becomes optically thick in the 10^4 K chromosphere due to free-free opacity. Even though the high-frequency Sun is normally extremely homogenous and quiet, dominated by thermal emission, the Sun surprisingly produces rare flares at sub-mm wavelengths, whose emission mechanism is not well understood (Krucker et al. 2013). Most solar radio flares above 1 GHz have weak circular polarization if any and broad spectral shape, generally attributed to gyrosynchrotron emission from non-thermal electrons. The timescale for non-thermal

electrons to thermalize through collisions is seconds (Dulk 1985), with the result that non-thermal flaring emission only persists as long as there is ongoing electron acceleration, which occurs at the magnetic reconnection site during flares. This is reflected by the Neupert effect (Sun: Neupert 1968; flare stars: e.g. Guedel et al. 1996), which states that the radio emission released in flares is the derivative of the soft X-ray emission, where the radio emission originates from non-thermal electrons accelerated by the flare, and the soft X-ray emission comes from material that is heated to coronal temperatures by collisions with the non-thermal electrons then cools gradually. In contrast to the Sun, where non-thermal centimeter emission is seen only during flares, magnetically active stars sustain continuous non-thermal radio emission, attributed to incoherent gyrosynchrotron, which is correlated with the stars' X-ray luminosity (Gudel et al. 1993). The same correlation, the Güdel-Benz relation, applies to solar flares and quiescent emission from active stars (Benz & Güdel 1994a), lending support to the hypothesis that the "quiescent" radio and X-ray emission from the coronae of active stars may be composed of a superposition of many flares. Very long baseline imaging sometimes resolves the non-thermal emission from the quiescent and slowly flaring radio coronae of active M dwarfs, detecting structures the size of multiple photospheric diameters, revealing that the non-thermal electron population is (at least sometimes) confined in the large-scale stellar magnetosphere. For example, Figure 1.3 shows the 8.4-GHz radio corona of M6 dwarf UV Ceti observed by Benz et al. (1998), which was resolved into two lobes with opposite circular polarization, separated by 4 stellar diameters.

At low radio frequencies (below 1-2 GHz on the Sun, 5-10 GHz on magnetically active stars), radio bursts with a coherent emission mechanism are common. The coherent emission mechanisms known to operate in the Sun and stars are plasma emission and electron cyclotron maser (ECM) emission, which produce radiation at low harmonics of the plasma frequency and the electron cyclotron frequency, respectively. Due to the dependence of emission frequency on local plasma conditions (density and/or magnetic field strength), evolution of the coherent emission spectrum over time can be used to trace source motion through different regions of the corona.

Dynamic spectra are used to highlight the evolution of spectral features of solar radio bursts over time. Figure 1.4 illustrates the dynamic spectrum of various types of solar radio bursts. Solar radio bursts are caused by high-energy electrons that have been accelerated at the site of magnetic reconnection. Coherent radio bursts

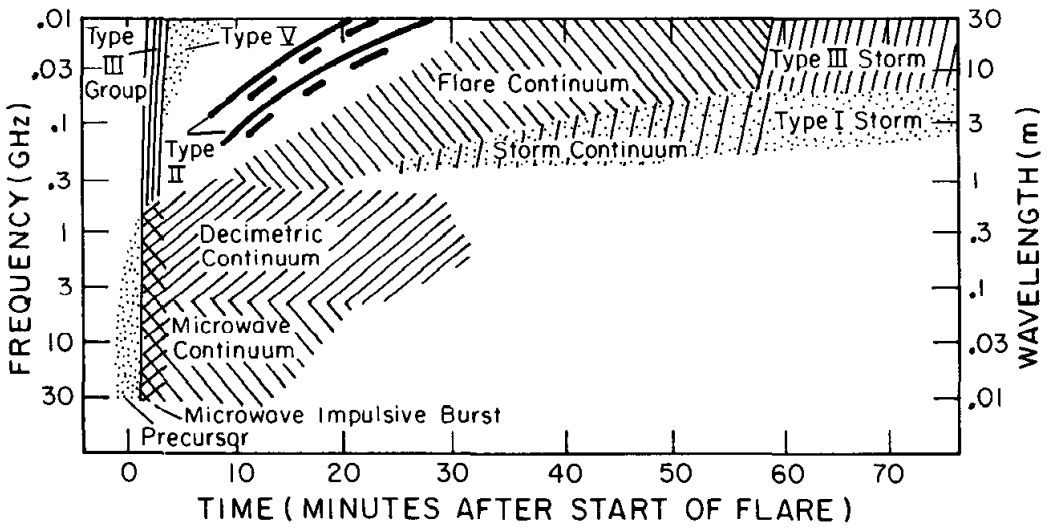

Figure 1.4 Cartoon illustrating the various types of radio bursts that may occur as part of a solar flare event. Two forms of coherent radio bursts of particular interest here are Type III (short-duration bursts that sweep quickly in frequency, produced by electron beams associated at the magnetic reconnection site) and Type II (long-duration bursts produced by electron beams accelerated at a shock as it moves outwards through the corona). Figure reproduced from Dulk (1985), copyright 1985 by Annual Reviews.

(solar type II and III bursts) occur because higher-energy electrons stream ahead of slower electrons, forming an electron beam. In the electron beam, there are more electrons at high energies than low energies, resulting in an inverted velocity distribution function $f(v)$ that satisfies the condition $df/dv > 0$ necessary to produce coherent emission (this is known as a bump-in-the-tail instability). Such electron beams can also form from ambient electrons reflecting off of a shock front (fast Fermi acceleration). Solar coronal mass ejections form a shock if their velocity is higher than the Alfvén speed, which is true for the majority of CMEs. Figure 1.5 shows the dynamic spectrum of the Type II solar radio burst associated with an exceptionally energetic CME.

1.4 Interpretation of dynamic spectra of coherent radio bursts

[This section is also included as part of the paper draft in Chapter 4.]

Interpretation of the dynamic spectra of stellar coherent radio bursts hinges on three interrelated questions: 1) What is the emission mechanism, plasma radiation or electron cyclotron maser? 2) Is frequency drift in the dynamic spectrum due to

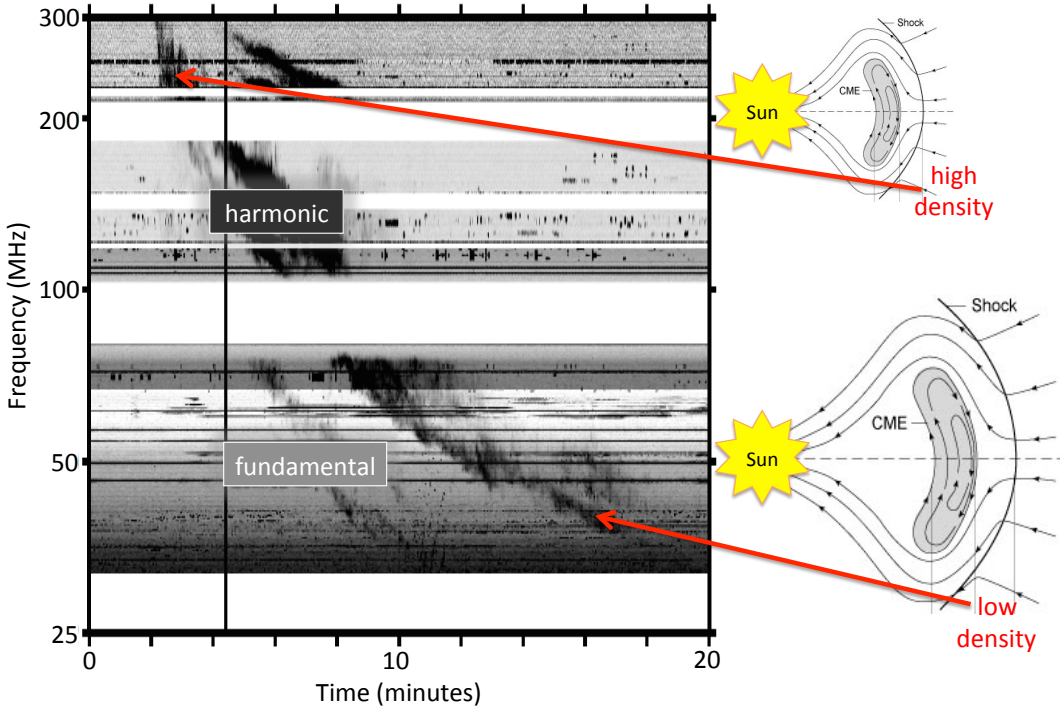

Figure 1.5 Dynamic spectrum, adapted from Kouloumvakos et al. (2014), of a solar Type II radio burst associated with a coronal mass ejection. The emission is produced at low harmonics of the plasma density upstream of the CME shock. As the CME expands outwards from the Sun, it moves into lower ambient plasma densities, exciting emission at lower frequencies. The frequency drift rate is used to measure the CME speed.

Caption in original publication: Combined dynamic spectra of ARTEMIS IV and RSTN (San Vito) in the 25-300 MHz range; the fundamental and the harmonic of the Type-II burst are annotated with II(F) and II(H), respectively. The Type-II bands below the II(H) in the range 275-300 MHz were found to be an artefact due to the non-linear response of the ARTEMIS IV pre-amplifier which introduced an image of II(H) displaced by 100 MHz. (The horizontal black stripes are interference from terrestrial emitters; the white stripes are disturbed frequency ranges that have been suppressed.)

source motion or to rotational modulation of highly-beamed emission? 3) Is the supply of high-energy electrons powering the emission stochastic (flares) or continuous (an auroral current system)? This section addresses the first two of these questions in greater detail.

1.4.1 Emission Mechanism

The two emission mechanisms responsible for stellar coherent radio bursts are plasma emission and electron cyclotron maser emission (ECM). The electron cyclotron maser is expected to amplify emission at the fundamental cyclotron frequency only when the ratio of plasma frequency to cyclotron frequency, $\Xi = \nu_p/\nu_c$, is less than one, and at the second harmonic of the cyclotron frequency for $\Xi < 1.4$ (Melrose et al. 1984; Winglee 1985). This condition is not met in most of the solar corona, except for low heights above strongly magnetized active regions (Morosan et al. 2016), so plasma emission is the dominant mechanism for low-frequency solar coherent radio bursts. ECM is responsible for some of the higher-frequency (GHz+) solar bursts and for planetary radio aurorae. High brightness-temperature periodic radio emission, attributed to ECM, is also observed on some brown dwarfs (e.g. Hallinan et al. 2008) and on the magnetic A star CU Virginis (Trigilio et al. 2011).

Observational signatures that can be used to distinguish between the two mechanisms include:

- **Frequency.** Plasma emission is limited to low frequencies due to free-free absorption, with hotter coronal temperatures pushing the cutoff to higher frequencies. For plasma emission at harmonic s, $\nu = s\nu_p \propto \sqrt{n_e}$, the free-free opacity can be written in terms of the observing frequency in GHz $\nu_{\rm GHz}$, the temperature in MK T_6, and the density scale length H along the path of the emission:

$$\tau_{\rm ff} = 46\ s^{-4}\ \nu_{\rm GHz}^2\ T_6^{-3/2} \left(\frac{H}{30\ {\rm Mm}}\right). \tag{1.1}$$

  Assuming a high coronal temperature of 10^7 K and a low density scale height of 30 Mm, plasma emission at the fundamental harmonic sees $\tau_{\rm ff} = 3$ at 1.4 GHz, and the second harmonic at 5.6 GHz. In contrast, the Sun's 10^6 K corona limits fundamental and harmonic plasma emission to roughly 250 MHz and 1 GHz, respectively. However, as noted by Osten & Bastian (2006), gyroresonance absorption by higher harmonics poses a problem for ECM

emission, especially in the hot coronae of flare stars, since gyroresonant opacity increases with temperature. It may be the case that both plasma emission and ECM must be emitted from a region with a sharp density gradient in order to have a low enough overlying opacity to escape from a stellar atmosphere.

- **Brightness temperature.** Coherent wave growth saturates at a brightness temperature that is dependent on emission mechanism (Melrose 1991). The theoretical predictions are roughly consistent with the range of brightness temperatures observed for plasma emission (low-frequency solar bursts: 10^8–10^{15} K, Dulk 1985) and ECM (Jupiter's decametric radiation: $> 10^{17}$ K, Dulk 1970).

- **Degree and sense of circular polarization.** Plasma emission at the fundamental is expected to be in the o-mode; the second harmonic is most often unpolarized but sometimes observed with weak o-mode polarization that is predicted not to exceed roughly 50% (Melrose et al. 1978). Combined with the constraint of free-free absorption that limits fundamental plasma emission to less than 1-2 GHz, this implies that strongly polarized emission above 2 GHz is likely produced by ECM. ECM, in the low-density limit, should be dominated by emission at the fundamental frequency in the x-mode, which can be fully circularly polarized. Propagating outwards from a north magnetic pole, o-mode corresponds to left circular polarization, and x-mode to right circular polarization.

- **Harmonic structure.** Both emission mechanisms can produce emission at the fundamental or second harmonic, although second harmonic emission is observed more commonly for plasma emission. For plasma emission, the coherent wave growth typically occurs in Langmuir waves, plasma density oscillations which cannot be radiated directly from the plasma. Instead a Langmuir wave must coalesce with another wave to produce transverse electromagnetic waves that can escape the plasma. Coalescence of a Langmuir wave and low-frequency turbulence produces emission at the fundamental frequency, whereas coalescence of two Langmuir waves produces second harmonic emission. These two processes can saturate at similar brightness temperatures, so that first and second harmonic are sometimes observed together at similar intensities in solar radio bursts; while the second harmonic is only weakly polarized, it is in the same sense as the first harmonic (Melrose et al. 1978). For ECM, in the low-density limit emission is expected only

at the fundamental frequency, but in a region with varying plasma density, fundamental emission may occur simultaneous to second harmonic with the opposite sense of circular polarization (Winglee 1985), as has been observed in Jupiter's auroral kilometric radiation (Mellott et al. 1986). ECM may also be responsible for solar spike bursts observed at frequency ratios implying the presence of 2nd to 6th harmonics, all of which had consistent weak circular polarization (Guedel 1990).

- **Fine structures in dynamic spectrum.** Treumann (2006) argues that fine structures in the dynamic spectrum showing rapid time variability and narrow bandwidth, observed in the auroral radiation of solar system planets, are a smoking gun for the electron-cyclotron maser.

1.4.2 Cause of Frequency Drift

For both emission mechanisms, the emission frequency depends on the conditions in the source region, so different frequencies correspond to different source regions. Solar, stellar, and planetary radio bursts all show evidence of frequency drift, seen in narrowband bursts or sub-bursts whose center frequency drifts upwards or downwards over time.

There are two potential causes for frequency drift in coherent bursts, i.e., two possible reasons that the source region is changing over time:

1. **Source motion.** Measuring frequency drift rate, combined with a model of the spatial variation of plasma density or magnetic field strength, enables estimation of an apparent source velocity. If the emission is at the plasma frequency or its harmonics, the time for a source with speed v (outwards is positive) to cross from starting frequency ν_1 to ending frequency ν_2 is:

$$t = \frac{2L}{v} \ln \frac{\nu_1}{\nu_2} = (60 \text{ sec}) \left(\frac{L}{30 \text{ Mm}} \right) \left(\frac{1000 \text{ km/s}}{v} \right) \ln \frac{\nu_1}{\nu_2}, \tag{1.2}$$

   where $L = H \cos \psi$, where H is the coronal density scale height, and ψ is the angle between the direction of propagation of the source and the density gradient.

   One type of moving coronal source, responsible for features with rapid frequency drift (covering an octave in frequency in ~0.1 sec), is an electron beam, moving at speeds of order 0.1c. Solar Type III radio bursts originate at plasma frequencies in the solar corona and sweep rapidly downwards to kHz

frequencies corresponding to the interplanetary medium; these features are produced by high-speed electrons traveling outwards along open magnetic field lines.

Another type of moving coronal source is a coronal mass ejection. In regions where the CME exceeds the fast magnetosonic speed (roughly the Alfvén speed), the CME forms a shock front, which accelerates electrons to high speeds. These electrons stream ahead of the shock front, exciting plasma emission at the frequency corresponding to the ambient plasma density upstream of the shock. Solar Type II radio bursts are associated with CME shock fronts, with frequency drift rates that cross an octave in roughly one minute, corresponding to speeds of order 1000 km/s.

If the emission is at the cyclotron frequency or its harmonics, the time to cross follows a similar form to Equation 1.2, replacing density scale height with a magnetic scale length. Frequency drifts of narrow-bandwidth, short time duration substructure ("striae") in ECM emission may be due to motion of the "elementary radiation sources" producing the emission, as has been considered for substructure during an intense right circularly polarized 1.1-1.6 GHz burst on AD Leo (Osten & Bastian 2008).

2. **Rotational modulation.** Coherent emission can be highly beamed, particularly ECM, which is beamed into the thin surface of a wide cone. As the surface of the cone emitted from a particular region passes through our line of sight, we briefly detect emission from that region. Sweeps in frequency over time can be produced as a purely geometric effect, as the beamed emission from different source regions rotates into the line of sight. This effect has been modeled for Jupiter's decametric emission, using beam widths of order 1° as observed by Kaiser et al. (2000), to explain arc shapes in the dynamic spectrum with frequency structure varying over minutes to hours (Hess et al. 2008).

In order to detect bulk plasma motion in stellar coronae, it is important to distinguish between true source motion and frequency drift due to rotational modulation. The smoking gun to identify frequency drift due to rotational modulation is repetition of the emission feature once per stellar rotation period, such as seen on brown dwarfs (Hallinan et al. 2007) and chemically peculiar massive star CU Virginis (where Trigilio et al. 2011, interpret frequency drift as due to frequency-dependent

propagation effects). The diverse assortment of bright coherent bursts detected on active M dwarfs may come from two distinct populations: stochastic bursts tracing source motion during stellar flares and eruptions, and periodic bursts powered by an auroral current system.

1.5 Overview of thesis

The mid-1970s to mid-1990s were a heyday for radio observations of active M dwarfs, during which their quiescent and coherent radio emission were discovered and characterized to the extent of the abilities of centimeter and meter wavelength telescopes at the time. With the current advent of sensitive, wideband low-frequency radio facilities and the stellar transient populations they are sure to detect, combined with the rising interest in the implications of M dwarf magnetic activity for planetary atmospheres, we are at a time where both technological advances and scientific motivation will make it rewarding to reopen the book on stellar radio bursts.

Chapter 2 of this thesis starts with the opposite of radio bursts from active stars, detailing the first detection of analogs to the quiescent radio Sun at stellar distances. Chapters 3 to 6 present work I conducted on the search for stellar coronal mass ejections via their radio signatures. Chapter 3 tells the story of the Starburst project, an instrument developed for the purpose of 1-6 GHz dynamic spectroscopy of stellar coherent radio bursts. Chapter 4 provides an overview of a 58-hour VLA survey of active M dwarfs with wideband dynamic spectroscopy, including statistics of burst rates at different radio frequencies, predictions of transient densities for various transient surveys, and analysis of an exceptional radio burst on YZ CMi. Chapters 5 and 6 combine the survey data from Chapter 4 with simultaneous VLBA observations to characterize a wide-bandwidth, luminous radio aurora on UV Ceti (Chapter 5) and compare the diverse flaring events seen across AD Leo's spectrum during a period of heightened activity (Chapter 6). In Chapter 7, I briefly summarize the results and look forward to the next destinations in the search for extrasolar coronal mass ejections.

Chapter 2

FIRST DETECTION OF THERMAL RADIO EMISSION FROM SOLAR-TYPE STARS WITH THE KARL G. JANSKY VERY LARGE ARRAY

Villadsen, J., Hallinan, G., Bourke, S., Güdel, M., & Rupen, M. 2014, ApJ, 788, 112, 112, DOI: 10.1088/0004-637X/788/2/112, arXiv: 1405.2341 [astro-ph.SR], URL: http://adsabs.harvard.edu/abs/2014ApJ...788..112V,

Abstract

We present the first detections of thermal radio emission from the atmospheres of solar-type stars τ Cet, η Cas A, and 40 Eri A. These stars all resemble the Sun in age and level of magnetic activity, as indicated by X-ray luminosity and chromospheric emission in calcium-II H and K lines. We observed these stars with the Karl G. Jansky Very Large Array with sensitivities of a few μJy at combinations of 10.0, 15.0, and 34.5 GHz. τ Cet, η Cas A, and 40 Eri A are all detected at 34.5 GHz with signal-to-noise ratios of 6.5, 5.2, and 4.5, respectively. 15.0-GHz upper limits imply a rising spectral index greater than 1.0 for τ Cet and 1.6 for η Cas A, at the 95% confidence level. The measured 34.5-GHz flux densities correspond to stellar disk-averaged brightness temperatures of roughly 10,000 K, similar to the solar brightness temperature at the same frequency. We explain this emission as optically-thick thermal free-free emission from the chromosphere, with possible contributions from coronal gyroresonance emission above active regions and coronal free-free emission. These and similar quality data on other nearby solar-type stars, when combined with ALMA observations, will enable the construction of temperature profiles of their chromospheres and lower transition regions.

2.1 Introduction

Efforts to measure radio emission from the Sun started as early as the 1890s by Wilsing & Scheiner (1896). The first detections occurred during the boom in radio technology development during World War II, when military radio engineers

James Stanley Hey (1946) in Britain, George Clark Southworth (1945) in the United States, and Bruce Slee in Australia (Orchiston 2005) all independently identified solar radio emission as a source of interference in their radar signals.

Seventy years later, solar radio observations have contributed significantly to a detailed (although far from complete) understanding of the solar atmosphere. Solar flares produce transient radio emission from MHz to GHz frequencies, including gyrosynchrotron storms and coherent bursts, which act as diagnostics of electron density and magnetic field strength in the solar corona (see Bastian et al. 1998 for a review).

From centimeter to far-infrared wavelengths, the quiet Sun emits optically-thick thermal radiation that departs slightly from the Rayleigh-Jeans law due to variation of brightness temperature with frequency. In models of the solar atmosphere (e.g., Loukitcheva et al. 2004), the quiet-Sun brightness temperature spectrum probes atmospheric temperature from the temperature minimum (far-IR) to the upper chromosphere at $\sim 10^4$ K (cm wavelengths), where free-free absorption dominates the opacity. During periods of heightened solar activity, low-frequency solar radiation (below 10-20 GHz) is enhanced by bright spots above active regions, where the $\sim 10^6$-K corona is optically thick due to gyroresonant and/or free-free opacity. For this reason, the 10.7-cm solar flux density $F_{10.7}$ is a traditional measure of solar activity, varying by a factor of 2 to 3 during the solar cycle.

For the nearest stars, radio luminosities at the level of the quiet Sun correspond to μJy flux densities at GHz frequencies, rising to tens of μJy above 20 GHz. Previous generations of radio telescopes have not been sensitive enough to detect such a signal. Probing higher luminosities, Drake et al. (1993) detected 8.3-GHz thermal chromospheric emission from Procyon, a slightly-evolved F5 subgiant, which has a radio luminosity roughly 10 times that of the quiet Sun due to its larger surface area and elevated brightness temperature.

To date, all radio-detected main-sequence stars have microwave luminosities orders of magnitude higher than the quiet Sun (for a review of stellar radio emission, refer to Güdel 2002). Gary & Linsky (1981) and Linsky & Gary (1983) reported and interpreted the first detections of radio emission from low-mass main-sequence stars. The stars' high radio luminosities are predominantly attributed to gyrosynchrotron emission from a persistent non-thermal electron population in the corona, a feature with no analog in the non-flaring Sun. This intense radio emission is accompanied by vigorous magnetic activity, indicated by X-ray luminosities orders of magnitude

Table 2.1 Basic stellar properties.

Name	HD	Dist. (pc)	Spectral Type	Ref.	Mass ($M_\odot$)	Ref.	Radius ($R_\odot$)	Ref.	T_{eff} (K)	Ref.	[Fe/H]	Ref.	Known Stellar Companions	Ref.
τ Cet	10700	3.65	G8.5V	1	0.783	3	0.790	6	5400	1	-0.40	1	none	
η Cas A	4614	5.95	F9V	2	0.972	4	1.039	4	6000	4	-0.25	8	K7V @ 70 AU (12")	9
40 Eri A	26965	4.98	K0.5V	1	0.84	5	0.77	7	5100	1	-0.28	1	DA3 & M5Ve @ 400 AU (80")	10

Distances to stars are based on parallaxes from van Leeuwen (2007). The orbital separations of any stellar companions are reported as the orbital semi-major axis. References: (1) Gray et al. (2006), (2) Gray et al. (2001b), (3) Teixeira et al. (2009), (4) Boyajian et al. (2012), (5) Holmberg et al. (2007), (6) di Folco et al. (2007), (7) Demory et al. (2009), (8) Gray et al. (2001a), (9) Mason et al. (2013), (10) Heintz (1974).

above solar. Güdel & Benz (1993) observed a correlation between X-ray and radio luminosity in quiescent emission from coronae of magnetically-active dwarf stars. Benz & Güdel (1994b) observed that the X-ray-radio luminosity relation is also seen in solar flares, suggesting that non-thermal stellar radio "coronae" may consist of the emission from many small flares, or at least are continuously heated by flares. Güdel et al. (1994) detected 8.5-GHz emission from X-ray-bright solar-type stars; these stars have radio luminosities a few thousand times that of the Sun, consistent with the X-ray-radio luminosity relation, so their radio luminosity is attributed to gyrosynchrotron emission.

The X-ray-radio luminosity relationship observed in active stars does not extend to stars with moderate-to-low magnetic activity. Güdel et al. (1998) and Gaidos et al. (2000) used the Very Large Array to search for 8.4-GHz radio emission from young, moderately active solar-type stars π^1 UMa, κ^1 Cet, and β Com at 8.4 GHz, reaching 3σ detection limits of 20-30 μJy. These upper limits correspond to radio luminosities of $\sim 10^{12.5}$ erg/s, which fall below expectations based on their X-ray luminosities. These stars do not show evidence of the strong gyrosynchrotron component that outshines thermal emission in more active stars, but their thermal component is too faint to detect due to their distance (9 to 14 pc).

To detect the analog of the thermal radiation that dominates quiescent microwave emission from the Sun, we turn to nearby solar-type stars (at 4 to 6 pc) with solar-like X-ray luminosities. Previous to the results reported here, the most sensitive microwave observations of such stars were performed with the Very Large Array by Güdel (1992), placing a 3σ upper limit of 80 μJy on the 8.3-GHz flux density of 40 Eridani A. (In contrast, at sub-mm wavelengths, the optically-thick thermal emission from the low chromospheres of these stars is of order a few mJy, but is blended with debris-disk emission of comparable brightness, as in the case of the observations of τ Cet's debris disk by Greaves et al. 2004.) With the enhanced sensitivity of the Karl G. Jansky Very Large Array (VLA), the observations described in this paper reached a 3σ detection limit of 6 to 12 μJy in a few hours of observation, enabling the first detections of microwave radio emission from the thermal atmospheres of solar-type stars. (The term "solar-type stars," as used in this paper, refers to main sequence stars of spectral type late F through early K.)

In this paper we present the first detections of thermal radio emission from three nearby solar-type stars with solar-like levels of magnetic activity: τ Ceti, η Cassiopeiae A, and 40 Eridani A. In Section 2.2, we review our sample and describe

the observing program. Section 2.3 presents the source detections and upper limits and compares them to the solar brightness temperature spectrum. Section 2.4 discusses a variety of possible emission mechanisms for the detected radiation. In Section 2.5, we conclude with a review of the detected sources and most likely emission mechanisms and discuss the potential for future observations with ALMA and the SKA.

2.2 Observations

Our sample consists of three of the nearest stars of spectral type F9V through K0.5V that are observable from the VLA's latitude: τ Cet, η Cas A, and 40 Eri A. Tables 2.1 and 2.2 compare these stars' properties, including a number of measures of stellar activity, to those of the Sun. All three stars are a good match for the Sun in age and activity level.

Table 2.3 summarizes the observations of all stars in the sample. Each star in the sample was observed with the full VLA array of 27 antennas in X band (8.0 - 12.0 GHz), Ku band (12.0 - 18.0 GHz), and/or Ka band (tuned to 30.5 - 38.5 GHz). Observations of a single source in different bands occurred on different dates. The VLA WIDAR correlator's 3-bit observing mode enabled up to 8-GHz bandwidth.

Table 2.2 Measures of stellar magnetic activity.

Name	$\log_{10} L_X$ (erg s^{-1})	Ref.	P_{rot} (days)	Ref.	$\log_{10} R'_{HK}$	Ref.	Age (Gyr)	Ref.
τ Cet	26.5	1	34	3	-5.01	6	5.8	7
η Cas A	27.4	1	17	4	-4.93	6	2.9	7
40 Eri A	27.2	1	43	3	-4.872	3	5.6	7
Sun	27.35	2	26.1	5	-4.906	7	4.6	8

References: (1) NEXXUS catalog (Schmitt & Liefke 2004). Stellar X-ray luminosities from pointed observations by the ROSAT High-Resolution Imager (HRI). (2) Judge et al. (2003). Solar L_X averaged over the solar cycle, calculated for the ROSAT All-Sky Survey 0.1 to 2.4 keV bandpass. The solar L_X varies by about an order of magnitude from solar minimum to solar maximum. (3) Baliunas et al. (1996). Rotation periods determined from rotational modulation of Ca II H&K lines. (4) Wright et al. (2004). Rotation period inferred from $\log_{10} R'_{HK}$ by activity-rotation relation. (5) Donahue et al. (1996). (6) Canto Martins et al. (2011). (7) Mamajek & Hillenbrand (2008). Note that age is not an independent measure of activity: these ages were derived using empirical gyrochronology relations from rotation rates, which were in turn derived from $\log_{10} R'_{HK}$. (8) Bouvier & Wadhwa (2010).

Table 2.3 Summary of observations.

Star	Band	Center Frequency (GHz)	Band-width (GHz)	# of Epochs	Time on Source (h)	VLA Configuration	Synthesized Beam Dimensions (FWHM)	RMS (μJy)	Phase Calibrator	Flux Calibrator
τ Cet	Ka	34.5	8.0	2	5.0	DnC	2.11" × 1.45"	3.9	J0204-1701	3C147
	Ku	15.0	6.0	1	2.0	D	8.99" × 4.64"	3.0		
η Cas A	Ka	34.5	8.0	4	8.0	DnC/C	1.01" × 0.83"	3.1	J0102+5824	3C147
	Ku	15.0	6.0	3	5.0	D/C	2.40" × 2.25"	2.1		& 3C48
	X	10.0	4.0	2	3.0	D	11.93" × 7.98"	2.7		
40 Eri A	Ka	34.5	8.0	3	5.5	DnC→C/C	0.98" × 0.73"	3.7	J0423-0120	3C147

All observations were made between March and September 2013.

Observations were performed between March and September 2013, with the VLA in D configuration and C configuration as well as intermediate configurations. Observations alternated between a nearby phase calibrator and the target source with cycle times of 7.5 minutes in Ka band and 17 minutes in X and Ku band. Typical sensitivities obtained with the full bandwidth in one hour on source were 4 μJy rms in X and Ku bands and 7 μJy rms in Ka band.

Typical VLA observations in X, Ku, and Ka bands reach an absolute flux calibration accuracy of 5% to 10%. Throughout the rest of the paper, quoted measurement errors reflect only the statistical error on measurements due to random noise on the source visibilities, not the systematic error due to absolute flux calibration. Measured flux density may also be reduced compared to the true value if the gain calibrations interpolated from the phase calibrator are not sufficient to correct for the variation of gain phases with time; however, the gain solutions obtained for the phase calibrator in all bands varied slowly and smoothly over time, suggesting that this source of error is negligible.

2.2.1 Source Motion

The expected positions of the sources were determined using Hipparcos coordinates and proper motions (van Leeuwen 2007), with an additional correction for parallactic motion based on the distances in Table 2.1. In addition, the position of η Cas A was corrected for displacement due to orbital acceleration, which resulted in a 0.3" displacement northwest of the position expected from proper motion and parallax. The orbital ephemeris calculation used an Excel workbook developed by Brian Workman[1] with data from the US Naval Observatory's Washington Double Star Catalog by Mason et al. (2013). 40 Eri A did not require a correction for orbital motion because the 40 Eri orbital period is much longer than that of η Cas.

Since the targets are within a few parsecs, the sources moved by as much as 1" due to proper motion and parallax during the half-year in which we observed. In comparison, our Ka-band observations reached a typical synthesized beam of 1" and an astrometric accuracy of order 0.1". To avoid smearing of the source and obtain accurate astrometry, we used the interferometry software package CASA's routine *fixvis* to shift the visibility phases to keep the expected location of the source at the phase center in all observations, before combining and imaging visibility data from different epochs.

[1] As of 2014 January 15, available online at `http://www.saguaroastro.org/content/db/binaries_6th_Excel97.zip`.

2.2.2 Chance Alignment of Extragalactic Sources

Based on the 3-GHz source counts of Condon et al. (2012), chance alignment of an unrelated source is a negligible source of error in these observations. Condon et al. (2012) performed 3-GHz source counts with 1-μJy sensitivity and measured a differential source count of:

$$n(S) = 9000 S^{-1.7} \text{ Jy}^{-1} \text{ sr}^{-1}. \tag{2.1}$$

Considering the scenario where source counts are independent of frequency, then the highest probability of finding a 1σ unrelated source within the synthesized beam is 18%, for the X-band observations of η Cas A (since those observations have the largest synthesized beam). For most other observations, the probability is much lower. In all cases where a source was detected, the probability of an unrelated source with flux density greater than or equal to the detected level (see Table 2.4) falling in the synthesized beam is 0.1% or less.

We base our statistics on 3-GHz source counts because source counts at higher frequencies are not available for μJy-level sources, but the probabilities of chance alignment of detectable sources in the observed bands (10, 15, and 34.5 GHz) are likely lower than at 3 GHz. The Australia Telescope 20 GHz Survey, which surveyed the 20-GHz southern sky down to a depth of 40 mJy, found that only 1.2% of 20-GHz sources were undetected or weakly detected at 5 GHz (Murphy et al. 2010) and that the majority of 5- and 8-GHz sources are flat- or falling-spectrum (Massardi et al. 2011). The 15.7-GHz Tenth Cambridge survey with the Arcminute Microkelvin Imager (Whittam et al. 2013), which was complete to 500 μJy over 12 deg^2, found that sources below 800 μJy tend to be flat spectrum. Thus it is reasonable to use 3-GHz source counts to put upper limits on the probability of chance alignment of extragalactic sources in our observations.

2.3 Results

2.3.1 Detections

Solar-type stars τ Cet, η Cas A, and 40 Eri A were all detected in Ka band (center frequency 34.5 GHz) with signal-to-noise ratio (SNR) of 6.5, 5.2, and 4.5, respectively. Table 2.4 gives the measured flux density for each source, where all the Ka-band observations of a single source from different dates have been combined. Figure 2.1 shows the VLA images of the detections (also one image per star, with all Ka-band observations combined). Flux densities and source positions were determined by using CASA's *uvmodelfit* task to fit a point source model to the visibilities.

To check whether the source was consistent with a point source, CASA's *imfit* task was also used to fit an elliptical Gaussian with unconstrained shape, which yielded dimensions consistent with the CLEAN beam to within 3 sigma for all sources.

The sources were imaged in full Stokes, but were only detected at or above the 3σ level in Stokes I (total intensity). We used the Stokes V (circularly polarized) flux density at the pixel representing the expected position of the source to calculate confidence intervals on the degree of circular polarization $r_c = V/I$ for each source, where r_c varies from -1 to 1. We obtained 95%-confidence intervals on r_c of [-0.52,0.14], [-0.18,0.69], and [-0.87,0.12] for τ Cet, η Cas A, and 40 Eri A, respectively.

To check for flares, we created Ka-band time series in Stokes I and V for each of the stars, averaging the observations over a range of timescales from 15 seconds to 25 minutes. Analysis of the time series showed no statistically significant evidence of variability, consistent with quiescence. All time series were consistent with constant flux density with reduced χ^2 ranging from 1 to 2 for different averaging times, with values of 1.1, 1.3, and 1.6 for 25-minute averaging of Stokes I for τ Cet, η Cas A, and 40 Eri A, respectively. Thus, these detections are consistent with non-flaring emission.

Positions

The fifth column of Table 2.4, titled "Position Offset," gives the offset of the VLA-observed position of each source compared to the phase center, where the phase

Table 2.4 Detections.

Star	34.5-GHz Flux Density (μJy)	RMS (μJy)	SNR	Position Offset [a] (sigma)	Brightness Temperature [b] (K)
τ Cet	25.3	3.9	6.5	3.9	9300±1400
η Cas A	16.0	3.1	5.2	0.4	9500±1800
40 Eri A	16.5	3.7	4.5	0.5	10200±2300

[a] The offset from the expected position based on Hipparcos astrometry (van Leeuwen 2007), in units of sigma (i.e. the distance between the measured and expected coords, divided by the amplitude of the error ellipse in the offset direction).

[b] Brightness temperature is averaged over the stellar disk, using the photospheric radii and distances reported in Table 2.1. The reported errors do not include the 5%- to 10%-percent errors typical of absolute flux calibration with the VLA for X, Ku, and Ka bands.

center is the expected position predicted from Hipparcos coordinates and proper motions, as described in Section 2.2.1. This offset is given in units of sigma, i.e. the offset distance in arcseconds divided by the amplitude of the position error ellipse in arcseconds in the offset direction. The position error ellipse is the synthesized beam, defined as the CLEAN restoring beam, divided by the signal-to-noise ratio of the source detection. η Cas A and 40 Eri A show good agreement between the expected and observed positions. τ Cet shows a 3.9σ, or 0.37", difference; however, the expected position agrees well with the location of peak flux density in the image. We are confident that the observed source is indeed τ Cet, because of the low probability of coincidence of an extragalactic source, and because the observed source is the only source detected in the 1.3' primary beam at the 4σ level or greater.

2.3.2 Upper Limits

Our observations at 10 GHz (η Cas A) and 15 GHz (τ Cet and η Cas A) did not lead to detections, but enabled us to put upper limits on the flux density from these sources at these frequencies. In the case of a non-detection, the flux density in the pixel at the star's known location still constitutes a measurement of the flux density, where the measurement is drawn from a Gaussian distribution whose mean is the true flux density and whose standard deviation is the image RMS. The measured flux densities were 4.6 μJy for τ Cet in Ku band, -0.56 μJy for η Cas A in Ku band, and 1.8 μJy for η Cas A in X band. The posterior probability distributions for flux density were calculated using flat priors that disallowed negative values for the true flux density of the source, resulting in the 95%- and 99%-confidence upper limits on flux density shown in Table 2.5.

For comparison, the traditional method of reporting 3σ upper limits is equivalent to giving the 99.73%-confidence upper limit in the case where the flux density measured at the known location of the source is zero (or where the location of the source

Table 2.5 Non-detections.

Star	Center Frequency (GHz)	RMS (μJy)	95%-Conf. Upper Limit (μJy)	99%-Conf. Upper Limit (μJy)
τ Cet	15.0	3.0	9.6	11.7
η Cas A	10.0	2.7	6.6	8.4
η Cas A	15.0	2.1	3.8	5.0

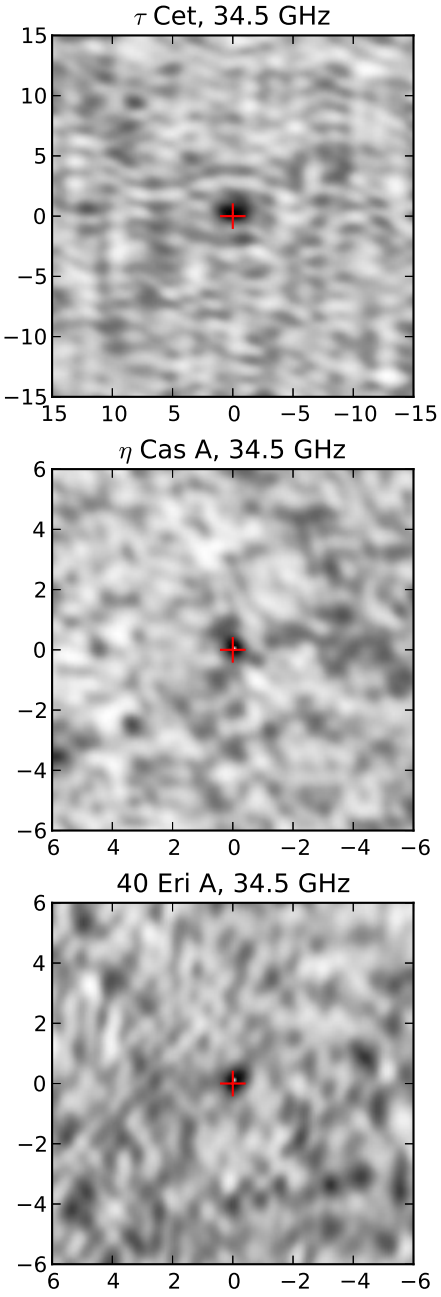

Figure 2.1 Ka-band images of the observed stars. The x- and y-axis are labelled with offset in arcseconds in the E-W and N-S directions, respectively. The cross (colored red in the online version) shows the location of the star, determined from Hipparcos astrometry (van Leeuwen 2007) and adjusted to the epoch of the observations accounting for proper motion, parallax, and (for η Cas A) orbital motion. The size of the cross marker is arbitrary because the errors on astrometry, of order 0.1", are too small to show in these images. See Section 2.3.1 for a comparison of Hipparcos positions and observed positions.

is not known).

2.3.3 Brightness Temperature Spectra

Figure 2.2 shows our constraints on the flux density and brightness temperature (T_b) spectra of the observed stars, compared to the solar spectrum. All three detections of solar-type stars are consistent with the solar brightness temperature in Ka band, suggesting that the emission observed in these cases is most likely chromospheric blackbody emission as in the Sun (see Section 2.4.1). The upper limits placed on the stars' T_b are consistent with the solar brightness temperature spectrum.

Spectral Index

The combination of the upper limits on 15.0-GHz flux density and the measured 34.5-GHz flux densities indicates that τ Cet and η Cas A have rising spectra from 15.0 to 34.5 GHz (as seen on the left in Figure 2.2). We calculated lower limits on the 15-to-34.5-GHz spectral index α for these two stars, where α is defined as the positive power-law index for the flux spectrum:

$$S_\nu \propto \nu^\alpha. \tag{2.2}$$

To do so, we considered the measured value for the Ku-band flux density to be the Ku-band flux density in the pixel at the star's known location (4.6 μJy for τ Cet and -0.56 μJy for η Cas A), drawn from a Gaussian distribution with the image RMS. The posterior probability distribution for spectral index was calculated using least-informative Jeffreys priors, resulting in 95%-confidence lower limits on α of 1.0 and 1.6, for τ Cet and η Cas A, respectively, and 99%-confidence lower limits of 0.8 and 1.1.

It should be noted that these statistical constraints on spectral index reflect only the random error on the visibilities: as noted in Section 2.2, we do not account for the systematic effect of relative errors in absolute flux calibration for different bands.

2.4 Discussion

2.4.1 Chromospheric Stellar Disk Emission

35-GHz solar radio emission is dominated by thermal emission from the chromosphere, which is optically thick at cm wavelengths due to free-free opacity. The disk-averaged brightness temperatures reported in Table 2.4 are consistent with the 35-GHz quiet-Sun brightness temperature of 9300 K reported in White (2004).

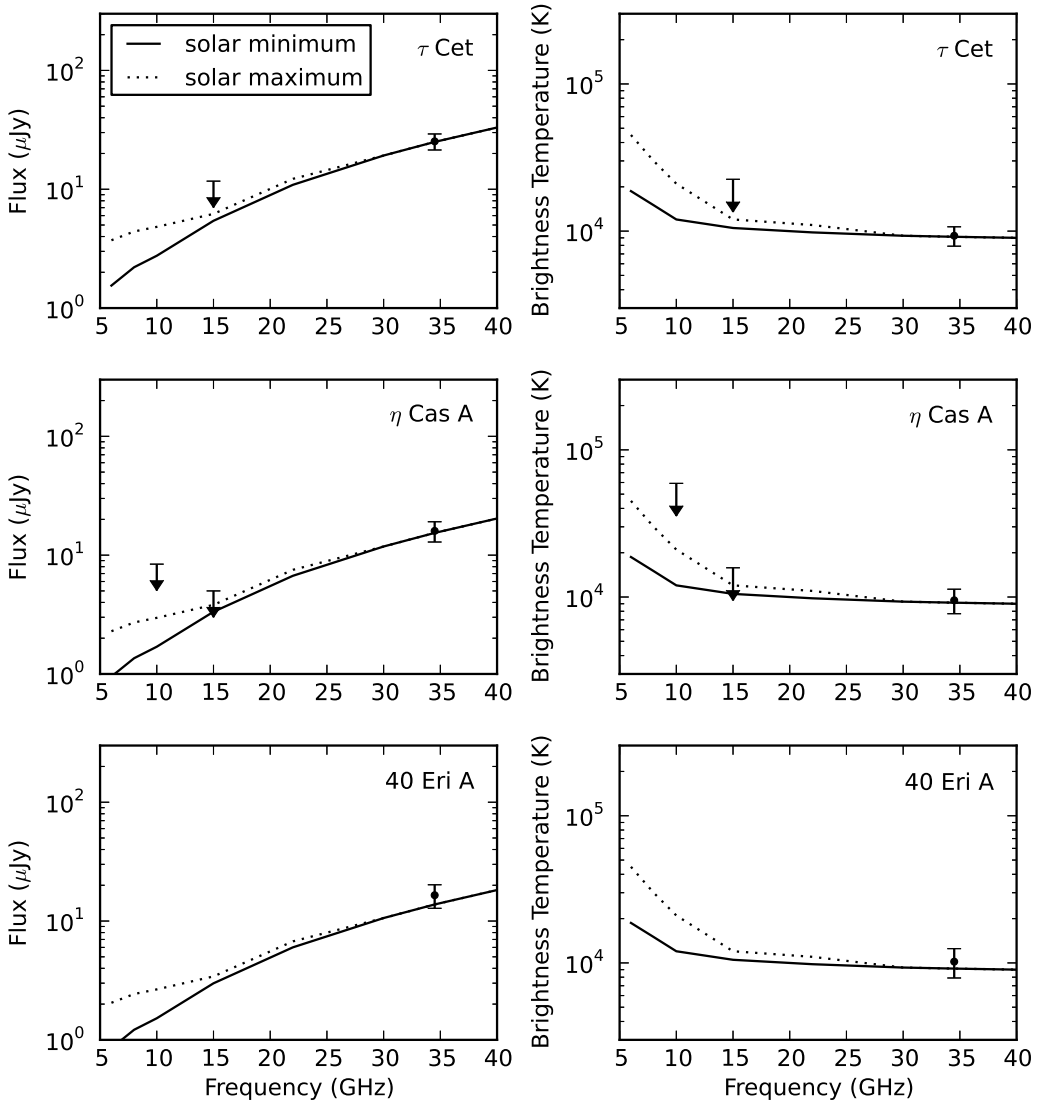

Figure 2.2 Left column: Flux spectra for the observed stars. Right column: Stellar disk-averaged brightness temperature spectra. Both columns: non-detections are shown as downwards arrows marking the 99%-confidence upper limits (Table 2.5) and detections as points with 1σ error bars (Table 2.4). The plots also show the solar spectra from White (2004) for solar minimum (solid line) and solar maximum (dotted line); in the left plots the solar flux density is scaled to the distance and radius of each star, so the lines show the flux density the star would have if it had solar brightness temperatures. The solar cycle mainly affects the solar spectrum below 15 GHz, where gyroresonant emission from active regions contributes significantly to the emission, because the number and strength of active regions varies with the solar cycle. Above 15 GHz, solar radiation is predominantly chromospheric thermal free-free emission, which is constant throughout the solar cycle because the temperature of the chromosphere remains steady.

At microwave frequencies, the radio opacity of the quiet Sun is dominated by free-free opacity from free electrons and ions. At an upper-chromosphere temperature of 10^4 K and frequencies near 34.5 GHz, the free-free absorption coefficient (from Equation 20 in Dulk 1985) is:

$$\kappa_{\nu,ff} \approx 0.076 \frac{n_e^2}{\nu^2 T^{3/2}}, \tag{2.3}$$

where all quantities are in cgs units. The frequency dependence of free-free opacity implies that different frequencies probe different depths, and therefore different temperatures, in the stellar atmosphere. Since free-free opacity also depends on density, a brightness temperature spectrum can constrain temperature and density profiles of model chromospheres, as for models of the solar chromosphere in Loukitcheva et al. (2004) and Fontenla et al. (2007). Comparable models of the atmospheres of these low-activity solar-type stars may be constrained using a brightness temperature spectrum consisting of the VLA data presented here combined with ALMA and far-IR data. The cm-wavelength observations in this paper probe the upper chromosphere and the base of the transition region, whereas mm-wavelength data would provide a glimpse of the lower chromosphere, and far-IR data would reveal the conditions of the temperature minimum (see for example the direct detection of the α Cen A temperature minimum by Liseau et al. 2013).

Lim et al. (1998) took a similar approach to construct a temperature profile of the atmosphere of supergiant Betelgeuse, observing with the VLA from 5 to 43 GHz. The supergiant star's extended atmosphere was resolved, enabling direct measurement of the atmospheric height probed by each frequency and of the source size for the purpose of calculating brightness temperature. In our case, the source is unresolved, but the chromosphere is likely close enough to the photosphere that assuming the photospheric radius will yield an accurate calculation of brightness temperature; however, the relationship between frequency and atmospheric height must be inferred from atmospheric models.

2.4.2 Coronal Gyroresonance Emission

The enhanced magnetic field strengths above active regions may cause the corona to become optically thick due to gyroresonant opacity, resulting in bright spots at coronal temperatures of $\sim 10^6$ K on the 10^4-K stellar disk. In a given field strength B (in G), free electrons absorb and emit at harmonics of this gyromagnetic frequency:

$$\nu = s\nu_B = sB\,(2.8\,\mathrm{MHz})\,, \tag{2.4}$$

where the solar corona typically becomes optically thick at low harmonics ($s \sim 3-5$). For gyroresonant radiation in the $s = 3$ harmonic to contribute to the observed stellar 34.5-GHz radiation requires the presence of coronal magnetic field strengths of 4.1 kG; 34.5-GHz emission in the lowest harmonic would require coronal field strengths of 12.3 kG.

Our data constrain the covering fraction f_{15} of coronal bright spots at 15 GHz, i.e. the covering fraction of ~1.8-kG magnetic fields in the corona. We model the 15-GHz disk-averaged brightness temperature T_{15} using a stellar disk with brightness temperature T_{chrom}, which is uniform except where the chromosphere is obscured by coronal bright spots with temperature T_{cor}:

$$T_{15} = (1 - f_{15})\, T_{chrom} + f_{15}\, T_{cor}. \tag{2.5}$$

If we assume that the coronal contribution at 34.5 GHz is negligible, then the measured 34.5-GHz brightness temperature is a direct measurement of T_{chrom}. Combining that with an assumed coronal temperature of $T_{cor} = 10^6$ K, we can convert our upper limits on 15-GHz flux density to upper limits on f_{15}. We obtain 95%-confidence upper limits on 15-GHz coronal covering fraction of 1.1% for τ Cet and 0.8% for η Cas A.

Although our data alone cannot rule out a coronal contribution to the detected 34.5-GHz emission, a significant coronal contribution at 34.5 GHz is unlikely considering the solar case. White (2004), and in personal communication White (2013), report the disk-integrated solar brightness temperature spectrum observed by Nobeyama at a consecutive solar minimum and maximum. These spectra show no significant variation at 35 GHz over the solar cycle. From this we infer that coronal bright spots, likely optically-thin at these high frequencies, contribute only a small, difficult-to-detect fraction of the disk-integrated 35-GHz solar emission. Since the observed stars have similar levels of magnetic activity to the Sun, coronal emission above active regions likely does not contribute significantly to the stellar 35-GHz emission. However, if it does, this would provide a diagnostic for tracking stellar cycles, since the active region coverage should vary significantly between stellar minimum and maximum.

Gyroresonant emission from a region with uniform magnetic field can have a high degree of circular polarization, depending on the viewing angle. The sense of circular polarization is determined by the line-of-sight magnetic field direction. The gyroresonant contribution to the emission, averaged over the stellar disk, will have

lower circular polarization than the emission from individual regions because regions of opposite magnetic polarity cancel each other out. In a given hemisphere on the Sun, sunspots of one polarity tend to have stronger magnetic fields, which means that the disk-integrated gyroresonant emission from the star may have significant circular polarization when viewed from high latitudes.

The detection of circular polarization in stellar microwave emission would be a smoking gun for a gyroresonant contribution. Our observations are consistent with zero circular polarization at 34.5 GHz (refer to Section 2.3.1 for constraints on r_c), as expected since gyroresonance contributes only a small fraction of the solar 35-GHz emission. If future, deeper observations of these stars below 10-15 GHz (the frequency below which gyroresonance contributes significantly to the disk-integrated quiet Sun emission) can detect circular polarization, flips in the sense of this polarization could then be used to track polarity reversals due to the stellar magnetic activity cycle.

2.4.3 Coronal Free-Free Emission

As mentioned above, coronal radiation is unlikely to contribute a significant fraction of the observed 34.5-GHz emission. In the case of the Sun, the corona is optically-thin to free-free emission above a few GHz. Optically-thin free-free emission has a nearly flat spectrum, so the rising spectra observed in τ Cet and η Cas A from 15 to 34.5 GHz imply that the 34.5-GHz emission is not dominated by coronal bremsstrahlung. One of the sources of coronal bremsstrahlung is the stellar wind, so these observations also place upper limits on the mass loss rates from these stars.

Stellar Wind Emission

The diffuse corona that lies on open field lines (i.e., not above active regions) flows into the stellar wind. This gas contributes a small fraction of the net free-free radio emission calculated from the X-ray emission measure, since most gas in the solar corona is magnetically bound to the star.

We can estimate expected levels of free-free radio emission from the magnetically-open corona by assuming a stellar wind with solar-like properties. The Sun loses mass through the solar wind at a rate of 2-3$\times 10^{-14}$ $M_\odot$ yr^{-1}. The solar wind has a fast component and a slow component, as reviewed in Aschwanden et al. (2001). The base of the solar wind has coronal temperatures, typically around 1 MK. For the following calculations, we scale equations to an "average" solar wind speed

of $500\,\mathrm{km\,s^{-1}}$ and a wind temperature of 1 MK, and an ionized mass loss rate of $10^{-14}\,\mathrm{M_\odot\,yr^{-1}}$. We assume a spherically-symmetric, constant-velocity wind with a steady mass loss rate, implying a $1/r^2$ density profile. These simplifying assumptions, combined with the assumed solar wind properties, should provide an order-of-magnitude estimate of the stellar wind radio flux density.

Using Equation 20 of Dulk (1985) to calculate the optical depth of a stellar wind with solar-like properties, we obtain:

$$\tau = \left(2.0 \times 10^{-10}\right) \left(\frac{\nu}{34.5\ \mathrm{GHz}}\right)^{-2} \left(\frac{T}{10^6\ \mathrm{K}}\right)^{-3/2} \ldots \left(\frac{r}{R_\odot}\right)^{-3} \left(\frac{\dot{M}_{ion}}{10^{-14}\ \mathrm{M_\odot\,yr^{-1}}}\right)^{2} \left(\frac{v_w}{500\ \mathrm{km\ s^{-1}}}\right)^{-2}, \tag{2.6}$$

where r is the distance of the line of sight from the center of the star and $\dot{M}_{ion}$ is the ionized mass loss rate (since only ionized gas contributes to the free-free emission). The 34.5-GHz optical depth is extremely low for a solar-like wind.

Since the wind is optically thin, the radio luminosity is obtained by integrating the free-free emissivity over the wind volume (from the stellar surface to infinity), yielding an expected 34.5-GHz flux density of:

$$S_\nu = \left(2.9 \times 10^{-5}\,\mu\mathrm{Jy}\right) \left(\frac{T}{10^6\ \mathrm{K}}\right)^{-1/2} \left(\frac{R_*}{R_\odot}\right)^{-1} \ldots \left(\frac{\dot{M}_{ion}}{10^{-14}\ \mathrm{M_\odot\,yr^{-1}}}\right)^{2} \left(\frac{v_w}{500\ \mathrm{km\ s^{-1}}}\right)^{-2} \left(\frac{d}{1\ \mathrm{pc}}\right)^{-2} \tag{2.7}$$

for frequencies near 34.5 GHz and electron temperatures near 10^6 K. More general formulas must adjust for the frequency and temperature dependence of the Gaunt factor (e.g. Equation 24b in Güdel 2002).

Equation 2.7 makes it apparent that a stellar wind will not contribute detectably to the stellar radio emission at 34.5 GHz, unless any of these stars have a mass loss rate more than 1000 times the solar mass loss rate. Wood et al. (2005) report stellar mass loss rates (measured using astrospheric absorption of Ly α) of up to 100 times solar for low-mass main sequence stars, but the mass loss rates they measure for stars with solar levels of activity are comparable to the solar mass loss rate. This stands in contrast to radiation pressure-driven winds from massive stars, which can produce radio emission of 100s of μJy or more at kiloparsec distances (Scuderi et al. 1998).

2.4.4 Gyrosynchrotron Emission

Linsky & Gary (1983) proposed that gyrosynchrotron emission dominates the radio luminosity of active stars, in order to explain stellar disk-averaged radio brightness temperatures of greater than 10^8 K, signicantly hotter than the coronal temperatures measured in X-rays. Such high radio brightness temperatures stand in contrast to the 10^4-K temperatures observed in τ Cet, η Cas A, and 40 Eri A. We cannot definitively rule out a gyrosynchrotron contribution on the basis of stellar disk-averaged brightness temperature, since the gyrosynchrotron source could be optically thin or cover only small regions of the star, both of which would reduce the disk-averaged brightness temperature, but gyrosynchrotron emission is not required to explain the observed stellar flux densities. Additionally, the Sun does not flare at a sufficient rate to produce the "quiescent" non-thermal gyrosynchrotron microwave radiation observed in magnetically active stars. Since the observed stars have solar-like levels of magnetic activity and brightness temperatures consistent with thermal emission, gyrosynchrotron radiation is unlikely to contribute appreciably to the detected 35-GHz radio emission.

2.5 Conclusions

We have detected 34.5-GHz radio emission from solar-type stars τ Cet, η Cas A, and 40 Eri A, which all have solar-like levels of magnetic activity. By analogy to the Sun, this emission is most likely thermal chromospheric emission from the entire stellar disk. Our data cannot constrain the possibility of a coronal contribution from thermal gyroresonance or free-free above active regions, but a large such contribution is unlikely since solar disk-integrated 35-GHz emission is steady throughout the solar cycle, independent of the number of active regions. Our sensitive upper limits on 15-GHz flux density for τ Ceti and η Cas A indicate that they have a rising spectrum from 15 to 35 GHz, consistent with optically-thick thermal chromospheric emission. These observations constitute the first radio detection of thermal stellar emission from low-mass main-sequence stars.

The disk-averaged brightness temperatures at 34.5 GHz are of order 10,000 K, higher than the photospheric $T_{\rm eff}$, providing independent confirmation of the temperature inversion in these stellar atmospheres. These VLA observations could be combined with ALMA observations to build a brightness temperature spectrum $T_b(\nu)$ for each star. The brightness temperature spectra can be used to constrain the chromospheric density and temperature profiles predicted by model atmospheres. These constraints on atmospheric models could be further strengthened by the addition of far-infrared

data, which probe the temperature minimum. Most of our understanding of stellar chromospheres currently comes from UV line emission, which is optically thin across the chromosphere. Because radio emission becomes optically thick in the chromosphere, with different frequencies becoming opaque at different depths, a radio brightness temperature spectrum directly measures the electron temperature across different chromospheric layers.

Next-generation radio observatories will enable the detection of thermal quiescent emission from solar-type stars at even lower frequencies, probing optically thick regions at coronal temperatures. As discussed in Section 2.4.2, microwave observations of these stars constrain the covering fraction of magnetic fields of a given strength in the corona, where different frequencies probe different magnetic field strengths. Detecting the emission below 15 GHz (the frequency below which gyroresonance starts to contribute an appreciable fraction of the quiescent solar emission) would provide a way to measure magnetic field strength and size of active regions, with rotational modulation of the radio emission potentially providing information on spatial distribution of these active regions.

Radio observations of these stars below 10 GHz would also provide a diagnostic for tracking stellar magnetic activity cycles, like the solar 10.7-cm flux density $F_{10.7}$, which varies by factors of 2 to 3 over the solar cycle. Of the observed stars, only 40 Eri A has a detected stellar cycle, seen in variation of calcium-II H & K lines with a 10.1-year period (Baliunas et al. 1995). Increasing the number of detected stellar activity cycles would provide a test of dynamo theory and explore the long-period end of the relationship between stellar rotation and activity cycle. The mid-frequency Square Kilometer Array (SKA) will achieve 0.5-μJy sensitivity at GHz frequencies in one hour on source[2]; a few hours per year would be sufficient to monitor stellar activity cycles of low-activity solar-type stars out to about 10 pc. The SKA will have high enough sensitivity to potentially detect circular polarization, which can be used to track polarity reversals in stellar magnetic fields. The enhanced sensitivity of the VLA, combined with the powers of ALMA and eventually the SKA, opens up for exploration a new realm of stellar radio luminosities and emission mechanisms.

[2]SKA1 Baseline Design, March 2013. https://www.skatelescope.org/wp-content/uploads/2012/07/SKA-TEL-SKO-DD-001-1_BaselineDesign1.pdf.

2.6 Acknowledgements

The National Radio Astronomy Observatory is a facility of the National Science Foundation operated under cooperative agreement by Associated Universities, Inc.

This material is based upon work supported by the National Science Foundation Graduate Research Fellowship under Grant No. DGE-1144469.

This research has made use of the SIMBAD database, operated at CDS, Strasbourg, France.

This research benefited from the web page "Basic Astronomical Data for the Sun"[3] created by Eric Mamajek of the University of Rochester.

J.V. thanks Stephen White and Jeffrey Linsky for giving helpful feedback on the paper and additionally thanks Stephen White for information on the quiescent solar microwave brightness temperature spectrum.

[3] https://sites.google.com/site/mamajeksstarnotes/basic-astronomical-data-for-the-sun

Chapter 3

DESIGN AND IMPLEMENTATION OF THE STARBURST SYSTEM

Active M dwarfs are known to flare frequently and energetically compared to the Sun, producing 10^{34} erg flares (e.g. Hawley & Pettersen 1991, Kowalski et al. 2010) which may occur at a rate of once a month based on extrapolation of observed flare frequency distributions (Lacy et al. 1976). If these extreme flares are accompanied by stellar coronal mass ejections (CMEs), planetary atmospheres can be eroded by the CMEs (Khodachenko et al. 2007; Lammer et al. 2007) as well as depleted of ozone by chemical interaction with energetic protons accelerated at shock fronts formed by CMEs (Segura et al. 2010). To assess these possibilities, it is necessary to determine whether the occasional extreme flares on active M dwarfs are accompanied by extreme stellar eruptions.

Wideband spectroscopy of stellar coherent radio bursts offers the potential to detect the shock fronts formed by fast-moving stellar coronal mass ejections. Solar radio spectrometers offer continuous coverage over extremely wide fractional bandwidth (such as 10-100 MHz and 1-18 GHz), allowing detection of radio sources at a wide range of coronal heights. In contrast, the widest fractional bandwidth dynamic spectrum published for a stellar coherent radio burst is at 1.1-1.6 GHz (Osten & Bastian 2008); increasing this fractional bandwidth will improve the detection rate of stellar coherent radio bursts and enable better identification of the causes of individual bursts.

The Starburst project is a facility designed to provide the long observing time and wide fractional bandwidth needed to detect and characterize stellar eruptions. Starburst is a dual-polarization backend consisting of a downconverter and single-baseline cross-correlator with 5 GHz of bandwidth and the capacity for high resolution in time and frequency. It was designed as a backend for the two 27-meter antennas at the Owens Valley Radio Observatory (Figure 3.1), which were being retrofitted with new wideband cooled receivers by the Owens Valley Solar Array (OVSA) expansion project. Due to structural instabilities in the antennas discovered in spring 2016, the Starburst project ended when it was still in the commissioning stage.

Figure 3.1 The 27-m antennas at the Owens Valley Radio Observatory. The Starburst project planned a single-baseline correlation between these antennas using cryogenic feeds built for the Owens Valley Solar Array expansion project.

As part of my graduate thesis, I worked on the Starburst project in the role of project scientist. This role involved identifying scientific requirements and technical specifications for the system, project management, software development (mainly control code and auxiliary code for observation planning, although I would have led data calibration as well), and commissioning. In addition, I led pathfinder observations for Starburst with the Karl G. Jansky Very Large Array (VLA) and the Very Long Baseline Array (VLBA): wideband dynamic spectroscopy of active M dwarfs with the VLA, and high resolution imaging of stellar radio coronae with the VLBA. The purpose of these observations, which are described in Chapters 4 to 6, was to measure the rate of stellar coherent radio bursts and their association rate with resolved coronal structures, providing data to use for proposing multi-wavelength observations simultaneous to Starburst and VLBA observations triggered by Starburst.

3.1 The Owens Valley Solar Array and the 27-m front ends

The OVSA consists of 13 small (2-meter) antennas that observe the Sun continuously during the day at 2.1-18 GHz. The OVSA calibrates the small antennas by observing astronomical calibration sources with cross-correlation between a small antenna and the two 27-meter antennas at OVRO, which provide the sensitivity needed to detect the astronomical calibrators. The OVSA expansion project (EOVSA) included the installation of cooled wideband receivers on the two 27-meter antennas, intended for observing astronomical calibration sources; a cross-correlation between a 27-meter antenna and a 2-meter antenna provides the sensitivity needed to rapidly derive calibration solutions for the small antennas. With the sensitivity of the cooled receivers, these observations would take only a few minutes a day, leaving the 27-m antennas available outside that time for use with the Starburst backend. The OVSA backend provides 600 MHz of instantaneous bandwidth, with an LO frequency that cycles rapidly through bands from 1-18 GHz, switching frequencies every 20 ms. For stellar observations, which need high sensitivity, it is better to have an instantaneous bandwidth that covers all the observing frequencies instead of cycling through frequencies; this is the motivation for building the Starburst backend rather than using the OVSA backend.

The cooled receivers built for EOVSA provide the wide bandwidth and sensitivity needed for observations of stellar coherent radio bursts. The front ends have two dual-polarization ultra-wideband feeds designed by Sander Weinreb's group: a 1-6 GHz feed and a 3-18 GHz feed. These feeds are mounted on a base that can be moved in three dimensions: side to side to enable switching between feeds, in and out to allow individual focus settings for the two feeds, and rotation, to allow the linearly polarized feeds to rotate to track parallactic angle. The system design aimed for 25-50 K system temperature from the front ends, which would enable a sensitivity of 10 mJy RMS in 64 MHz and 30 seconds, providing enough sensitivity to measure the time-frequency structure of the minutes-long coherent radio bursts associated with CMEs.

The first front end was installed on antenna A ("ant14", the western 27-m antenna) in October 2015, with the front end for antenna B ("ant15") planned to follow by mid-2016. Since the commissioning of the front ends occurred on a similar timeline to the commissioning of the Starburst backend, I participated in front end commissioning as well.

Each polarization in the front end went through two stages of amplification in a

cooled vacuum chamber before passing through variable attenuators and being converted to an optical signal for transmission from the antenna to the OVSA correlator room. Caltech undergraduate student Loko Kung wrote the control code for the front end, mentored by James Lamb, Dale Gary, and me. I worked with OVRO staff and OVSA team members to document the requirements for the tasks this code would perform, the protocol for communication with the OVSA's Array Control Computer, and the monitor data to be collected from front end subsystems and the commands to be transmitted to them. These subsystems included motors to move the feeds, a temperature controller, a temperature monitor, a Beaglebone microcontroller that set the bias voltages for the low noise amplifiers, and a power strip used to turn a noise source on and off and toggle a switch that selected between the high band and low band signals. I also helped troubleshoot a network problem with a Rabbit board used to control the variable attenuators in the front end.

I worked with Dale Gary to conduct some of the commissioning observations for the ant14 front end, initially using the OVSA backend rather than the Starburst backend, since the OVSA backend was already well tested from use with the small antennas. At the time the OVSA correlator was running at 0.8 Gigasamples per second (Gsps) instead of the design speed of 1.2 Gsps, resulting in the 600 MHz IF band being aliased onto 400 MHz of bandwidth. The commissioning observations included determining pointing corrections and focus positions for each feed based on drift scans across the Moon and geostationary satellites, producing dynamic spectra of OVSA data to characterize the RFI environment and look for any evidence of non-linearity or rapid gain variation, and taking spectra on and off the Moon to make rough measurements of system temperature for each feed. The observations of dynamic spectra identified frequent gain fluctuations in one polarization; by measuring power levels throughout the signal path, I identified that these fluctuations were coming from that polarization's optical transmitter, which was then replaced.

The spectral measurements identified that RFI was dominating the total power in the low-frequency (1-6 GHz) feed, as seen in the spectrum in Figure 3.2 (the particular spectrum in this figure was actually taken with the Starburst correlator). Other team members purchased and installed a 1.1 GHz high pass filter on the front end and a 2.1 GHz notch filter. Installation of these filters also removed a number of the other RFI peaks across the spectrum, which must have been aliased from the main RFI peaks. Figure 3.3 shows a system temperature spectrum measured on/off

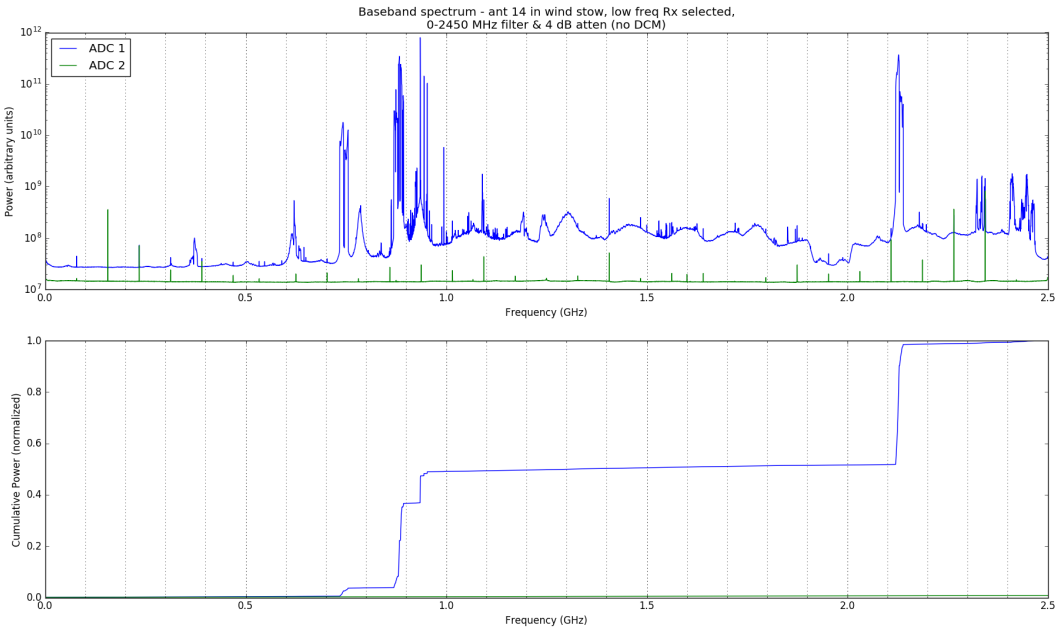

Figure 3.2 Baseband 0-2.5 GHz spectrum from OVRO 27-m antenna A taken in the stow position with the low-band feed; top panel is the spectrum and bottom panel is the cumulative spectrum, showing the fraction of the total signal power coming from below a given frequency. We used a 2.45 GHz low pass filter and passed the signal directly to the Starburst correlator, bypassing the downconverter, to take the spectrum. RFI at 0.9 and 2.1 GHz dominates the total power in the spectrum. The blue line shows the spectrum from the feed on sky and the green line shows the spectrum from the correlator with an empty input, to illustrate the narrowband artifacts that originate in the correlator.

the Moon at 0.5-6 GHz before the installation of the RFI filters, with an approximate system temperature of 400 K in the clean parts of the spectrum; to the best of my recollection, the filters did help improve the low-band system temperature somewhat, but I did not end up characterizing the new system temperature before the conclusion of the Starburst project.

3.2 Starburst back end: Scientific requirements and technical specifications

The goal of the Starburst program was to detect and characterize coherent stellar radio bursts, especially events analogous to solar Type II bursts, which are associated with the shock fronts formed by fast-moving coronal mass ejections. With two antennas, Starburst offered a much lower sensitivity than facilities such as the VLA, but much more observing time; Starburst's goal was therefore to detect the infrequent, luminous radio bursts that are expected in association with the most extreme

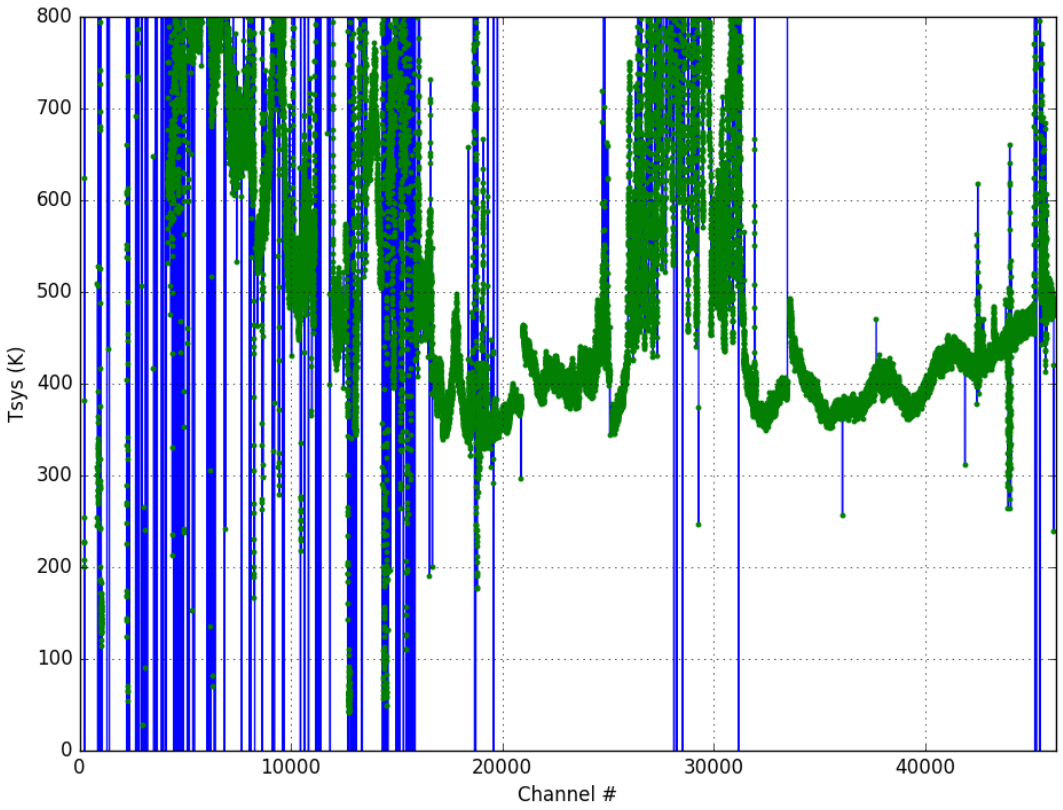

Figure 3.3 Approximate system temperature spectrum of the ant14 low-band feed at 0.5-6 GHz based on autocorrelation spectra taken with the OVSA backend. The frequency axis corresponds roughly to 0.5-6 GHz. Tsys was estimated by comparing spectra taken on and off the Moon, subtracting from them a spectrum taken with the front end attenuator at 30 dB (essentially with no front end signal). The assumed brightness temperature of the Moon is 250 K. The blue lines interconnect the green data points.

stellar flares.

The front ends of the 27-meter antennas were designed and built to fit the needs of the EOVSA project, although the wide bandwidth and cooled receivers made them a good fit for observing stellar radio bursts. The design of the Starburst backend was therefore guided by the goal of optimizing stellar radio burst observations, as well as support for other observations such as radio transient followup, given the properties of the front end.

The guiding principles identified for the Starburst system design, and corresponding design choices, were:

- *Maximize instantaneous bandwidth and total frequency coverage.* The Star-

burst system was designed to have an instantaneous bandwidth of 5 GHz, with 4 fixed-frequency local oscillators (LOs) to enable observation in one of four bands: 1-6 GHz for the low band feed, and the three bands of 5-10 GHz, 9-14 GHz, and 13-18 GHz to cover the high band feed. The 1-6 GHz band is the main band for stellar coherent radio burst observations.

- *High dynamic range.* Harmonic structure is one of the signatures of solar CME-associated radio bursts, so it is important to avoid instrumental effects that might mimic this signature. Given that Jansky-bright coherent radio bursts have been observed on active M dwarfs in only dozens of hours, we consider the possibility of an exceptionally bright 10 Jy burst. Compared to a dynamic spectrum sensitivity of 10 mJy in 64 MHz and 30 seconds, we want to achieve a dynamic range of 30 dB to keep aliased stellar emission below the noise levels, although 25 dB would take us quite far. Dynamic range is also important to prevent strong RFI from contaminating additional regions of the spectrum. The Starburst system uses an IQ downconversion scheme, so our dynamic range requirement translates into a sideband rejection requirement.

- *Full polarization.* Many coherent radio bursts have a strong Stokes V signature, so we decided to observe all polarization products, which combine to calculate Stokes I and V.

- *RFI rejection.* The low-frequency band has strong RFI. We want narrow enough channels to reject RFI while saving as much of the clean spectrum as possible. The correlator was designed with flexible channel width, capable of producing channels as narrow as 300 kHz. In addition, the correlator was able to return kurtosis as well as the standard correlation products, and we planned to experiment with using kurtosis for RFI rejection.

- *Flexible time resolution.* Integration times of 1 second are more than short enough for observing the minutes-long emission associated with CMEs. However, a number of stellar coherent radio bursts have been observed with >1 Jy flux and variability on millisecond timescales. The Starburst correlator was designed with flexible time and frequency resolution, enabling diverse observing modes to characterize different aspects of stellar bursts and making the backend flexible enough to support other observations with diverse science goals.

- *Gain stability.* The complex bandpass of the cross-correlation between the two antennas must be stable enough to be calibrated by periodic observations of calibration sources. We did not reach the point of testing whether astronomical data could be effectively calibrated. This principle did not particularly influence design decisions, as we expected sufficient gain stability of cross-correlations at 1-18 GHz without special precautions.

- *Delay tracking.* The backend must remove delay (phase slope versus frequency due to different arrival times at the two antennas) sufficiently to avoid losing sensitivity during channelization and time integration. The Starburst system implemented coarse delay tracking by applying a time delay between the signal voltages when they were digitized, with an option for fine delay tracking (applying a phase slope in the correlator FFT to remove the residual delay) that was not tested on astronomical observations.

- *Simplicity of implementation and maintenance.* The Starburst program was a small experiment, led by grad students (Ryan Monroe and myself) and likely to involve other students in the future. As a small experiment, we tried to pick components that would speed up the design process and make maintenance or modification as simple as possible, using commercially available components in the downconverter modules and using simple control boards (LabJacks) rather than investing the overhead time to design printed circuit boards or program custom control boards.

3.3 Starburst back end: System design and implementation

I worked on project management for the Starburst project, collaborating with Ryan Monroe to lay out the overall system architecture and identify components to purchase. Setting up the infrastructure for the instrument was a time-intensive process from which I learned quite a bit of practical knowledge about how to set up an electronic system.

The Starburst back end is in an electronics rack in the OVSA correlator room. The signal from the 27-meter antennas enters the room on optical fiber and is converted back to an analog signal in the OVSA downconverter modules (DCMs). The OVSA DCMs for the 27m antennas were modified to include a 16 dB coupler after the optical receiver. From the coupler a -16 dBm signal is supplied to the Starburst rack: one signal per antenna per polarization.

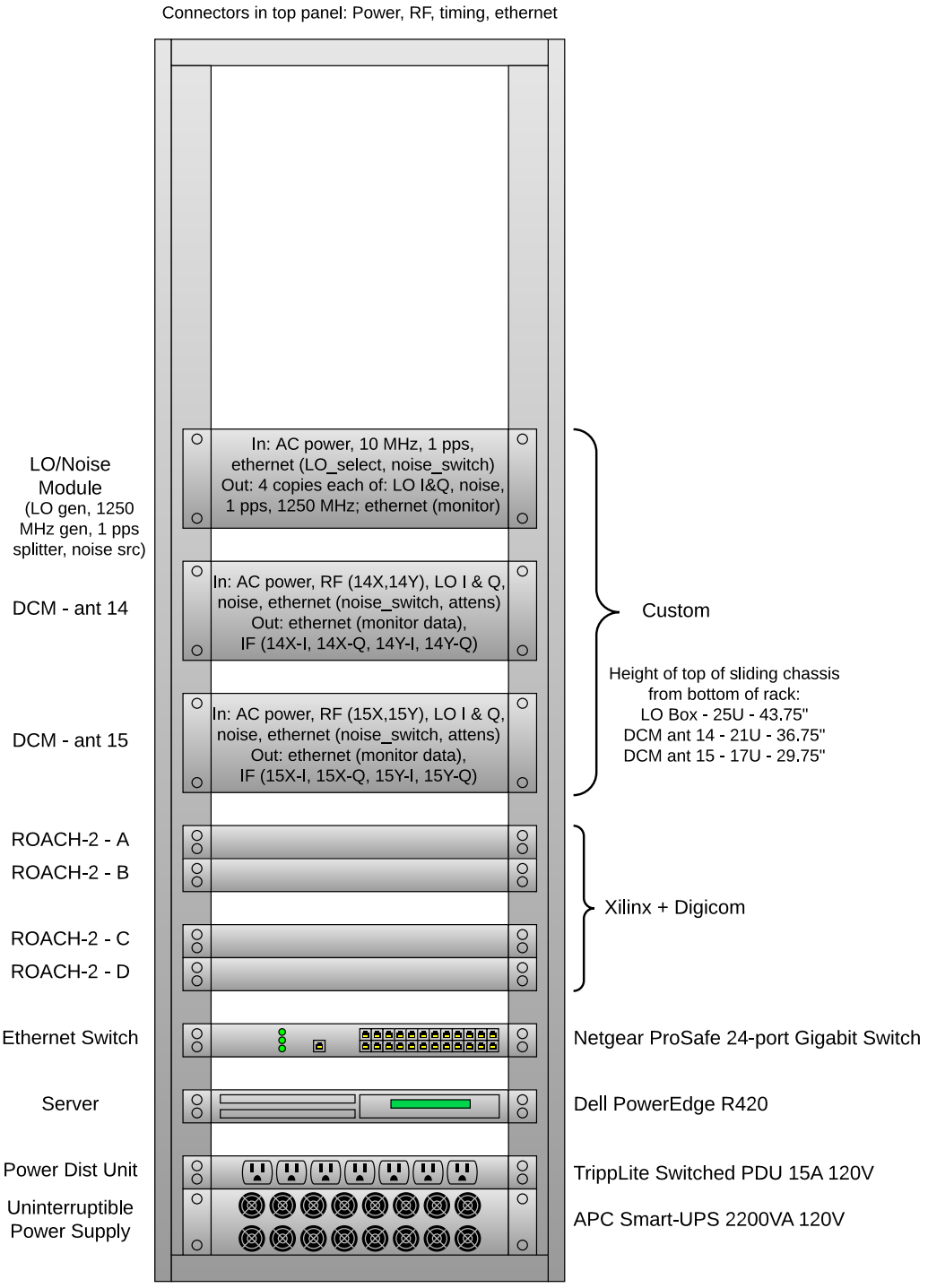

Figure 3.4 Layout of the subsystems within the Starburst rack. The LO/Noise Module generates LO signals for the downconverter and a 2500 MHz signal for the correlator FPGA clock. The downconversion system consists of two downconverter modules, one per antenna; each module has two signal paths, one for each polarization from an antenna. The correlator consists of four ROACH-2 boards, each of which digitize one polarization from one antenna.

The Starburst rack is designed for electronics and is shielded against RFI. Figure 3.4 shows the contents of the Starburst rack, illustrating the large-scale modules that make up the Starburst back end. The LO/Noise Module generates LO signals for the downconverter and a 2500 MHz signal for the correlator FPGA clock. The downconversion system consists of two downconverter modules, one per antenna; each module has two signal paths, one for each polarization from an antenna. The correlator consists of four ROACH-2 boards, each of which digitize one polarization from one antenna. The LO/Noise Module and DCM chassis are on slides (like drawers), which proved invaluable during installation and troubleshooting. Although the chassis were specified for the width of our rack, the chassis with slides did not fit the rack, requiring a day of time and testing every type of spacer to be found at OVRO and every possible orientation of the mounting hardware before we successfully installed the sliding chassis into the rack. OVRO staff modified the top panel of the rack to provide entry points for RF signals, clock signals, ethernet and power. Ryan and I sent the back panels of the chassis for custom modification to provide entry points for signals and power and to etch labels by the connectors; the custom labels were beautiful but came with the unexpected result that they were etched on the inside of the chassis instead of the outside as intended. The exercise of producing the rack diagram (Figure 3.4) itself proved invaluable, when Sandy Weinreb pointed out that the original design, which placed sliding chassis above head height, was negating the purpose of the sliding chassis.

The server was purchased in collaboration with Patrick Shopbell, with 7 TB of storage space providing enough room to store multiple years of Starburst data and 64 TB of memory enabling fast processing of large data sets in CASA. The power distribution unit enabled remote power cycling of the other rack components, which was especially helpful for the ROACH-2 boards. The uninterruptible power supply stored up to 15 minutes of power for the Starburst system in a battery.

I used the rack diagram to identify and purchase cables of appropriate length to allow the sliding chassis to move freely and connectors to mount in the chassis and rack. I also produced a network diagram for the Starburst system (Figure 3.5), working with Dale Gary and Cahill computing staff to assign IPs for the Starburst subsystems. Finding the Starburst computer on the OVSA network proved to be a long afternoon tracing network packets with Wireshark. The correlator boards are interconnected with 10 gigabit ethernet to transfer data after an FFT and before cross-correlation. The output of the correlator travels to the Starburst computer via

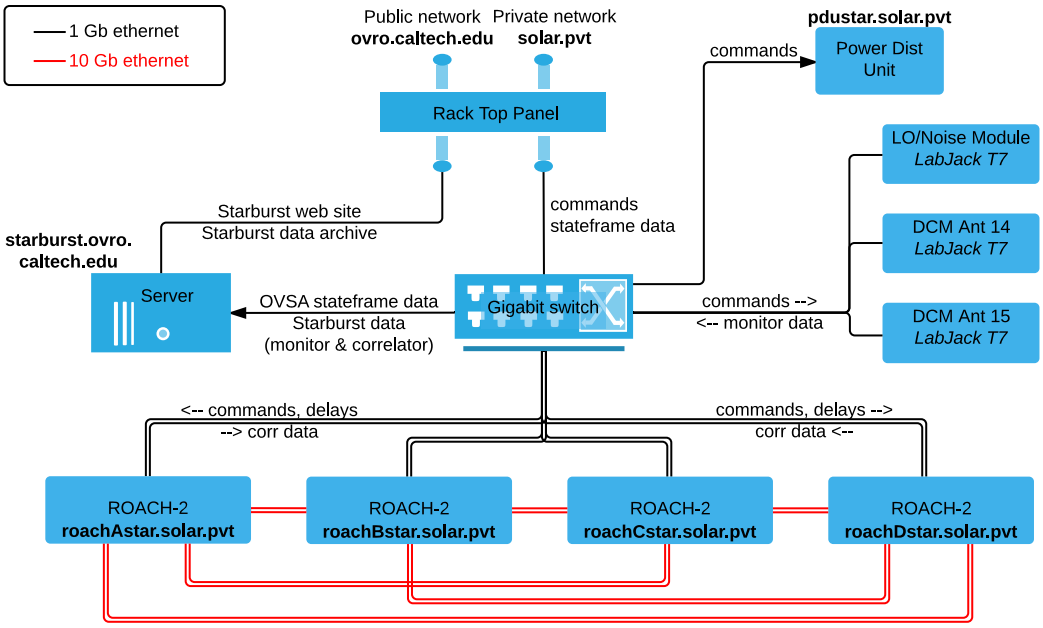

Figure 3.5 Starburst network diagram, showing ethernet connections inside the Starburst rack. Ethernet connections are labeled with the data they transmit, and marked with an arrow if the data flow is unidirectional. Double lines represent two ethernet cables between the same two elements. The correlator boards are interconnected with 10 gigabit ethernet to transfer data after an FFT and before cross-correlation. The output of the correlator travels to the Starburst computer via 1 gigabit ethernet through the gigabit switch, imposing data rate limits that constrain the relationship between channel width and integration time.

1 gigabit ethernet through the gigabit switch, imposing data rate limits that constrain the relationship between channel width and integration time.

3.3.1 Starburst downconverter and correlator

The design and implementation of the Starburst downconverters and correlator was led by electrical engineering graduate student Ryan Monroe, and will be described in an upcoming publication about the Starburst instrument (Monroe, Villadsen, et al. in prep). Many of the parameters of the Starburst downconverter and correlator design are listed above in Section 3.2, but a brief complementary description follows.

The Starburst downconverter uses an I/Q downconversion scheme, mixing the full-bandwidth RF signal with two signals at the LO frequency that are 90° out of phase, producing two signals that consist of different linear combinations of the upper

side band (frequencies above the LO frequency) and lower side band (frequencies below the lower side band). After the mixer, a 2.5-GHz low-pass filter restricts each sideband to 2.5 GHz bandwidth and therefore restricts the total observing band to 5 GHz bandwidth centered on the LO frequency.

The I and Q signals from the DCMs enter the correlator, with the I and Q signal from one antenna/polarization entering each correlator board, where they are digitized with a clock rate of 5 Gsps. The correlator follows an FX structure. The signals are delayed by a certain number of samples when they enter the correlator, where this delay is sent to the correlator by the control system. Then the digitized voltage time series of the I and Q signals are then transformed to the frequency domain using a Polyphase Filter Bank (PFB), a modified Fourier transform which gives a sharper and flatter frequency channel shape. The I and Q signals are then separated in the frequency domain using frequency-dependent parameters that are measured in a calibration routine every time the correlator is reset (this correlation routine involves using an input from a signal generator to sweep a single-frequency tone across the input RF frequency range and measuring the response to this tone in I and Q). The signals are then transmitted between correlator boards and each correlator board is given responsibility for a certain sideband and cross-correlation, then these data are integrated in time and collated into packets (one per correlator board) that are transmitted to the Starburst computer. Ryan wrote python code to parse the correlator packets.

The Starburst LO/Noise Module and DCMs both involved components with switches and components that generated monitor data. In addition to temperature detectors in all modules, in the LO/Noise Module, there was a 4-way switch to select between LO frequencies; and in the DCMs, there were switches to select between input from the RF (sky) signal and from a calibration signal, variable attenuators to control power levels in the DCM signal chain, and power monitors to measure the output power from the DCM. To control the switches and variable attenuators and collect the monitor data, we decided to use LabJacks, a simple form of control board that has both analog and digital pins for both input (collecting monitor data) and output (driving switches). OVRO staff designed a custom supplementary board that enabled us to use the LabJacks to control the variable attenuators, which required a short-time-duration pulse to cause their settings to change. Caltech undergraduate Loko Kung, who wrote the control system run on the 27-m front end computers, also wrote a Starburst-specific python wrapper for the LabJacks to carry

out commands such as changing bands, changing variable attenuator settings, and collecting monitor data.

I enthusiastically recommend LabJacks to anyone seeking simple control hardware that will work off-the-shelf. LabJack drivers were easy to install, and connecting to the LabJacks worked on the first attempt and every time after that. A simple python module is available for controlling and reading from the digital and analog input and output pins of the LabJack, making it a joy to operate.

3.3.2 Control software

I led the development of software for the Starburst system, which was a significant fraction of the work I did on the Starburst project. Since Starburst was discontinued early in commissioning, I had not yet written automated versions of the data packaging and calibration software. Most of my software work for Starburst was making modifications to the OVSA software to enable Starburst to observe simultaneously and to provide functionality needed by both OVSA and Starburst. Starburst used the overall framework for antenna control developed by the OVSA. I modified the OVSA's control code to support transitioning antenna control between the OVSA and Starburst, and to send commands to and collect monitor data from the Starburst downconverters and correlator. I added functionality to the OVSA control code to support tracking sidereal targets, to determine source visibility with the 27m antennas, and to force the 27m antennas to autostow if they were pointed too close to Sun for more than a few seconds.

I also wrote auxiliary scripts for observation planning, to plot the rise and set times of bright calibrators and their distance from the Sun and Moon, to find bright calibrators or geostationary satellites within a certain distance of any other source and above a certain flux limit, and other related tools. I also adapted OVSA code for Starburst to produce files for tracking sources in the custom formats used by OVSA.

Finally, I wrote preliminary (simple) scripts to update delays and send them regularly to the Starburst correlator while collecting and collating data and applying lobe rotation. Lobe rotation takes out the time-varying phase offset seen across the whole band, which is the phase offset at the LO frequency due to delay. Coarse delay correction in the correlator removes delay from the IF frequencies (0 to 2.5 GHz instead of the original frequencies), so the phase shift of the data due to delay at the LO frequency is not accounted for in the correlator.

3.4 Starburst back end: Commissioning

We brought the Starburst back end from Caltech campus to OVRO in January 2016. Figure 3.2 shows an autocorrelation spectrum with ant14 taken with the Starburst correlator on that trip. Many of the commissioning steps are described above. Other tasks included checking for non-linear gains in the signal path by measuring the linearity of power entering and exiting the Starburst downconverters as a function of front end attenuation, and troubleshooting variable, overall low power levels in certain signal paths in the DCM. The signal power exiting the DCMs was lower than planned based on the system design, which used an idealized power budget (not accounting for cable losses etc in the design stage, although James Lamb later prepared an excellent, detailed frequency-dependent power budget). Combined with gain slope across the band, this resulted in prohibitively low sensitivity. We resolved this by removing the variable attenuators from the DCMs and adding an extra stage of amplifiers, using wideband amplifiers available at OVRO that had been purchased for the CARMA telescope. Commissioning of the back end progressed gradually as it occurred simultaneously to and depended on troubleshooting the front end, which is described above.

Only one 27m had a front end installed, so we tested the Starburst correlator by observing geostationary satellites and bright astronomical calibrators with a cross-correlation between a small solar antenna ("ant11") and the 27m (ant14). Figure 3.6 shows the final Starburst observation, a cross-correlation on Cygnus A which successfully used I/Q sideband separation. We detect coherent phases in the center part of the band but lose the outer parts, which cannot be recovered by integrating over time. This is in part because the small solar antennas have 2.1-GHz high pass filters, which were installed because the wide field of view of the small antennas makes them especially susceptible to the bright RFI at 2.1 GHz and below. The loss of the higher frequency edge of the band may be due to a gain slope across the band. The maximum power from the front ends of the small solar antennas is almost 10 dB lower than that from the 27m antenna. Starburst did not have the amplification necessary to achieve good sensitivity for the small solar antennas; the upper edge of the band likely has lower overall gain and is lost in the noise floor of the Starburst back end.

Commissioning of the Starburst project also included test runs for optical photometry of the Starburst targets. Paul Gardner, who works with the CSU San Bernardino observatories, joined the Starburst team to lead photometric monitoring of Starburst

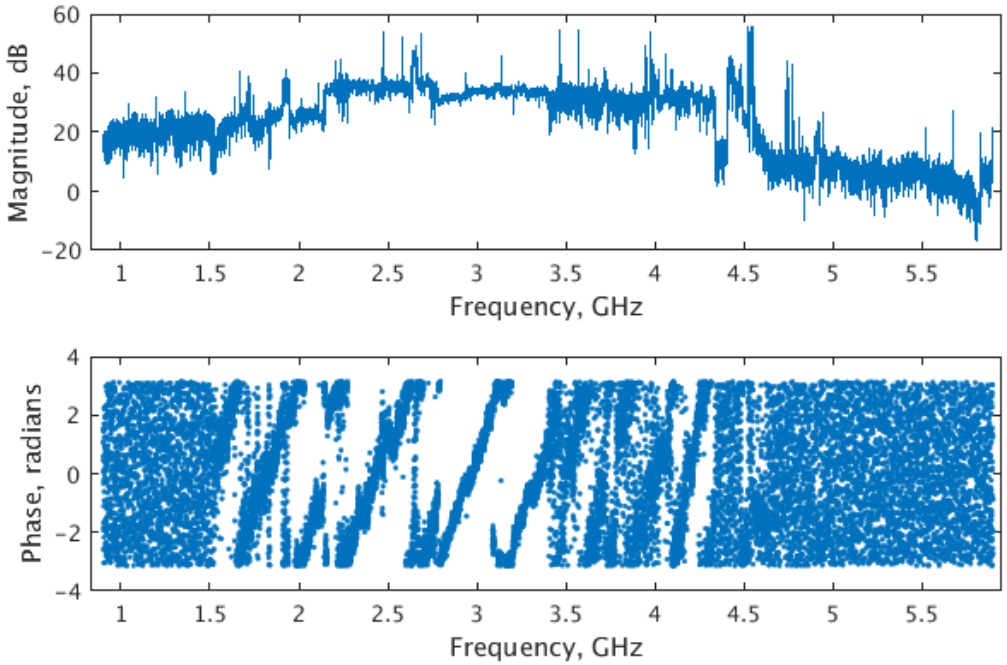

Figure 3.6 A cross-correlation spectrum of Cygnus A taken with the Starburst back end, using signals from one 27-m antenna and one small solar antenna. The loss of signal in the outer parts of the band is likely due to the gain profile and low power levels of the small antenna.

targets with a small optical telescopes, with the goal of conducting simultaneous radio and optical observations once Starburst started its radio observations. Navtej Singh wrote a pipeline to calibrate and extract time series from the optical photometry data. Paul led a few nights of test observations on EQ Peg, and I used Navtej's pipeline to do an initial reduction of these data. Figure 3.7 shows the time series of EQ Peg and a field star from this test observation, with a small flare detected on EQ Peg.

3.5 Conclusion

Ultrasound structural testing of the 27-m antennas was conducted by an outside contractor at the beginning of the OVSA expansion project in 2013. However, in April 2016, OVRO staff, noting a rusted hole in the support structure of one of the 27-m antennas, tested the thickness of the metal and found that the metal support beams were almost entirely rusted through; Russ Keeney reported poking a hole through the metal with a pencil, which resulted in water draining out of the hole. The ends of the support beams, which were hollow pipes, were not sealed, so rain had ac-

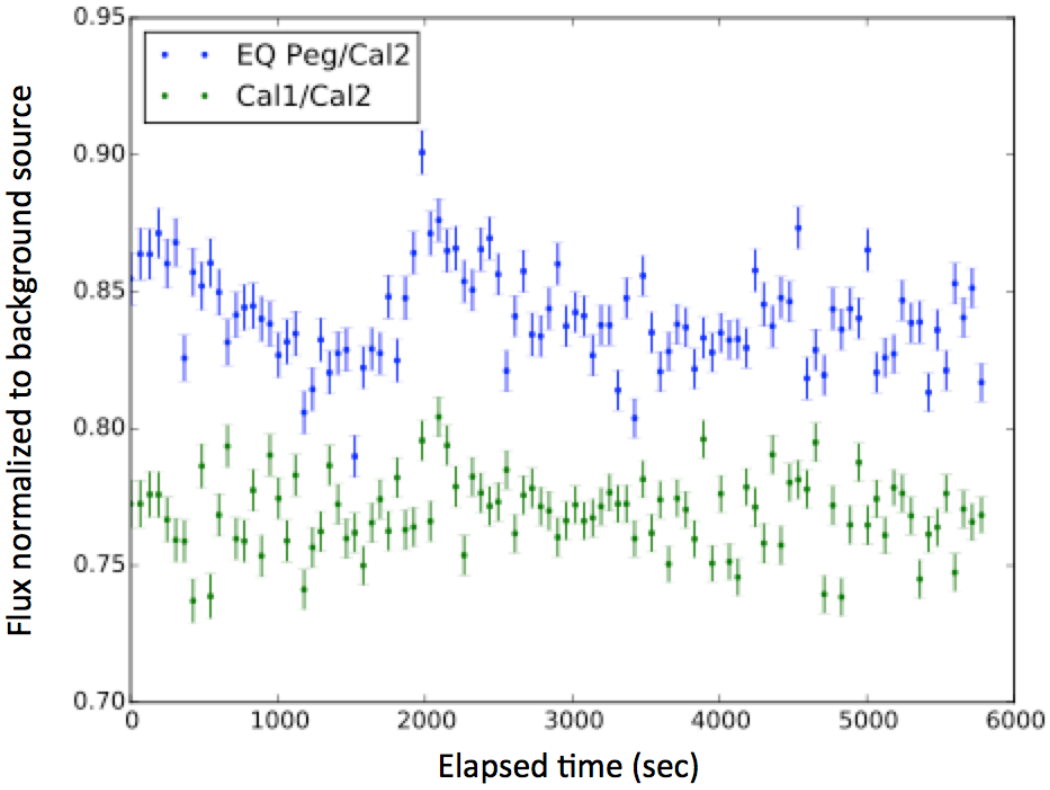

Figure 3.7 Optical photometric time series of EQ Peg, taken as a test observation to prepare for simultaneous Starburst radio observations and photometry with a small optical telescope. The blue time series is EQ Peg's flux, divided by that of a bright field star ("cal2") in order to remove atmospheric variations. The green time series is the flux of another bright field star ("cal1") divided by that of cal2. EQ Peg produces a small flare during this time period that is not seen in the time series of the field star.

cumulated inside the pipes, causing them to rust. Further testing revealed that the structural problems were pervasive in both antennas, making it unsafe to install the cooled receiver on the second 27-m antenna and to conduct long-term maintenance on either antenna. The science goal of the Starburst project, stellar spectroscopy, requires the sensitivity and gain stability of the cross-correlation between two large antennas with cooled receivers, so at this point the Starburst project was discontinued except for a few calibrator observations conducted through September 2016 for inclusion in an upcoming Starburst instrument paper (Monroe, Villadsen, et al. in prep). This paper will publish a description of the design and testing of the Starburst downconverter and correlator.

The Starburst hardware was purchased for a 1-18 GHz solar spectrometer in Antarc-

tica (PI Dale Gary), which will combine the two Starburst downconverter modules to observe 10 GHz bandwidth simultaneously with a single antenna and which will use the spectrometer capabilities of the Starburst correlator. The Starburst system, designed for wideband stellar spectroscopy, will find new life as a spectrometer for our nearest star, the Sun.

3.6 Acknowledgements

The Starburst project was funded by the National Science Foundation's Advanced Technologies and Instrumentation program, Grant No. AST-1311098. The Starburst project used the cryogenic front ends developed for the OVRO 27-m antennas as part of the Owens Valley Solar Array expansion project, and also used the antenna array control code developed by the OVSA. Many people contributed to Starburst, from the Starburst team, the Owens Valley Radio Observatory staff and Cahill computing staff, and the Owens Valley Solar Array team. These people include: Gregg Hallinan (the Starburst PI), Ryan Monroe (lead engineer), Paul Gardner, Dale Gary, David Hawkins, Mark Hodges, Russ Keeney, Althea Keith, Oliver King, Loko Kung, James Lamb, Anu Mahabal, Stephen Muchovej, Kjell Nelin, Gelu Nita, Anthony Readhead, Patrick Shopbell, Navtej Singh, and David Woody. I would like to express particular gratitude to the OVRO staff and the OVSA team for taking the time to answer all my questions about radio interferometry and instrumentation. While the Starburst project came to an early close, I am grateful to have had the opportunity to learn so much and I look forward to future involvement in development and commissioning of radio observing facilities.

Chapter 4

A WIDEBAND SURVEY FOR COHERENT RADIO BURSTS ON ACTIVE M DWARFS

Abstract

Wideband spectroscopy of coherent radio bursts can be used to trace source motion in stellar coronae, offering the potential to detect stellar coronal mass ejections. Coherent radio bursts are emitted at low harmonics of either the plasma frequency or the cyclotron frequency, diagnosing plasma density and magnetic field strength in the source region. The upgrades to the Jansky Very Large Array (VLA) enable ultra-wide bandwidth observations, which are sensitive to sources at a wide range of coronal heights. We have conducted a 58-hour survey of 5 nearby active M dwarfs with the VLA, simultaneously observing in three frequency bands to cover a subset of 224-482 MHz and 1-6 GHz. These stars are prolific sources of coherent radio bursts, with bursts detected in 13 out of 23 epochs. Among the most luminous bursts is an event on YZ CMi, with features indicating apparent source motion of > 0.1c. Luminous bursts are most abundant in L band, 1-2 GHz, with the stars spending $\sim$10% of the total observing time producing coherent bursts with 1-2 GHz luminosity (assuming no directional beaming) greater than $2\text{x}10^{14}$ erg/s/Hz, an order of magnitude greater than their typical quiescent radio luminosity. We calculate lower limits on rates of stellar coherent radio bursts for current transient surveys, finding that coherent radio bursts from active M dwarfs will be among the dominant transient populations at 1-2 GHz. The frequency of luminous bursts peaks at 1-1.5 GHz, declining at higher and lower frequencies, implying that the population of stellar bursts observed by this survey is associated with phenomena that are confined to the low corona, rather than stellar eruptions.

4.1 Introduction

The Sun produces intense bursts of emission at low radio frequencies, which caused it to become the second detected astrophysical radio source after the Galactic center (Hey 1946; Southworth 1945; Orchiston 2005). These bursts are classified according to their morphology in the time-frequency plane ("dynamic spectrum"), reviewed in Bastian et al. (1998). As a picture for the origin of the different types of bursts has emerged, they have proved to have significant diagnostic power for

processes in the solar corona. Many of the classes of bursts are powered by coherent emission mechanisms, plasma emission or electron cyclotron maser (ECM) emission. Two types of coherent bursts that track material escaping from the solar corona are Type II and Type III bursts. These bursts occur at the local plasma frequency, and their frequency declines over time as a coronal source moves outwards into lower densities. Solar Type II bursts trace the motion of shock fronts formed by coronal mass ejections (CMEs) at speeds of order 1000 km/s, passing through regions with progressively lower plasma frequency in matter of minutes. Solar Type III bursts are produced by electron beams moving at speeds of order 10% of the speed of light, with frequency decreasing exponentially on a timescale of seconds; when these bursts occur at low frequencies, they indicate that energetic electrons (and likely protons as well) are escaping the solar corona on open magnetic field lines. Both of these classes of bursts are predictive of solar space weather events that impact Earth: coronal mass ejections and solar energetic protons (Kouloumvakos et al. 2015).

We can characterize the space weather environment experienced by extrasolar planets by searching for stellar coherent radio bursts analogous to solar Type II and Type III bursts. This is particularly important for M dwarfs, which retain their vigorous youthful magnetic activity for hundreds of millions to billions of years (West et al. 2008). Active M dwarfs have a high rate of energetic flares (Lacy et al. 1976), with potentially dramatic consequences for planetary atmospheres (e.g., Lammer et al. 2007; Khodachenko et al. 2007; Segura et al. 2010). Current models of how stellar ejecta impact planetary atmospheres around active stars must rely on extrapolating the solar relationships between flares and CMEs/protons (Yashiro & Gopalswamy 2009) to apply to the high-energy flares and strongly magnetized corona of active M dwarfs. Wideband radio spectroscopy of stellar coherent radio bursts can track outwards-moving coronal sources, offering the potential for direction observations of stellar eruptions.

Coherent radio bursts are abundant on active M dwarfs, dominating the population of radio flares observed on these stars below 5 GHz (Bastian 1990). Dynamic spectroscopy has helped to characterize these bursts, finding features such as striae with rapid frequency drift (Osten & Bastian 2008), rapid time variability, and strong circular polarization that provide evidence that ECM may be responsible for many of these bursts. A number of coherent radio bursts in stellar atmospheres are also attributed to plasma emission (Stepanov et al. 2001; Osten &

Bastian 2006), a promising sign that events analogous to the solar Type II and Type III plasma-frequency bursts may occur in stellar atmospheres. The search for the radio signature of these space weather events benefits from wide fractional bandwidth ($\nu_{\rm max}/\nu_{\rm min} >> 1$), which enables tracking a source as it moves across multiple coronal density scale heights, and observations at low frequencies, which are sensitive to sources at greater distances from the star. So far, dynamic spectroscopy of stellar coherent radio bursts has occurred with a maximum bandwidth (for observations with detected bursts) of $\nu_{\rm max}/\nu_{\rm min} \sim 1.5$ (Osten & Bastian 2008) and mostly at frequencies above 1 GHz. Exceptions include observations of YZ CMi at 425-435 MHz by Bastian et al. (1990) and at 10-90 MHz and 110-190 MHz with LOFAR by Crosley et al. (2016). The upgraded Karl G. Jansky Very Large Array (VLA) offers wide instantaneous bandwidth and low observing frequencies, making it a powerful instrument for searching for stellar eruptions.

We have conducted a 58-hour survey of a sample of 5 active M dwarfs with the VLA, using the VLA's subarray capabilities to achieve ultra-wide bandwidth over a subset of frequencies from 224-482 MHz and 1-6 GHz. We analyze the results of this survey in a series of three papers. In this paper (Paper I), we present the ensemble of coherent radio bursts detected by the survey, consider the physical origins of an exceptional event on YZ CMi, and predict rates of stellar coherent radio bursts for upcoming transient surveys. Papers II and III analyze in detail a series of coherent bursts on UV Cet and AD Leo, respectively, accompanied by simultaneous 8.2-8.5 GHz high-resolution imaging with the Very Long Baseline Array (VLBA).

4.2 Observations

The survey consists of 58 hours of VLA observations in 2013 and 2015, summarized in Table 4.1. The observations consist of 2- and 4-hour blocks on individual stars, with 1-second integrations. The targets are well-known flare stars: AD Leonis (M3V), binary BL & UV Ceti (M5.5V+M6V), binary EQ Pegasi AB (M3.5V+M4.5V), EV Lacertae (M3.5V), and YZ Canis Minoris (M4V); spectral types are from Henry et al. (1994). Both binaries have orbital separations of a few arcseconds, unresolved by most of the VLA observations; in this paper we use the names "UV Cet" and "EQ Peg" to refer to the unresolved binary system unless otherwise specified.

A key feature of this survey is its extremely wide fractional bandwidth, defined

Table 4.1 Summary of observations.

Star	Date	Duration (hrs)	Frequency (GHz)	Flux Calibrator	Gain Calibrator	VLA Configuration
AD Leo	4/24/2013	2	2-6	3C147	J1111+1955	D
	5/26/2013	2	1-6	3C147	J1111+1955	DnC
	6/2/2013	2	1-6	3C147	J1111+1955	DnC→C
	7/27/2013	2	1-6	3C147	J1111+1955	C
	5/12/2015	2	0.22-0.48, 1-4	3C286	J1111+1955	B→BnA
	5/13/2015	2	0.22-0.48, 1-4	3C286	J1111+1955	B→BnA
	7/5/2015	4	0.22-0.48, 1-4	3C286	J1111+1955	A
	7/19/2015	4	0.22-0.48, 1-4	3C286	J1111+1955	A
	9/5/2015	4	0.22-0.48, 1-4	3C286	J1111+1955	A
UV Cet	5/26/2013	2	1-6	3C48	J0204-1701	DnC
	6/2/2013	2	1-6	3C48	J0204-1701	DnC→C
	8/24/2013	2	1-6	3C48	J0204-1701	C
	5/15/2015	2	1-2	3C147	J0204-1701	B→BnA
	5/16/2015	2	0.22-0.48, 1-4	3C147	J0204-1701	B→BnA
	7/4/2015	4	0.22-0.48, 1-4	3C147	J0204-1701	A
	7/18/2015	4	0.22-0.48, 1-4	3C147	J0204-1701	A
	9/6/2015	4	0.22-0.48, 1-4	3C147	J0204-1701	A
EQ Peg	5/15/2015	2	0.22-0.48, 1-4	3C147	J2254+2445	B→BnA
	5/16/2015	2	0.22-0.48, 1-4	3C147	J2254+2445	B→BnA
EV Lac	5/12/2015	2	0.22-0.48, 1-4	3C286	J2202+4216	B→BnA
	5/13/2015	2	0.22-0.48, 1-4	3C286	J2202+4216	B→BnA
YZ CMi	5/11/2015	2	0.22-0.48, 1-4	3C147	J0745+1011	B→BnA
	5/13/2015	2	0.22-0.48, 1-4	3C147	J0745+1011	B→BnA

Narrower bandwidth for AD Leo on 4/24/2013 and UV Cet on 5/15/2015 is due to bad data for some bands.

here as ν_{max}/ν_{min}, the ratio of highest frequency to lowest frequency observed simultaneously. Previous detections of stellar radio bursts have achieved continuous frequency coverage of ν_{max}/ν_{min} up to 1.4 (Osten & Bastian 2008) or have observed widely spaced narrow bands (e.g., Spangler & Moffett 1976); in contrast, solar spectrographs offer continuous frequency coverage for ν_{max}/ν_{min} of 10 to 100, with facilities such as the 10-1000 MHz Green Bank Solar Radio Burst Spectrometer and the 18-1800 MHz Culgoora Solar Radio Spectrograph. Our survey multiplies the fractional bandwidth achieved for stellar observations, with significant frequency coverage over ν_{max}/ν_{min} of 6 to 18. To achieve this wide bandwidth, we divided the VLA into three subarrays to observe three frequency bands simultaneously; the upgraded VLA's wideband feeds and WIDAR correlator enabled up to 2 GHz bandwidth in each band. The 2013 observations cover L band (1-2 GHz, 1 MHz channels), S band (2-4 GHz, 2 MHz channels) and C band (4-6 GHz, 2 MHz channels), with 9 antennas per subarray. The 2015 observations cover P band (224-482 MHz, 125 kHz channels) with 15 antennas to compensate for its lower sensitivity, and L and S bands with 6 antennas each. The wide bandwidth enables detection of sources across an order of magnitude in coronal density or magnetic field strength, increasing the probability of detecting narrowband bursts and enabling detailed characterization of burst morphology and source motion.

4.2.1 Calibration

The L, S, and C band data were calibrated using the CASA VLA calibration pipeline, using the Perley & Butler (2013a) flux density scale, followed by an additional round of automatic flagging with *rflag*. The P band data were also calibrated in CASA, following the calibration steps outlined in the CASA Guide "Basic P-band data reduction-CASA4.6" and using the Scaife & Heald (2012) flux density scale with L-band model images. We bypassed ionospheric TEC correction as it was not supported in CASA 4.6. The gains from a flux calibrator scan at the beginning or end of the observing block were applied to the entire P band data set, as gain interpolation from phase calibrator scans did not significantly improve calibration quality. No gain self-calibration was performed on any of the data; the sensitivities listed below are thus an upper limit to the achievable sensitivity with these data.

Stellar coherent radio bursts can have strong circular polarization. Measuring Stokes V provides two benefits: 1) the sense and the degree of circular polarization provide information on the emission mechanism and the magnetic field orientation in the source region; and 2) Stokes V has minimal contamination from background

sources, offering a better sensitivity to strongly polarized bursts than Stokes I. Cross-polarization leakage is expected to be a more significant source of error for P band circular polarization than for the higher frequency bands, because the P band dipole feeds can become misaligned and because cross-correlation is performed on linear polarization voltages in contrast to the circular polarization voltages used at higher frequencies. VLA P band polarimetry was still in commissioning at the time of observations and data analysis, but we performed a provisional polarization calibration for the P band data, correcting for cross-polarization delay and per-channel cross-polarization leakage. For polarization calibration, we assumed that the flux calibrator (3C147 or 3C286) was unpolarized. Perley & Butler (2013b) reports that the fractional linear polarization of these sources declines towards lower frequencies, reaching <0.5% for 3C147 and 8.6% for 3C286 at 1.05 GHz, the lowest frequency observed in that paper. Intrinsic polarization of the calibration sources therefore introduces at most a few percent error to the fractional polarization measured from our observations. Another source of error in polarization calibration may be time variation of cross-polarization leakage, which is not yet well-characterized.

4.2.2 Background Source Subtraction and Dynamic Spectroscopy

After calibration, we shift the phase center to the position of the target star. If the star is detected in a Stokes I or V image of an entire observation, then we use the star's imaged location as the phase center; otherwise we use the star's expected position based on positions and proper motions from Hipparcos and/or VLBA (Benz et al. 1998). In general, there is good agreement between expected and image plane position at 1-6 GHz, with more divergence in P band, likely due to the decision not to use a nearby phase reference source for this band.

The end product of the data reduction is dynamic spectra (such as in Figure 4.1) for all the observations, showing the evolution of stellar emission in the time-frequency plane. We produce dynamic spectra from interferometric data by averaging the visibility data over all baselines, generating a single complex visibility per channel per integration. The real part of this number corresponds to the center pixel in a dirty image of the data at this time and frequency. Thus, it is necessary to model and remove background sources from the visibility data before averaging over all baselines, to avoid the contribution of their sidelobes to the stellar flux.

Each observation was imaged in Stokes I using CASA's *clean* task with multi-

frequency synthesis with nterms=2, which allows flux of clean components to vary linearly with frequency. These images of background sources were produced using time and frequency ranges chosen to exclude any bright stellar radio bursts, since the sidelobes of stellar bursts can impact the clean model of the background sources. We masked any quiescent stellar emission out of the clean model image, then used CASA tasks *ft* to generate model visibilities from the background-only image. We then used *uvsub* to subtract the background-only model visibilities from the observed calibrated visibilities, leaving visibility data containing only the stellar emission. We used *tbavg*, a code developed by Stephen Bourke, Jackie Villadsen, and Gregg Hallinan, to average the visibilities over all baselines and extract the dynamic spectrum, combining all simultaneous L, S, and C band data to produce a single dynamic spectrum.

A pixel in the dynamic spectrum is a snapshot at a single time and frequency using a subarray of only 6 to 15 antennas, so it has limited uv coverage. The sidelobes of background sources can be very strong, effectively requiring high dynamic range imaging to prevent the dynamic spectrum from being dynamic range limited, especially at low frequencies and for fields with especially bright background sources. AD Leo has an especially bright background source (roughly 200 mJy at L band, 800 mJy at P band). Imperfect subtraction of a single bright background source causes striations in the dynamic spectrum, as exemplified by the AD Leo Stokes I dynamic spectrum in the fourth row of Figure 4.6b. However, background sources within the main lobe of the primary beam should not have significant circular polarization, which means that Stokes V dynamic spectra are mostly free of artifacts due to background sources. Table 4.1 reports the sensitivity achieved in each block for Stokes I and V, where Stokes I is often significantly less sensitive than V due to the impact of background sources.

4.2.3 Search for Radio Bursts

We searched for stellar radio bursts by inspecting the Stokes I and V dynamic spectra. For 1-6 GHz, we binned the dynamic spectra to 64 MHz and 150 seconds to achieve a typical RMS sensitivity of 1 mJy. For 224-482 MHz, we binned to 4 MHz and 300 seconds to achieve typical RMS sensitivity of 16 mJy in Stokes I and 6 mJy in Stokes V. We searched for bursts in both Stokes I and V because Stokes V offered greater sensitivity to circularly polarized bursts for fields with bright background sources, and Stokes I provided sensitivity to unpolarized and weakly polarized bursts.

Each pixel of the dynamic spectrum has a complex value, the result of averaging complex-valued visibilities over all baselines. A point source at the phase center produces a positive signal in the real component of the dynamic spectrum and no signal in the imaginary component. Bursts were identified visually as a cluster of pixels in the real component of the dynamic spectrum with signal-to-noise ratio greater than 3, where the RMS in each channel was calculated using the imaginary component of the dynamic spectrum. The other requirement for identifying a burst is the lack of comparable features in the imaginary component of the dynamic spectrum, which would indicate contamination by RFI or background sources. For example, the third row of Figure 4.6b shows a strong 1.1-1.6 GHz burst on AD Leo, which appears in the real components of Stokes I and V (columns 1 and 3) but not the imaginary components (columns 2 and 4).

The observed stars are known to produce broadband slowly-variable quiescent emission, attributed to incoherent non-thermal gyrosynchrotron radiation, with incoherent flares on timescales of minutes to days (reviews: Bastian 1990; Güdel 2002). Rather than incoherent flares, we are primarily searching for coherent radio bursts, where the signature of coherent processes is seen in narrow bandwidths or complex spectral structure, rapid time variability and high fluxes implying high brightness temperatures, and strong circular polarization of up to 100%. Our search methods are based on a signal-to-noise cutoff, so they may also identify some bright incoherent bursts, but the time-frequency structure and polarization of the detected events can be used to distinguish coherent bursts.

4.3 Results

Coherent bursts were detected in 13 out of 23 epochs on 4 of the 5 stars. Some epochs contained multiple, possibly distinct burst features, but we do not count individual bursts here due to the difficulty of distinguishing multiple simple bursts from a single complex event. Roughly half of the bursting epochs had peak fluxes of a few tens of mJy or more, allowing much finer binning of the dynamic spectra for detailed characterization of the bursts. These bright bursts include a series of events on UV Cet, discussed in Paper II; multiple events on AD Leo, discussed in Paper III; and one bright event on YZ CMi, presented in detail below in Section 4.5. Statistics of the luminosity distribution and rate of bursts inferred from the survey are presented in Section 4.6.

Figures 4.6a-4.7e show the Stokes I and V dynamic spectra of all observations,

with the color scale for each dynamic spectrum set to saturate at 6 times the RMS. All epochs with bursts have features with a high degree of circular polarization, although some substructure during bursts appears only in Stokes I. The strong circular polarization, combined in many cases with narrowband features in the frequency spectrum, favors a coherent emission mechanism for all of the bursts. The bursts have diverse morphology, which may be due to differences in the magnetic configuration of the source regions, the emission mechanisms, and/or the mechanisms supplying high-speed electrons to power the emission. Most of the bursts have no obvious analog in the classification system of solar radio bursts, but they may be driven by the same underlying physical phenomena, as discussed below for the YZ CMi event.

Most bursts are detected in multiple bands. Fewer bursts are detected in P band than at higher frequencies, in part due to P band's lesser sensitivity, and in part due to a decline in the rate of high-luminosity bursts compared to the lower half of L band (discussed in Section 4.6.1). All epochs with P band emission have bursts at higher frequency as well, most of which extend from the upper edge of the band, apparently a continuation of the higher frequency burst. The two exceptions are a burst in the final 2015 observation of AD Leo and one in the fourth 2015 observation of UV Cet, both of which bursts peak in P band with narrow burst fractional bandwidth. While some bursts show a downwards frequency drift, including on the timescale of seconds to minutes expected for space weather events, no bursts have both frequency drift on these timescales and emission that continues beyond the lower edge of the observed bands, which would be a signature of a disturbance continuing to move outwards from the star.

4.4 Mechanisms for Producing Stellar Radio Bursts

[This section is reproduced in the Introduction chapter of this thesis. It is included here for clarity since some version of this content will be included in the published version of this paper.]

Interpretation of the dynamic spectra of stellar coherent radio bursts hinges on three interrelated questions: 1) What is the emission mechanism, plasma radiation or electron cyclotron maser? 2) Is frequency drift in the dynamic spectrum due to source motion or to rotational modulation of highly-beamed emission? 3) Is the supply of high-energy electrons powering the emission stochastic (flares) or continuous (an auroral current system)? This section addresses the first two of these

questions in greater detail.

4.4.1 Emission Mechanism

The two emission mechanisms responsible for stellar coherent radio bursts are plasma emission and electron cyclotron maser emission (ECM). The electron cyclotron maser is expected to amplify emission at the fundamental cyclotron frequency only when the ratio of plasma frequency to cyclotron frequency, $\Xi = \nu_p/\nu_c$, is less than one, and at the second harmonic of the cyclotron frequency for $\Xi < 1.4$ (Melrose et al. 1984; Winglee 1985). This condition is not met in most of the solar corona, except for low heights above strongly magnetized active regions (Morosan et al. 2016), so plasma emission is the dominant mechanism for low-frequency solar coherent radio bursts. ECM is responsible for some of the higher-frequency (GHz+) solar bursts and for planetary radio aurorae. High brightness-temperature periodic radio emission, attributed to ECM, is also observed on some brown dwarfs (e.g. Hallinan et al. 2008) and on the magnetic A star CU Virginis (Trigilio et al. 2011).

Observational signatures that can be used to distinguish between the two mechanisms include:

- **Frequency.** Plasma emission is limited to low frequencies due to free-free absorption, with hotter coronal temperatures pushing the cutoff to higher frequencies. For plasma emission at harmonic s, $\nu = s\nu_p \propto \sqrt{n_e}$, the free-free opacity can be written in terms of the observing frequency in GHz $\nu_{\rm GHz}$, the temperature in MK T_6, and the density scale length H along the path of the emission:

$$\tau_{\rm ff} = 46\ s^{-4}\ \nu_{\rm GHz}^2\ T_6^{-3/2} \left(\frac{H}{30\ {\rm Mm}}\right). \tag{4.1}$$

  Assuming a high coronal temperature of 10^7 K and a low density scale height of 30 Mm, plasma emission at the fundamental harmonic sees $\tau_{\rm ff} = 3$ at 1.4 GHz, and the second harmonic at 5.6 GHz. In contrast, the Sun's 10^6 K corona limits fundamental and harmonic plasma emission to roughly 250 MHz and 1 GHz, respectively. However, as noted by Osten & Bastian (2006), gyroresonance absorption by higher harmonics poses a problem for ECM emission, especially in the hot coronae of flare stars, since gyroresonant opacity increases with temperature. It may be the case that both plasma emission and ECM must be emitted from a region with a sharp density gradient in order to escape from a stellar atmosphere.

- **Brightness temperature.** Coherent wave growth saturates at a brightness temperature that is dependent on emission mechanism (Melrose 1991). The theoretical predictions are roughly consistent with the range of brightness temperatures observed for plasma emission (low-frequency solar bursts: 10^8–10^{15} K, Dulk 1985) and ECM (Jupiter's decametric radiation: $> 10^{17}$ K, Dulk 1970).

- **Degree and sense of circular polarization.** Plasma emission at the fundamental is expected to be in the o-mode; the second harmonic is most often unpolarized but sometimes observed with weak o-mode polarization that is predicted not to exceed roughly 50% (Melrose et al. 1978). Combined with the constraint of free-free absorption that limits fundamental plasma emission to less than 1-2 GHz, this implies that strongly polarized emission above 2 GHz is likely produced by ECM. ECM, in the low-density limit, should be dominated by emission at the fundamental frequency in the x-mode, which can be fully circularly polarized. Propagating outwards from a north magnetic pole, o-mode corresponds to left circular polarization, and x-mode to right circular polarization.

- **Harmonic structure.** Both emission mechanisms can produce emission at the fundamental or second harmonic, although second harmonic emission is observed more commonly for plasma emission. For plasma emission, the coherent wave growth typically occurs in Langmuir waves, plasma density oscillations which cannot be radiated directly from the plasma. Instead a Langmuir wave must coalesce with another wave to produce transverse electromagnetic waves that can escape the plasma. Coalescence of a Langmuir wave and low-frequency turbulence produces emission at the fundamental frequency, whereas coalescence of two Langmuir waves produces second harmonic emission. These two processes can saturate at similar brightness temperatures, so that first and second harmonic are sometimes observed together at similar intensities in solar radio bursts; while the second harmonic is only weakly polarized, it is in the same sense as the first harmonic (Melrose et al. 1978). For ECM, in the low-density limit emission is expected only at the fundamental frequency, but in a region with varying plasma density, fundamental emission may occur simultaneous to second harmonic with the opposite sense of circular polarization (Winglee 1985), as has been observed in Jupiter's auroral kilometric radiation (Mellott et al. 1986). ECM may also

be responsible for solar spike bursts observed at frequency ratios implying the presence of 2nd to 6th harmonics, all of which had consistent weak circular polarization (Guedel 1990).

- **Fine structures in dynamic spectrum.** Treumann (2006) argues that fine structures in the dynamic spectrum showing rapid time variability and narrow bandwidth, observed in the auroral radiation of solar system planets, are a smoking gun for the electron-cyclotron maser.

4.4.2 Cause of Frequency Drift

For both emission mechanisms, the emission frequency depends on the conditions in the source region, so different frequencies correspond to different source regions. Solar, stellar, and planetary radio bursts all show evidence of frequency drift, seen in narrowband bursts or sub-bursts whose center frequency drifts upwards or downwards over time.

There are two potential causes for frequency drift in coherent bursts, i.e., two possible reasons that the source region is changing over time:

1. **Source motion.** Measuring frequency drift rate, combined with a model of the spatial variation of plasma density or magnetic field strength, enables estimation of an apparent source velocity. If the emission is at the plasma frequency or its harmonics, the time for a source with speed v (outwards is positive) to cross from starting frequency ν_1 to ending frequency ν_2 is:

$$t = \frac{2L}{v} \ln \frac{\nu_1}{\nu_2} = (60 \text{ sec}) \left(\frac{L}{30 \text{ Mm}} \right) \left(\frac{1000 \text{ km/s}}{v} \right) \ln \frac{\nu_1}{\nu_2}, \tag{4.2}$$

   where $L = H \cos \psi$, where H is the coronal density scale height, and ψ is the angle between the direction of propagation of the source and the density gradient.

   One type of moving coronal source, responsible for features with rapid frequency drift (covering an octave in frequency in ~0.1 sec), is an electron beam, moving at speeds of order 0.1c. Solar Type III radio bursts originate at plasma frequencies in the solar corona and sweep rapidly downwards to kHz frequencies corresponding to the interplanetary medium; these features are produced by high-speed electrons traveling outwards along open magnetic field lines.

Another type of moving coronal source is a coronal mass ejection. In regions where the CME exceeds the fast magnetosonic speed (roughly the Alfvén speed), the CME forms a shock front, which accelerates electrons to high speeds. These electrons stream ahead of the shock front, exciting plasma emission at the frequency corresponding to the ambient plasma density upstream of the shock. Solar Type II radio bursts are associated with CME shock fronts, with frequency drift rates that cross an octave in roughly one minute, corresponding to speeds of order 1000 km/s.

If the emission is at the cyclotron frequency or its harmonics, the time to cross follows a similar form to Equation 4.2, replacing density scale height with a magnetic scale length. Frequency drifts of narrow-bandwidth, short time duration substructure ("striae") in ECM emission may be due to motion of the "elementary radiation sources" producing the emission, as has been considered for substructure during an intense right circularly polarized 1.1-1.6 GHz burst on AD Leo (Osten & Bastian 2008).

2. **Rotational modulation.** Coherent emission can be highly beamed, particularly ECM, which is beamed into the thin surface of a wide cone. As the surface of the cone emitted from a particular region passes through our line of sight, we briefly detect emission from that region. Sweeps in frequency over time can be produced as a purely geometric effect, as the beamed emission from different source regions rotates into the line of sight. This effect has been modeled for Jupiter's decametric emission, using beam widths of order 1° as observed by Kaiser et al. (2000), to explain arc shapes in the dynamic spectrum with frequency structure varying over minutes to hours (Hess et al. 2008).

In order to detect bulk plasma motion in stellar coronae, it is important to distinguish between true source motion and frequency drift due to rotational modulation. The smoking gun to identify frequency drift due to rotational modulation is repetition of the emission feature once per stellar rotation period, such as seen on brown dwarfs (Hallinan et al. 2007) and chemically peculiar massive star CU Virginis (where Trigilio et al. 2011, interpret frequency drift as due to frequency-dependent propagation effects). Since our 2- and 4-hour blocks are shorter than the stars' rotation periods, we cannot confirm periodicity of radio bursts on the stars in this sample. Therefore, the bursts we detected may come from two distinct populations:

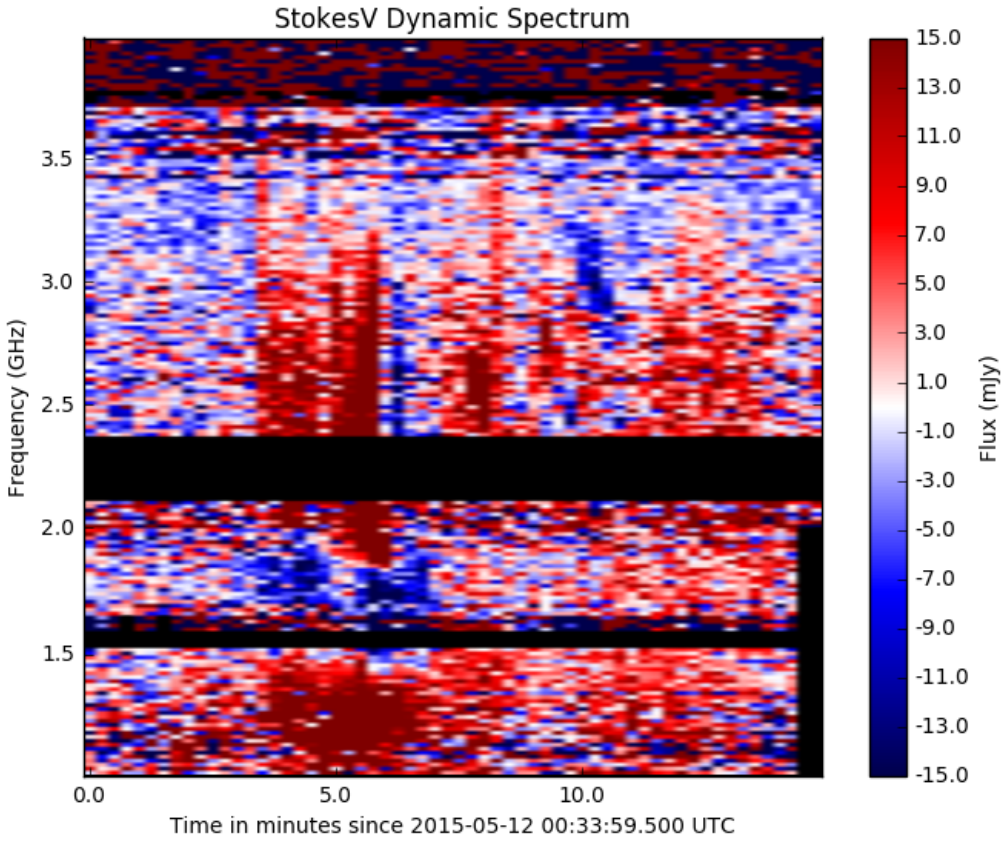

Figure 4.1 1-4 GHz Stokes V dynamic spectrum of YZ CMi during a bright radio burst. The dynamic spectrum is binned to a resolution of 16 MHz and 15 sec. The brightest component of the burst show alternating circular polarization with frequency.

stochastic bursts tracing source motion during stellar flares and eruptions, and periodic bursts powered by an auroral current system.

4.5 Bright Radio Burst on YZ CMi

In four hours of observations of YZ CMi, we detected one extremely bright event, shown in Figures 4.1 and 4.2 . Figure 4.1 shows the Stokes V dynamic spectrum at the time of the bright burst, binned to low resolution to highlight the circular polarization structure. The 10-minute burst, which spans 1-4 GHz, is preceded and followed by ongoing left circular polarized emission above 3 GHz throughout most of the 2-hour observing block. Figure 4.2 shows the burst in right circular polarization (RCP) with a finer time and frequency resolution to highlight short-duration substructure. The intense short-duration RCP burst subtructure has no analog evident in LCP. The burst is not detected in the P band dynamic spectrum

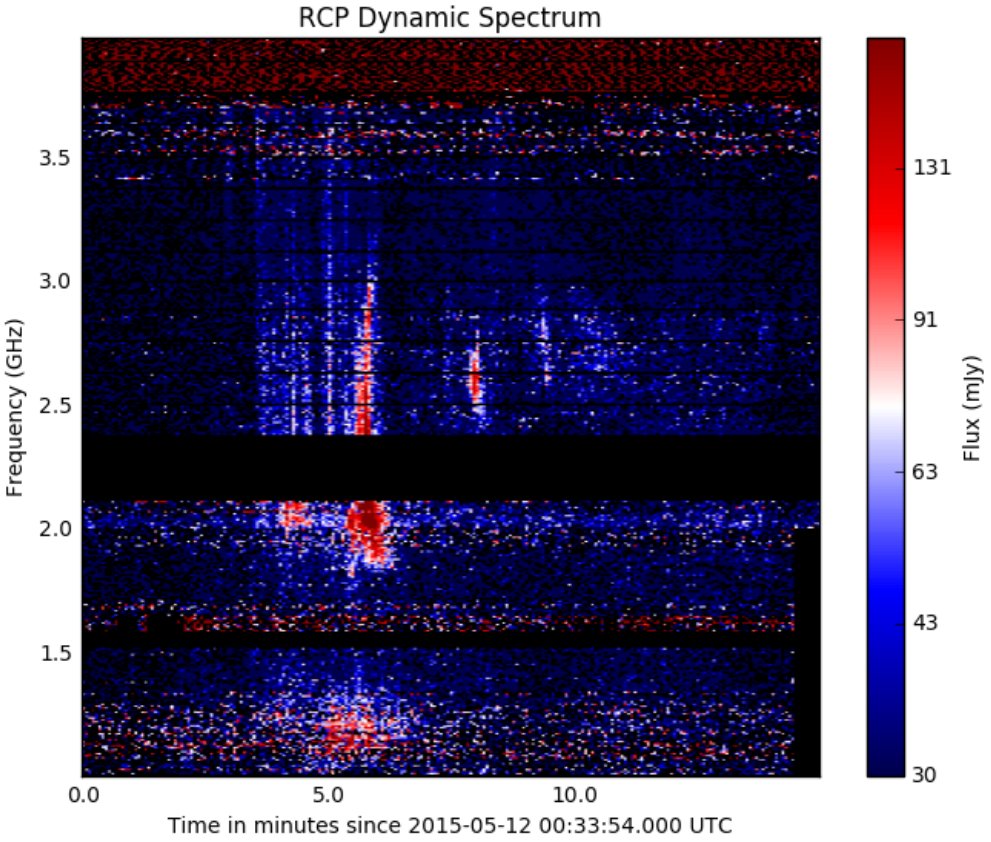

Figure 4.2 1-4 GHz RCP dynamic spectrum of YZ CMi during a bright radio burst. The dynamic spectrum is binned to a resolution of 8 MHz and 4 sec. The RCP component of the burst shows vertical features in the time-frequency plane, attributed to rapid frequency drift unresolved by the 1-second integration time. Note that for this strongly polarized burst, the RCP peak flux is almost twice as large as Stokes I due to the convention used to define RCP and LCP such that Stokes I = (RCP + LCP)/2.

nor in a cleaned image of the P band data (entire bandwidth) at the times of the higher frequency burst, 5/12/2015 0:35-0:50 UT. The non-detection in this image puts a 3σ upper limit of 6.0 mJy in Stokes I and 2.3 mJy in Stokes V on the P-band flux of the burst.

4.5.1 Emission mechanism

The burst shows a high degree of circular polarization up to high frequencies. In particular, the righthand polarized features from 2.4-3 GHz show roughly 60% circular polarization. Plasma emission is unlikely to be produced at the second harmonic with such a high degree of circular polarization (Melrose et al. 1978), implying that if the burst is plasma emission, it is most likely at the fundamental fre-

quency. However, as shown in Equation 4.1, if the fundamental plasma frequency is 3 GHz, the free-free opacity above the source region will be prohibitively high; $\tau_{\rm ff} \sim 3$ in a 10^7-K corona would require a density scale height of only 1.2 Mm, 1-2 orders of magnitude lower than the density scale height predicted by hydrostatic equilibrium. Therefore, we favor ECM as the likely emission mechanism for this burst, especially at the highest frequencies.

The most luminous part of the burst occurs from minutes 4 to 6 on Figure 4.1. During this time interval, the burst covers all of 1-4 GHz but is undetected at 224-482 MHz. If all of the 1-4 GHz emission is at the fundamental cyclotron frequency, this implies magnetic field strengths in the source region from 0.36 to 1.4 kG. The 1-4 GHz band is wide enough that it is possible to see first and second harmonic emission together. Winglee (1985) predict that a source region can amplify both fundamental and harmonic cyclotron frequencies if the ratio of plasma frequency to cyclotron frequency is between 0.3 and 1, but in that case the fundamental and harmonic are expected to have opposite polarization, as has been observed in Jupiter's auroral kilometric radiation by Mellott et al. (1986). In contrast, the burst on YZ CMi tends to show the same polarization at ν and 2ν.

During the burst peak in minutes 4 to 6, the mapping between frequency and sense of polarization is, roughly: RCP for 1-1.5 GHz, LCP for 1.5-2 GHz, RCP for 2-3.2 GHz, and tentatively switching back to LCP above 3.2 GHz (this is seen more clearly in the LCP dynamic spectrum, which peaks at 1.5-2 GHz and above 3 GHz). The predicted dominant wave mode for ECM (x-mode or o-mode) depends on both the ratio of plasma frequency to cyclotron frequency (Melrose et al. 1984; Winglee 1985) and the energy distribution of the exciting electrons (Melrose et al. 1984; Zhao et al. 2016). How the x-mode or o-mode wave couples into circular polarization of escaping light depends additionally on the relative orientation of the magnetic field to the direction of propagation: a positive line-of-sight magnetic field (such as emerges radially from a northern magnetic pole) in the source region means that x-mode waves couple into RCP emission and o-mode to LCP emission. One possible explanation for the switch in polarization is variation in the ratio of plasma frequency to cyclotron frequency across the source region, although this explanation fails to explain why the sense of polarization flips more than once as frequency increases. Another possible explanation is mode coupling, which can occur when the orientation of the magnetic field along the line of sight flips direction; however this requires a complex overlying magnetic field structure to explain the multiple

polarization reversals across the frequency spectrum. Another explanation is that the RCP and LCP emission originate in two magnetically connected regions with opposite polarity, such as the two footpoints of a magnetic loop; in this scenario, the alternation between RCP and LCP with frequency is a coincidence originating from different magnetic field strengths in opposite polarity regions, but this scenario also struggles to explain the multiple polarization flips. We have identified no single scenario that provides a simple explanation for the observed polarization structure.

4.5.2 Frequency drift rate

The YZ CMi burst RCP dynamic spectrum in Figure 4.2 shows a number of features cover a wide frequency bandwidth, with no drift rate measurable with our 1-second integration time, which means we can put a lower limit on frequency drift rate. The vertical feature at t=5 minutes in Figure 4.2 extends from at least 2.4 GHz to 3.5 GHz, with no frequency drift resolved even when plotted with the full time resolution of 1 second. This implies a lower limit on frequency drift rate of $\dot{\nu} > 1.1$ GHz/sec or $\dot{\nu}/\nu > 0.37$ sec^{-1}. As discussed in Section 4.4, we are unable to uniquely identify the cause of this frequency drift: source motion, or rotational modulation of highly-beamed emission. If the vertical features in the burst are indeed attributed to source motion, the lower limits on frequency drift rate imply high source speeds.

Converting frequency drift rate to speed depends on the scale length for decay of magnetic field strength in the source region. Reiners & Basri (2007) measured a surface-averaged magnetic flux on YZ CMi of $Bf > 3.9$ kG. Morin et al. (2008) measured the large-scale magnetic field of YZ CMi with Zeeman Doppler Imaging (ZDI), finding that in both 2007 and 2008 the large-scale field was dominated by a dipole field aligned with the stellar rotation axis, which has an inclination of 60°, with negative radial magnetic field at the visible pole with peak magnetic flux of 3 kG. Reiners & Basri (2009a) find that the magnetic flux detectable in Stokes V (the large-scale field characterized by ZDI) is ≤14% of the magnetic flux detected in Stokes I, which implies that the majority of the stellar magnetic flux is in small-scale fields whose magnetic field strength drops off much more rapidly than the dipole field. For emission at the fundamental cyclotron frequency, 2.4 to 3.5 GHz corresponds to magnetic field strengths of 0.86-1.25 kG. If we assume that the emission region is in an area where magnetic field strength is dominated by a 3-kG stellar dipole field (which will give us a high magnetic scale length compared to smaller scale features), these frequencies correspond to heights above the

stellar surface of $1.34R_\star$ (3.5 GHz) and $1.52R_\star$ (2.4 GHz). For a stellar radius of $0.3R_\odot$, this gives an estimated source speed of 38000 km/s or ~0.1c. This estimate is limited by our inability to resolve the frequency drift with 1-second integrations (which means the source speed may be higher) and that the emission may come from small-scale magnetic features instead of a global dipole field (which means the source speed may be lower).

4.6 Statistics of Coherent Radio Bursts

4.6.1 Burst luminosity distribution vs. emission frequency

For the population of stars observed by this survey, the rate of luminous bursts peaked in the lower half of L band. Figure 4.3 shows all the survey data in time series of $S_{1\mathrm{pc}}$, the Stokes I flux scaled to a distance of 1 pc. The data are divided into sub-bands with $\nu_{\max}/\nu_{\min} = \sqrt{2}$ before averaging over frequency to produce the time series. The frequency channels were weighted by their inverse variance when averaging, where the inverse variance was measured from the imaginary component of the dynamic spectrum; this downweighted RFI to maximize sensitivity of the resulting time series. The time series for the imaginary component of the baseline-averaged visibilities are shown on the plot, offset by -0.5 Jy. The lower half of L band shows the most frequent, most luminous bursts.

The thick lines in the left panel of Figure 4.4 shows the fraction of time the stars spend above a given value of $S_{1\mathrm{pc}}$ in each subband. As a control, the thin lines show the same quantity calculated using the imaginary component of the time series, providing an estimate of the false alarm rate, i.e. how much the solid lines are overestimating burst rates due to variations in the time series caused by noise, RFI, or background sources.

We restrict the calculation in Figure 4.4 to a minimum 1-pc flux of 100 mJy to keep the P band false alarm rate low; this restriction does cause some fainter coherent bursts to be neglected, especially in S band. $S_{1\mathrm{pc}} = 100$ mJy corresponds to a luminosity of 1.2×10^{14} erg/s/Hz. The right panel of Figure 4.4 translates the fractional time spent bursting into lower limits on transient rates: how many bursts per area on the sky can be expected in a single snapshot observation, assuming that the density of stellar systems like our sample (single or wide-binary mid-M dwarfs with strong magnetic activity) is constant with distance and is equal to:

$$n_\star = \frac{\text{number of star systems in our sample}}{\text{volume of our sample}} = \frac{5}{(4/3)\pi(6.2\text{ pc})^3} = 0.005\text{ pc}^{-3}. \tag{4.3}$$

This is a conservative estimate of the density of such systems because we do not count the handful of other nearby highly active flare star systems that we have not observed. In addition, this estimate of burst rates does not account for the contribution of less active stars, which may produce luminous coherent radio bursts as well. However, we note that our estimation of burst rate may be skewed by the fact that most of our survey time is spent on only two stars, AD Leo and UV Cet. In addition, the approximation of constant spatial density will break down for estimating rates of very faint events, because the density of active M dwarfs declines as you move away from the galactic plane; in addition to decreasing overall stellar density, the fraction of M4 dwarfs with magnetic activity declines by about a factor of 2 at 100 pc compared to the Galactic plane (West et al. 2008). Since our brightest events have $S_{1\mathrm{pc}} \sim 1$ Jy, if the density of active mid M dwarfs declines at a height of roughly 100 pc, using constant density to estimate transient rates should work for fluxes ≥ 0.1 mJy. We consider the predicted transient rates in the right panel of Figure 4.4 to be lower limits, because of our conservative estimates of the source density and because we imposed a lower cutoff on burst luminosity of 1.2×10^{14} erg/s/Hz, neglecting fainter events.

Figure 4.4 demonstrates that luminous bursts are more abundant in the lower half of L band (1-1.4 GHz) compared to lower and higher frequencies. This stands in contrast to the Sun, on which luminous bursts are an order of magnitude more frequent below 1 GHz than in bands above 1 GHz (Nita et al. 2002). The abundance of >1 GHz coherent radio bursts compared to the Sun can be attributed to the stronger magnetic field strengths and higher plasma densities in the atmospheres of active M dwarfs, which push the cyclotron frequency and plasma frequency to higher values, as well as to the reduced free-free absorption at high frequencies due to the higher coronal temperatures on active stars. The decline of burst occurrence rate below 1 GHz observed on these stars indicates that the population of bursts observed by this survey are dominated by disturbances that are restricted to the low corona, where magnetic field strengths are >300 kG and/or plasma densities are $> 3 \times 10^{10}$ cm^{-3}. Many of these bursts are likely due to the electron cyclotron maser, due to the constraints of free-free absoprtion on plasma emission above ~1.5 GHz, and without simultaneous optical or X-ray data, it is unclear whether the bursts are powered by stochastic energy release in flares or continual auroral currents. The presence of this population of ultra-luminous bursts peaking at 1-1.4 GHz may be connected to the strong large-scale magnetic fields that have been observed on these stars, which can generate powerful currents due to interaction of the stars' large-scale magnetic

fields with ambient plasma that has been ejected from the star or from a close-in planet, analogous to Jupiter's magnetic field interacting with plasma erupted from its volcanic satellite Io to drive auroral currents.

4.6.2 Expected burst rates for transient surveys

Figure 4.5 shows predicted densities of stellar coherent radio bursts for the frequency bands of three ongoing and upcoming transient surveys: the ASKAP VAST survey (1.13-1.43 GHz; Murphy et al. 2013), the MeerKAT ThunderKAT survey (the band which overlaps with our survey is 1-1.75 GHz), and the VLA Sky Survey (VLASS, covering all of VLA S band, 2-4 GHz). We generated these predictions following the same procedure described in the previous section, except using a shorter integration time of 150 sec and using a lower S_{1pc} minimum value of 3 times the median time series RMS for each band. We were able to use shorter integration times and lower flux thresholds since these surveys draw only from L and S bands, which are more sensitive than P band; however we compared results with different minimum values for S_{1pc} and integration times and found that it had only a small effect on the outcome, since luminous long-duration bursts dominate the predicted transient densities.

The L band surveys, VAST and ThunderKAT, will detect a higher rate of luminous stellar coherent radio bursts than the S band survey, VLASS. VAST sees a moderate enhancement in luminous events compared to ThunderKAT due to VAST's narrower band, since averaging over a wide band decreases the measured flux of the narrowband continuum of coherent stellar bursts.

4.6.3 Sense of circular polarization

Spectropolarimetric observations by Morin et al. (2008) measured the polarity of mid M dwarfs' magnetic dipole fields in 2007-2008. For AD Leo, YZ CMi, and EV Lac, the visible magnetic pole was a southern magnetic pole, and for EQ Peg A and B the visible pole was a northern magnetic pole. UV Cet and BL Cet also both had their northern magnetic pole visible in 2012 (Julien Morin, private communication). For radio bursts originating from a region where the line-of-sight magnetic field direction agrees with this measured dipole orientation, x-mode would correspond to LCP for AD Leo, YZ CMi, and EV Lac, and to RCP for EQ Peg and UV Cet.

All long-duration (hour-timescale) coherent bursts at >1 GHz have an observed sense of circular polarization that consistent with the x-mode polarizations pre-

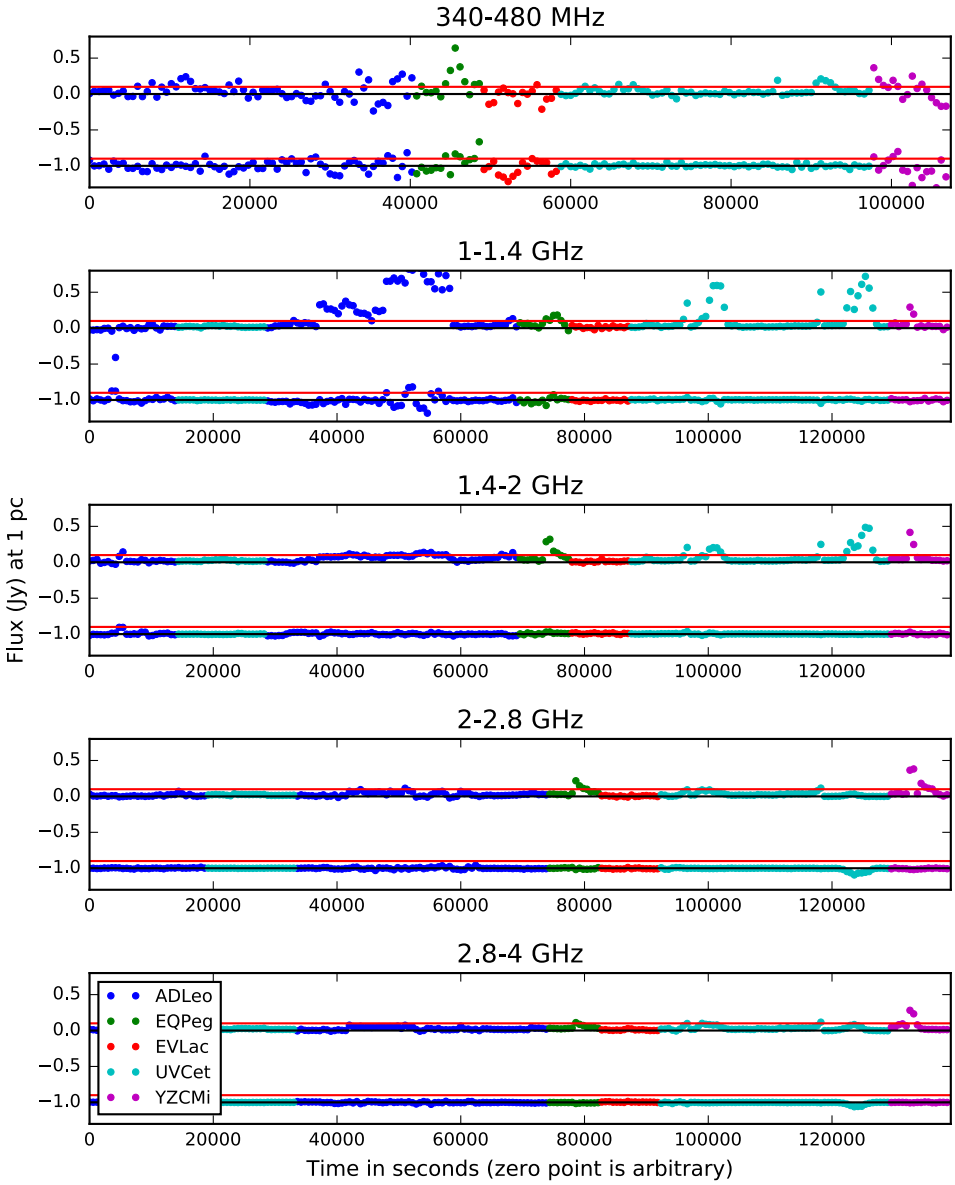

Figure 4.3 Time series of all observations, scaled to a distance of 1 pc. The Stokes I flux is averaged to 10-minute integrations and across the frequency bands, which were chosen to all have the same fractional bandwidth of $\nu_{\max}/\nu_{min} \approx \sqrt{2}$: 0.34-0.48, 1-1.4, 1.4-2, 2-2.8, and 2.8-4 GHz. The lower half of P band, 0.24-0.34 GHz, was excluded due to high noise levels. The observations are concatenated, removing times without data, so the x-axis shows the total time on source of our survey. The data are colorized by source, with multiple observations of a source in a given year shown as a continuous block. The time series is the real component of the baseline-averaged visibilities; shown offset by -0.5 Jy is the imaginary component of the same quantity, which is used to estimate the RMS on the time series, calculating one RMS per observing block. The red horizontal line shows $S_{1\mathrm{pc}}$ =100 mJy, which is used as the minimum threshold flux for calculating expected transient rates due to stellar coherent radio bursts.

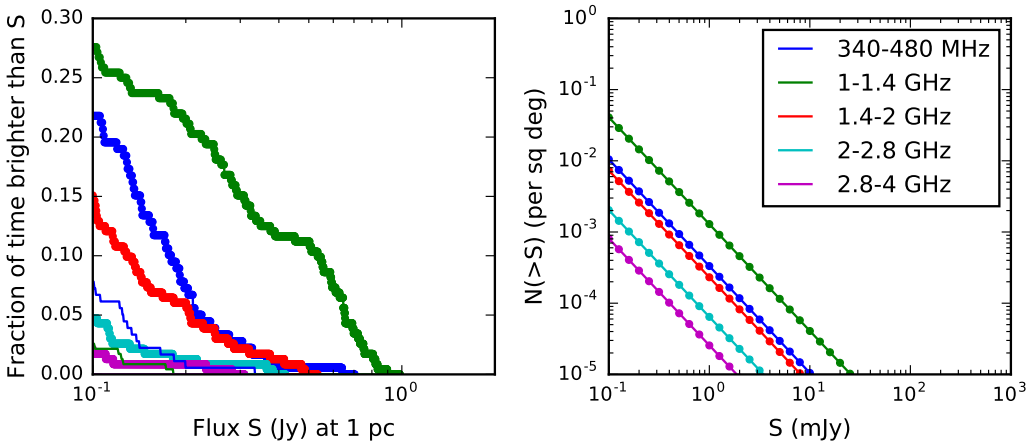

Figure 4.4 Rate of stellar coherent radio bursts versus frequency. (left) Fraction of time that a given highly active M dwarf, viewed from 1 pc, will spend bursting brighter than a given flux in the listed bands. The thin lines at the bottom show the false alarm rate. (right) The expected rate of transients per area due to stellar coherent radio bursts, analogous to Figure 22 in Mooley et al. (2016), which summarizes galactic radio transient populations. We assume a constant source density as a function of distance, so the predicted transient rates follow a Euclidean relationship of $N(>S) \propto S^{-3/2}$.

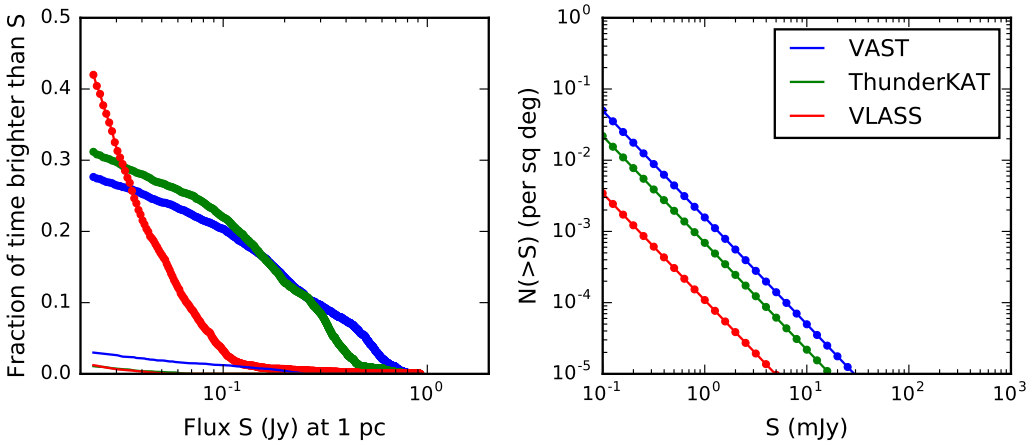

Figure 4.5 Predicted rate of stellar coherent radio bursts in transient surveys. Both panels are in the style of Figure 4.4, with the exception that burst rates are calculated down to a minimum $S_{1\mathrm{pc}}$ of 3 times the minimum RMS in the time series, and the time series were calculated with a shorter integration time of 150 sec.

dicted based on spectropolarimetry measurement of the large-scale field. 2 of 2 epochs on YZ CMi show long-duration coherent emission with left circular polarization; the shorter-duration (minutes-timescale) event on YZ CMi has both left and right circular polarization. 1 of 2 epochs on EQ Peg has long-duration coherent emission, which is righthand circularly polarized. EV Lac has no events. 7 of 8 epochs on UV Cet have strong right circularly polarized features, most of which are long duration; and no long-duration left polarized events are detected. The 3 epochs on AD Leo with confident detections of coherent radio emission all have long-duration left circularly polarized emission occurring above 1 GHz, although a minutes-long event and long-duration emission below 1 GHz are right circularly polarized; possible reasons for the polarity inversion at low frequencies on AD Leo are discussed in Paper III. In addition, Kellett et al. (2002) collate the properties of radio bursts on UV Ceti and YZ CMi across more than 10 years of published observations, finding that the preponderance of events from UV Ceti and BL Ceti have right circular polarization and from YZ CMi have left circular polarization.

If this is a real pattern, and not just confirmation bias, it suggests that long-duration coherent bursts above 1 GHz originate near the stellar magnetic pole in features that share the polarity of the large-scale dipole field, and that these stars have not reversed their magnetic polarity between the spectropolarimetric observations in 2007-2012 and the radio observations in 2013-2015, and perhaps not over the course of the decades implied by including Kellett et al. (2002)'s compilation of events. In addition, it would imply that long-duration coherent emission above 1 GHz is in the x-mode, favoring the electron cyclotron maser as the emission mechanism. The population of coherent radio bursts on active M dwarfs observed by this survey, whose luminosity distribution peaks at 1-2 GHz, may therefore originate from ECM emission powered by energetic electrons in the stars' large-scale magnetic field, a phenomenon which does not occur on the Sun.

4.7 Conclusions

We have conducted a 58-hour, 23-epoch survey of 5 nearby active M dwarfs with the VLA, motivated by the possibility that the extreme optical flares of these stars are accompanied by energetic CMEs with radio-loud shock fronts. This survey includes observations from 2013 with continuous coverage of 1-6 GHz, and from 2015 with coverage of 0.22-0.48 and 1-4 GHz. This wide bandwidth, enabled by the upgrades to the VLA, greatly extends the maximum fractional bandwidth of stellar dynamic spectroscopy, opening the possibility of tracking coronal sources

across regions varying by more than an order of magnitude in density or magnetic field strength.

We detect no events that clearly resemble the "Type II" solar radio bursts that originate at CME shock fronts. However, we find that active M dwarfs produce luminous coherent bursts in all bands observed, with coherent bursts detected in 13 of the 23 epochs. An exceptional event on YZ CMi has substructure that may imply source motion at speeds of ~0.1c. This burst shows repeated alternations in the sense of circular polarization across the frequency spectrum, for which we find no single compelling explanation.

The rate of luminous bursts peaks in the lower portion of L band (1-1.4 GHz) and declines at both lower and higher frequencies. This stands in contrast to the Sun, where luminous radio bursts become more common at frequencies below 1 GHz. The decline of the burst luminosity and rate at lower frequencies indicates that the majority of bursts observed by this survey belong to a population that is confined to the low corona, where GHz frequencies originate, rather than with eruptive events that escape the stellar corona. We favor the electron cyclotron maser as the emission mechanism for most events due to the high frequencies reached by the bursts and the tentative association of the >1 GHz emission with the polarization of x-mode expected based on the large-scale stellar magnetic field.

We use our data to produce time series and predict transient densities for the frequency bands of upcoming or ongoing transient surveys, ASKAP VAST, MeerKAT ThunderKAT, and the VLA Sky Survey, finding that VAST's 1.13-1.43 GHz band will find the highest rate of coherent stellar radio bursts from active M dwarfs, due to its narrower bandwidth at the frequency corresponding to the peak of the burst luminosity distribution.

4.8 Acknowledgements

This research was conducted in collaboration with Gregg Hallinan and Stephen Bourke, who will be co-authors on the upcoming publication. Tracy Clarke provided valuable advice about P band calibration.

This material is based upon work supported by the National Science Foundation under Grant No. AST-1311098.

The National Radio Astronomy Observatory is a facility of the National Science Foundation operated under cooperative agreement by Associated Universities, Inc.

This research has made use of the SIMBAD database, operated at CDS, Strasbourg, France.

J.R.V. thanks the Troesh family and the PEO International Scholar Award program for financial support of her graduate research.

4.A Dynamic Spectra of All Observations

Figures 4.6a-4.6g show the dynamic spectra of all L, S, and C band data from this survey and Figures 4.7a-4.7e show all P band dynamic spectra. Detected stellar coherent radio bursts appear as continuous patches of high signal-to-noise pixels (bright blue or bright red) in Stokes I or V (columns 1 and 3), with no strong features in the imaginary component of the spectrum (columns 2 and 4).

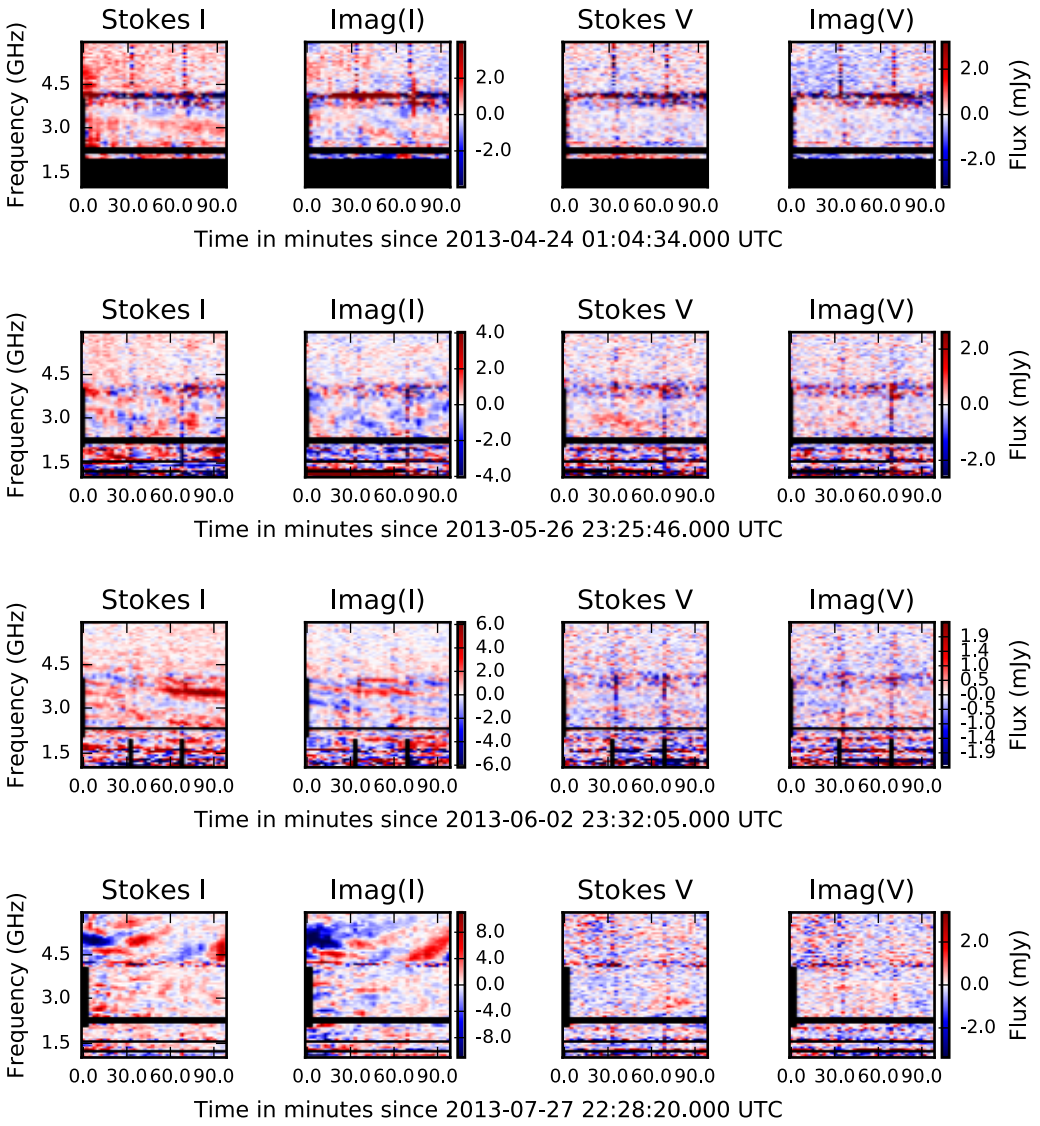

Figure 4.6a 1-6 GHz dynamic spectra for all 2013 observations of AD Leo (listed in Table 4.1). The dynamic spectra are binned to a resolution of 150 seconds and 64 MHz. The columns labeled "Stokes I" and "Stokes V" are our measurements of the source flux, whereas the columns labeled "Imag(I)" and "Imag(V)" are the imaginary component of the baseline-averaged visibilities. The star should not contribute to the imaginary component so these columns show the contribution of background sources and RFI to the dynamic spectrum. The color scale saturates at 6 times the median RMS per channel in the imaginary component of the dynamic spectrum. The Stokes V dynamic spectra have lower RMS due to the lack of circularly-polarized background sources. These four observations contain no unequivocal burst detections but there are two faint candidates in Stokes V only, one each in the second and fourth epochs.

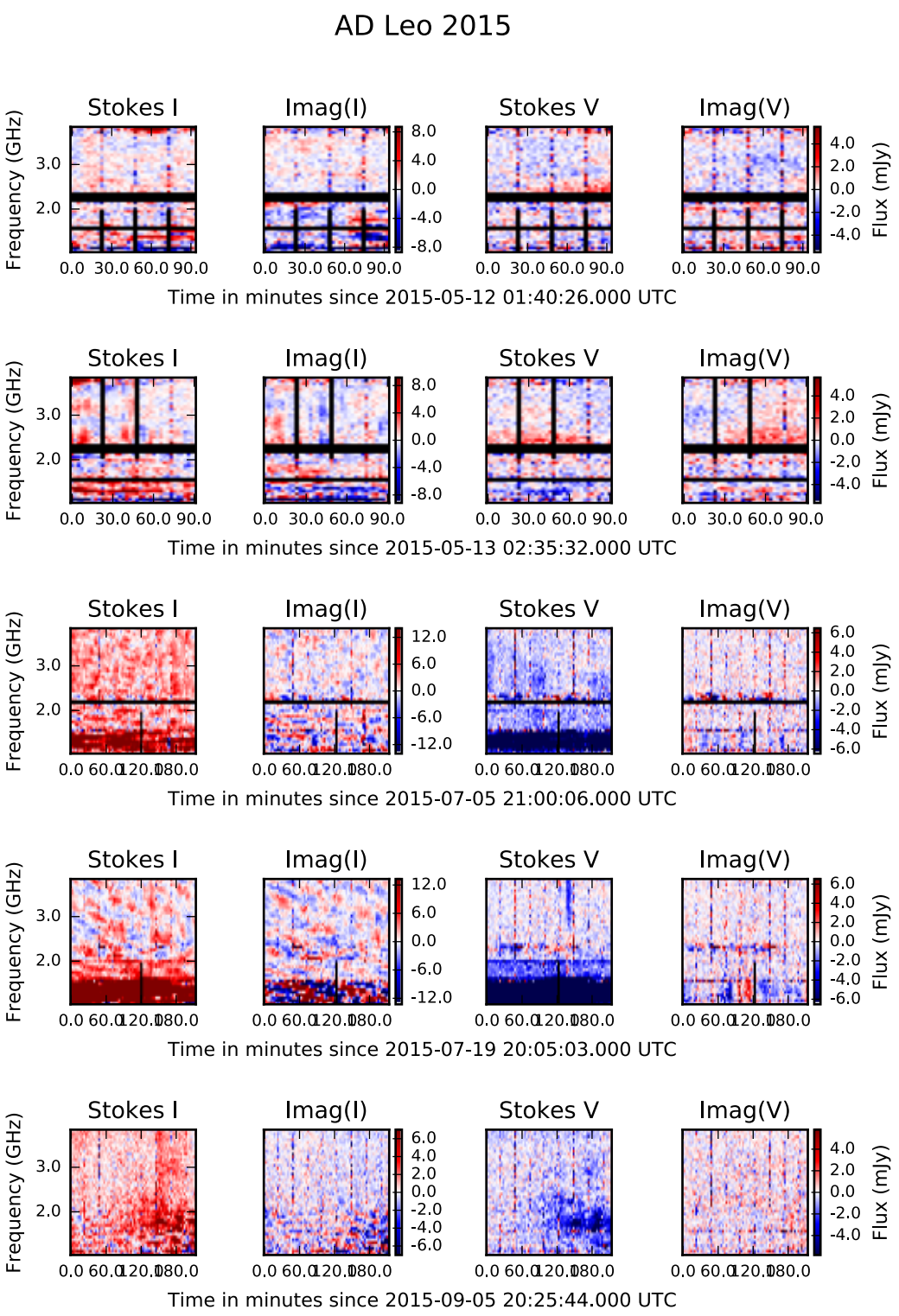

Figure 4.6b 1-4 GHz dynamic spectra for all 2015 observations of AD Leo, in the style of Figure 4.6a. Note that the first two epochs are 2-hour blocks whereas the following three are 4-hour blocks. Bright coherent bursts were detected in epochs 3 to 5 in Stokes I and V. These epochs, which have accompanying VLBA observations, are discussed in greater detail in Paper III.

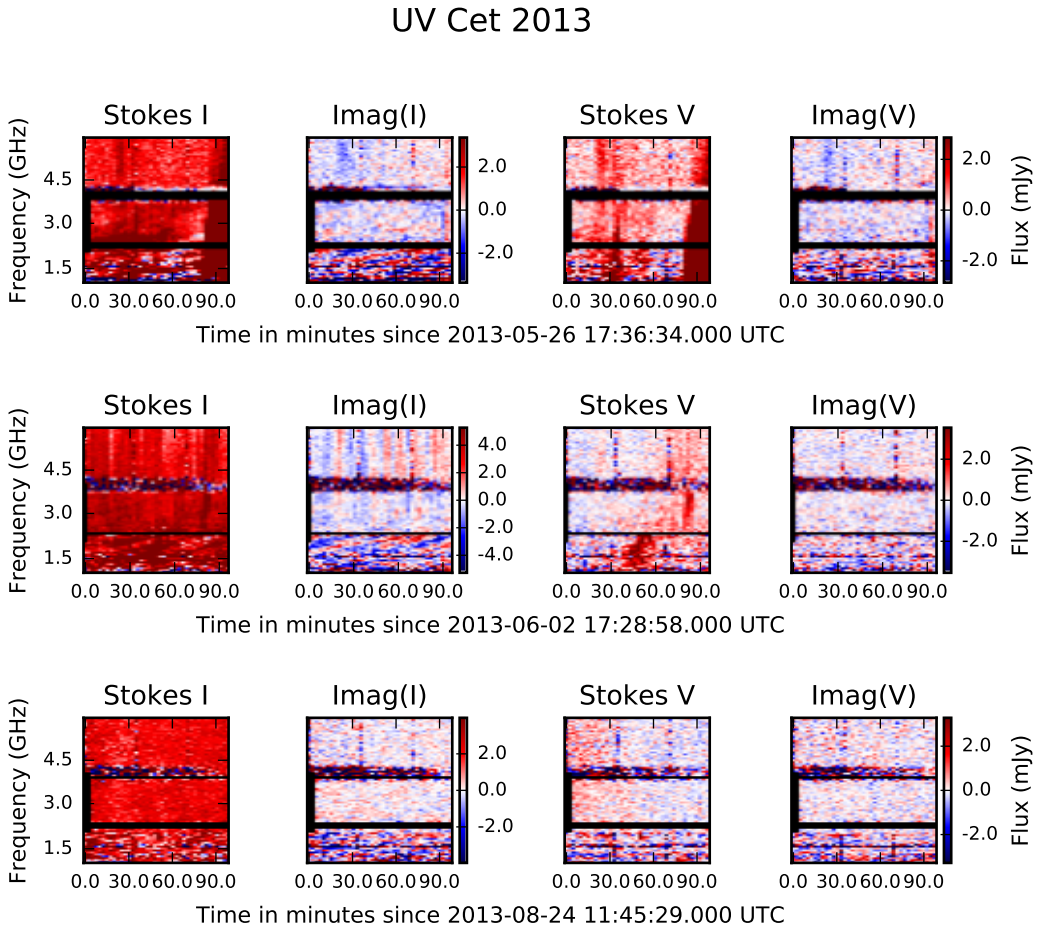

Figure 4.6c 1-6 GHz dynamic spectra for all 2013 observations of UV Cet, in the style of Figure 4.6a. The first two epochs both show substructure attributed to coherent emission, discussed in Paper II.

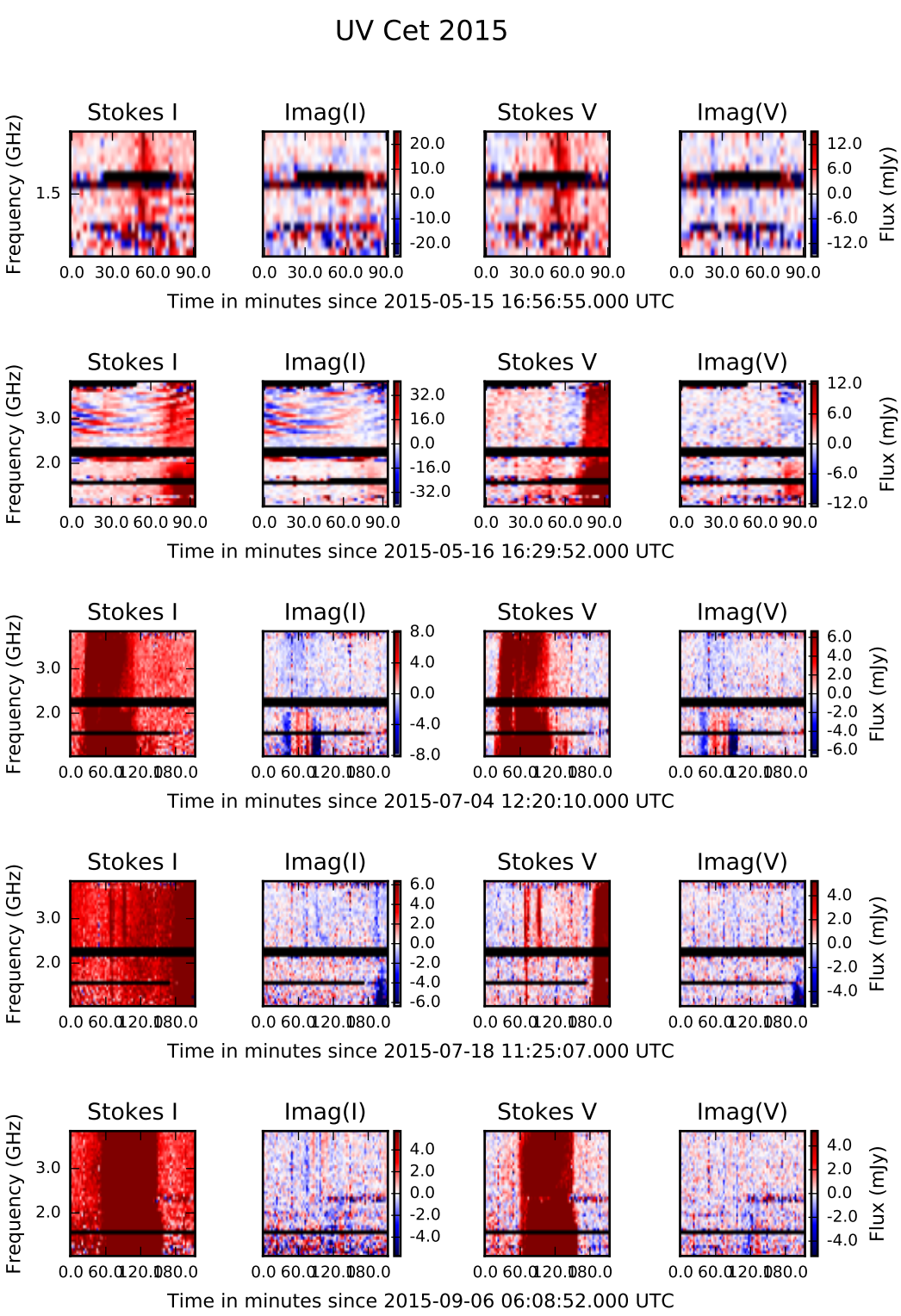

Figure 4.6d 1-4 GHz dynamic spectra for all 2015 observations of UV Cet, in the style of Figure 4.6a. Note that the first two epochs are 2-hour blocks whereas the following three are 4-hour blocks. All epochs show strong righthand circularly polarized emission, discussed in Paper II.

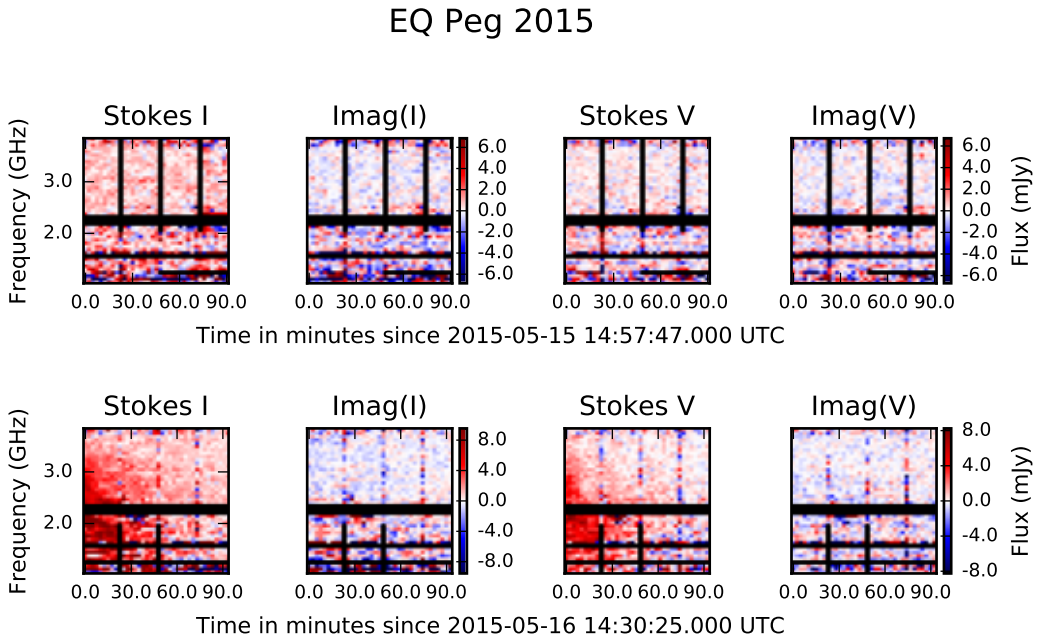

Figure 4.6e 1-4 GHz dynamic spectra for both observations of EQ Peg, in the style of Figure 4.6a. The second epoch contains a strongly righthand polarized burst.

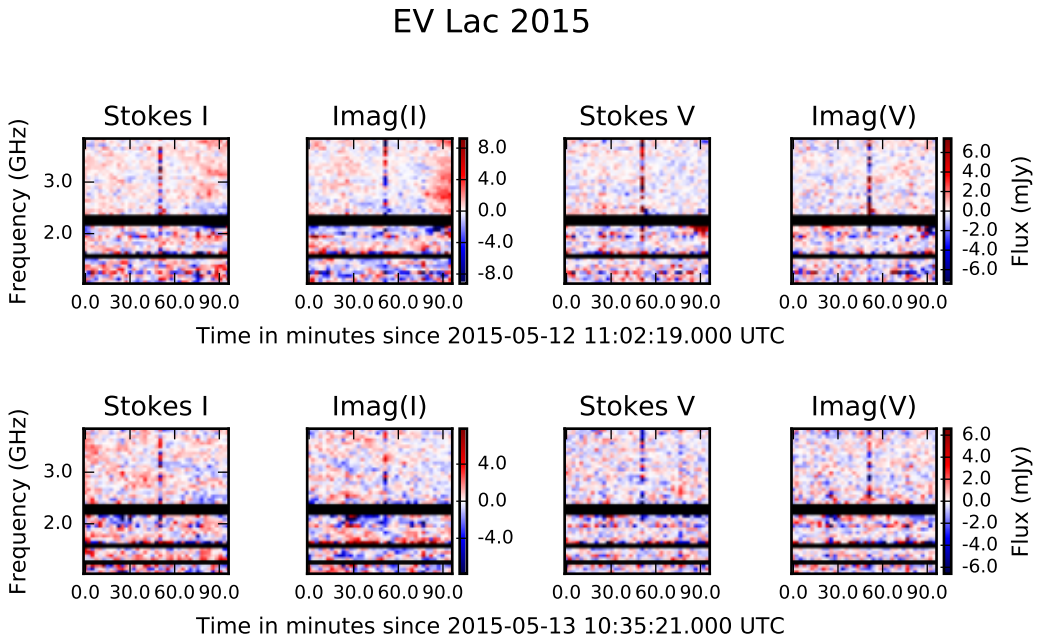

Figure 4.6f 1-4 GHz dynamic spectra for both observations of EV Lac, in the style of Figure 4.6a. No radio bursts were detected.

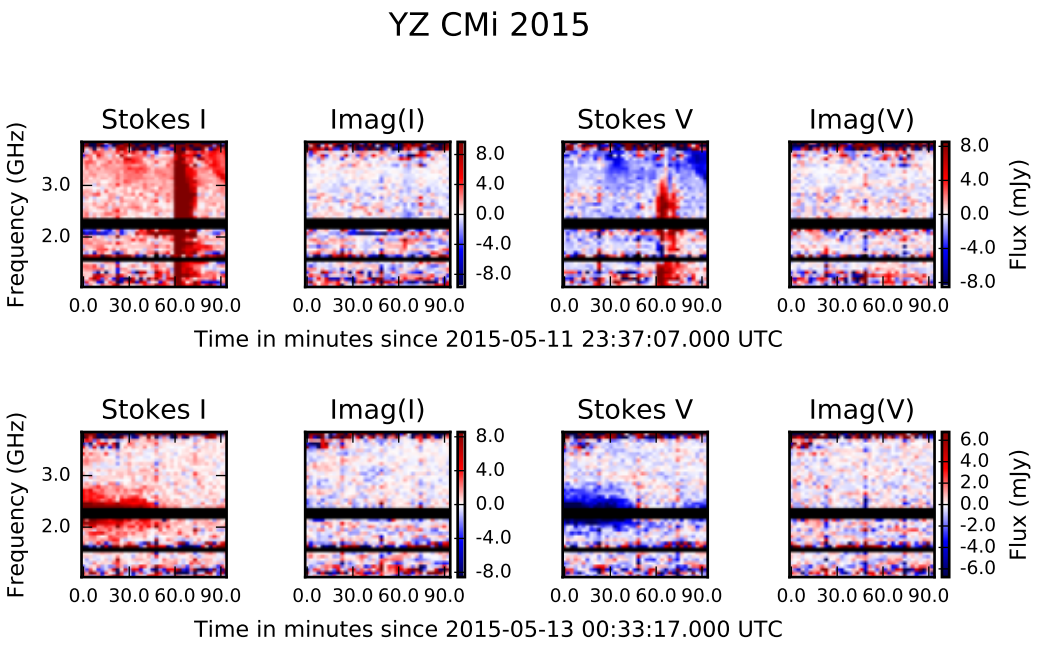

Figure 4.6g 1-4 GHz dynamic spectra for both observations of YZ CMi, in the style of Figure 4.6a. Both epochs contain bursts with strong circular polarization.

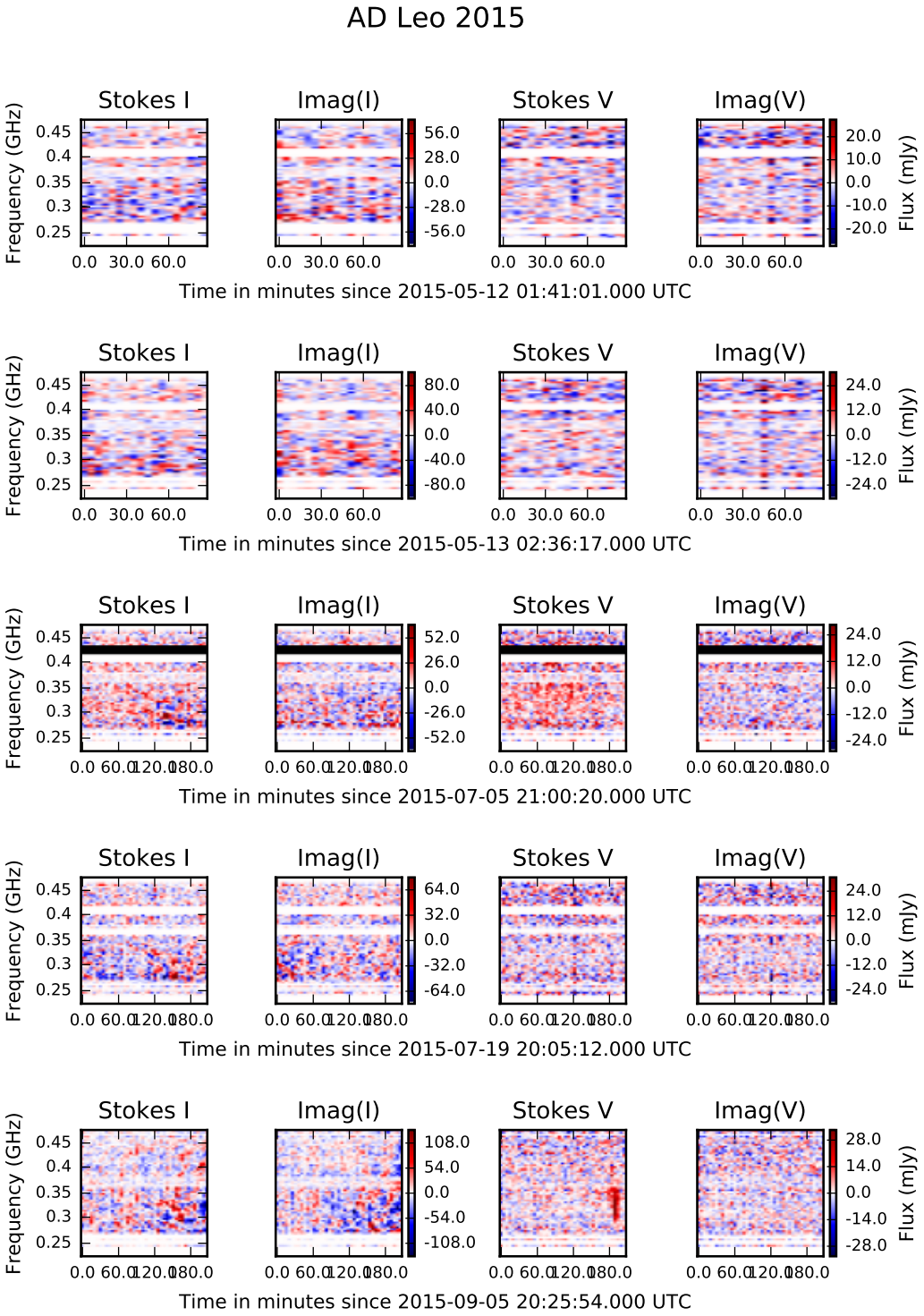

Figure 4.7a 224-482 MHz dynamic spectra for all observations of AD Leo. These plots are in the style of Figure 4.6a but binned to 300 sec and 4 MHz and the color scale saturates at 6 times the median channel RMS of the imaginary component of the spectrum. Background source residuals contribute strongly to the Stokes I dynamic spectra. Right circularly polarized events are detected in epochs 3 and 5.

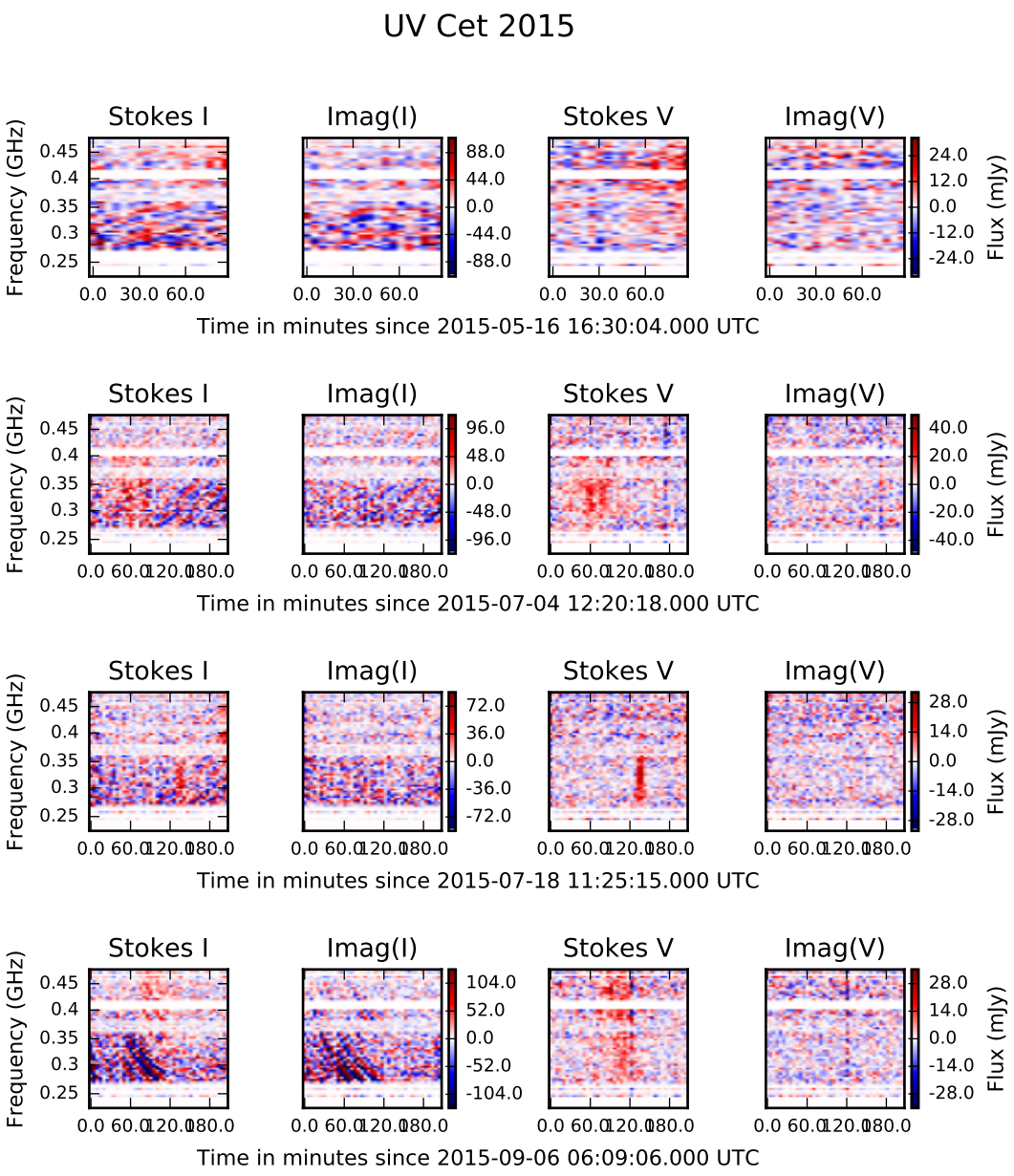

Figure 4.7b 224-482 MHz dynamic spectra for all observations of UV Cet, in the style of Figure 4.7a. Right circularly polarized events are detected in all epochs.

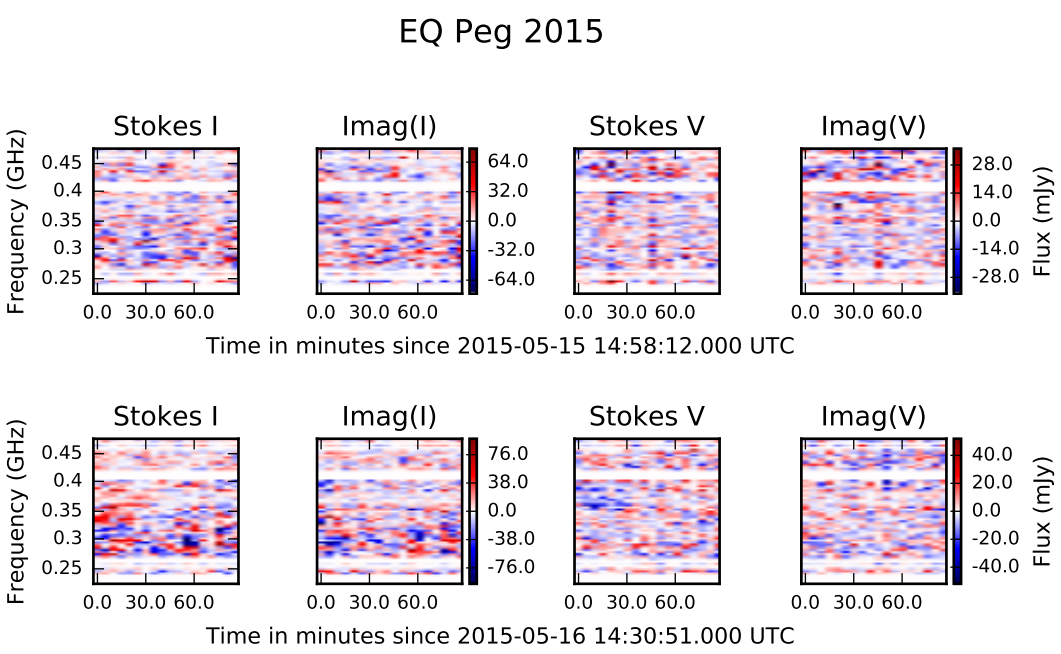

Figure 4.7c 224-482 MHz dynamic spectra for both observations of EQ Peg, in the style of Figure 4.7a. No radio bursts were detected in P band although the first epoch had a burst at higher frequencies.

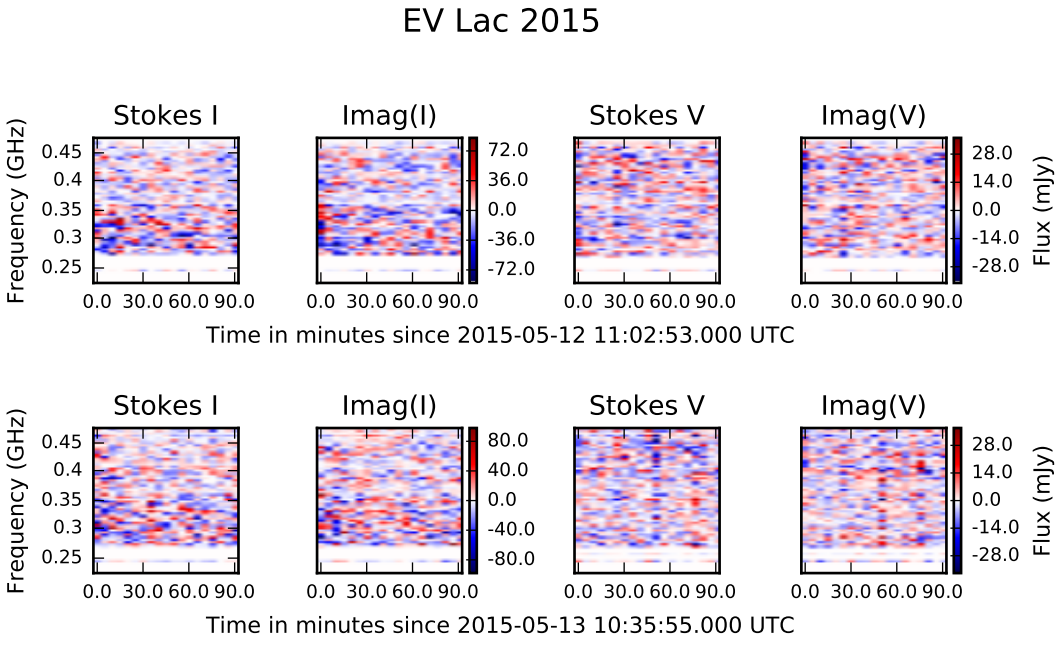

Figure 4.7d 224-482 MHz dynamic spectra for both observations of EV Lac, in the style of Figure 4.7a. No radio bursts were detected in P band or at higher frequencies.

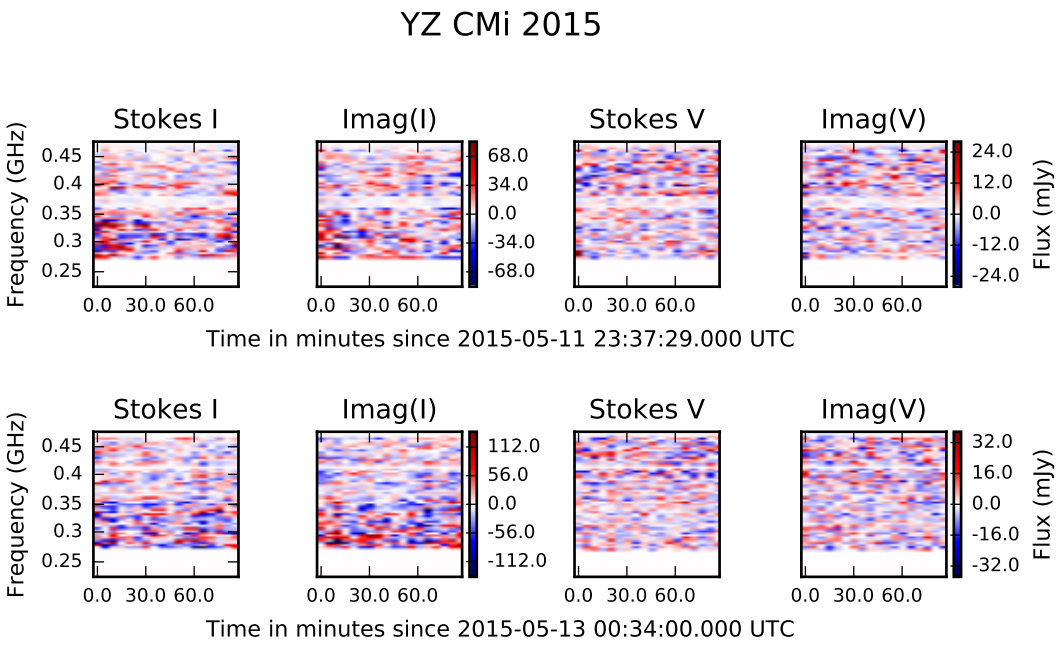

Figure 4.7e 224-482 MHz dynamic spectra for both observations of YZ CMi, in the style of Figure 4.7a. No radio bursts were detected in P band although there were events in both epochs at higher frequencies.

Chapter 5

ULTRA-WIDEBAND OBSERVATIONS OF UV CETI'S RADIO AURORA

Abstract

UV Ceti, an M6 dwarf, is an archetypal flare star, famous for its frequent energetic flares across the electromagnetic spectrum, including bright strongly-polarized radio bursts. Here we present wide-bandwidth spectroscopy and high-resolution imaging of a series of luminous long-duration radio bursts on UV Cet, observed with the VLA and VLBA at 0.22-8.5 GHz in 2013 and 2015. The coherent emission, which we attribute to the electron cyclotron maser, is detected at all observed frequencies, implying magnetic field strengths in the source region of from 0.08 to 3.0 kG. The bursts have strong right circular polarization at all frequencies and in all epochs, which indicates that the polarity of the longitudinal magnetic field in the source region is constant across the whole source region and across epochs. 8.2-8.5 GHz VLBA observations identify the coherent bursts with UV Cet rather than its wide binary companion BL Cet. The bursts have complex morphology in the time-frequency plane, with remarkably consistent structure across the 4 months of observations in 2015. This consistency suggests that the bursts are periodic auroral emission, as seen on planets and brown dwarfs; this hypothesis will be tested by ongoing observations with the Deep Space Network. We integrate over our broad observing bandwidth to estimate the star's auroral radio luminosity to be 4×10^{22} erg/s erg/s. This makes UV Cet, an archetypal flare star, also an exceptionally luminous auroral emitter.

5.1 Introduction

UV Ceti, an M6 dwarf at 2.7 pc, was one of the first known flare stars, identified by its multi-magnitude increases in brightness during optical flares. It became the namesake for "UV Ceti type variable stars", the designation for flare stars that are not in a close binary. This class of stars also includes M5.5 dwarf BL Ceti, UV Ceti's binary companion, which has an orbital semi-major axis of 5.5 AU (Kervella et al. 2016). These two stars, which share their approximate spectral type, age, and rapid rotational velocities (Jones et al. 2005), diverge markedly in the characteristics of their stellar magnetic activity. They have similar levels of quiescent X-ray

emission, but frequent flaring on UV Cet results in a time-averaged X-ray luminosity twice that of BL Cet (Audard et al. 2003). UV Cet's quiescent radio emission, attributed to non-thermal gyrosynchrotron radiation, is of order 1 mJy, roughly an order of magnitude brighter than that of BL Cet, whose quiescent emission is a few hundred μJy or less (Kundu et al. 1987), indicating that UV Cet is more efficient than BL Cet at generating and/or retaining a non-thermal coronal electron population. Resolved imaging of the 8.4-GHz radio corona with the Very Long Baseline Array (VLBA) found that during an hours-long incoherent gyrosynchrotron flare, UV Ceti's corona consisted of two lobes separated by four stellar diameters in a direction likely aligned with the stellar rotation axis whereas BL Ceti, which produced a circularly polarized 30 mJy radio burst, was unresolved (Benz et al. 1998). Although UV Ceti produces much stronger incoherent radio emission, coherent radio bursts are frequently detected on both BL Ceti (e.g., Gary et al. 1982) and UV Ceti (including the first stellar burst observed with dynamic spectroscopy, Bastian & Bookbinder 1987, and a burst observed in 2011 by Hallinan et al. in prep), with predominantly right circular polarization, as summarized by Kellett et al. (2002).

The Sun, stars, brown dwarfs, and planets all produce coherent radio bursts. The coherent emission mechanisms that operate in stars and substellar objects are plasma emission and electron cyclotron maser (ECM) emission, reviewed in Melrose (1991). The emission frequency is determined by the plasma density and/or magnetic field strength in the source region, which corresponds to radio wavelengths for stellar coronae and planetary atmospheres. Coherent emission mechanisms can produce observational signatures including: high brightness temperature and rapid time variability, strong circular polarization, narrowband frequency structure, and narrow angular beaming. Coherent emission requires an inverted electron velocity distribution, with an excess of high speed electrons. Coherent radio bursts on the Sun and flare stars are thought to be stochastic events, with high-speed electrons accelerated at magnetic reconnection sites in flaring regions or shock fronts of coronal mass ejections. In contrast, coherent radio bursts on brown dwarfs and planets are often periodic rather than stochastic, repeating once per rotation period; in these cases, the coherent emission is powered by an ongoing supply of high speed electrons, and the transient nature of observed radio bursts is due to rotational modulation of angularly beamed emission. Such rotationally modulated radio aurorae have been observed on brown dwarfs (e.g. Hallinan et al. 2008), Jupiter and other planets, and magnetic chemically peculiar A star CU Virginis (Trigilio et al. 2011). UV Ceti, an M6 dwarf, lies at the transition between the flaring magnetic activity of the Sun and

solar-type stars and the auroral magnetic activity observed on brown dwarfs and planets.

An important distinction that separates UV Ceti's magnetic activity from that of solar-type stars is the nature of its magnetic dynamo. UV Ceti is a fully convective star, requiring a different type of dynamo than the Sun's $\alpha - \Omega$ dynamo, which is rooted in the tachocline, the interface between the solid radiative core and the differentially rotating convective layer. Spectropolarimetric observations of fully convective mid M dwarfs indicate that, compared to partially convective stars, they have a greater fraction of their magnetic flux in the large-scale field (Reiners & Basri 2009a), in configurations that are stable on timescales of at least a year (Morin et al. 2008). These observations find that the large-scale magnetic fields of late M dwarfs fall in one of two distinct morphologies: strong (kilo-Gauss) axisymmetric dipolar fields or weak non-axisymmetric fields (Morin et al. 2010), suggesting either that the fully convective dynamo causes stars to cycle between these two morphologies, or that the dynamo is bistable, causing a star to reside in one of the two states long-term. The possibility of long-term stability in the magnetic field configuration of fully convective stars is supported by photometric variability observations of mid-M dwarf V374 Peg that suggest its spot configuration is stable over 16 years (Vida et al. 2016). Kitchatinov et al. (2014) argue that fully convective low-mass stars should have a long magnetic cycle, of order 100 years, due to their long magnetic diffusion timescale. In contrast, Route (2016) infers magnetic polarity reversals on a number of ultracool dwarfs based on changes in the sense of circular polarization of radio bursts. The sense of circular polarization of coherent radio bursts depends on the longitudinal (line of sight) magnetic field polarity in the source region, making coherent radio bursts a means of tracing magnetic field evolution.

We present a series of coherent radio bursts observed on UV Ceti in 2013 and 2015: from 2013, 1-6 GHz dynamic spectroscopy with the VLA, and from 2015, 0.224-0.482 and 1-4 GHz dynamic spectroscopy with the VLA and (for 3 of 4 epochs) simultaneous 8.3-8.5 GHz observations with the VLBA. Viewed together, these observations provide evidence of a powerful radio aurora on UV Ceti, originating in a region with constant magnetic field polarity across years but whose small-scale structure evolves on timescales of months. This paper is Paper II in a three-part series: Paper I presents statistics of 58 hours of wideband dynamic spectroscopy of 5 active M dwarfs with the VLA, including the VLA data considered in this paper; Paper III brings together VLA spectroscopy and VLBA imaging to characterize the

dynamic radio corona of flare star AD Leo.

5.2 Observations

The VLA observations discussed in this paper include observations from 2013 and 2015. The 2013 observations consist of three 2-hour blocks, each covering 1-6 GHz by using the VLA's subarray capability to observe simultaneously in L, S, and C bands. The 2015 observations consist of two 2-hour blocks and three 4-hour blocks, all covering 0.224-0.482 and 1-4 GHz by using subarrays to observe P, L, and S bands. The data calibration and production of dynamic spectra are discussed in Paper I. Most of the VLA observations did not resolve the UV Cet-BL Cet binary, with the exception of the final epoch on September 6, 2015. For that epoch, the VLA was in A configuration and we used the outer antennas in a subarray observing at 2-4 GHz in order to resolve the binary.

The three 4-hour blocks of VLA observations in 2015 have simultaneous VLBA observations. These observations used a dual polarization with 256 MHz bandwidth. Correlation was performed with the DiFX software correlator (Deller et al. 2007), using a single phase center for the UV Cet-BL Cet field of 01:39:05.041, -17:56:53.21 on July 4 and July 18, 2015 and 01:39:05.1764, -17:56:52.92 on September 6, 2015. We calibrated the VLBA data using the VLBA utilities in AIPS, following the calibration approach outlined in the AIPS Cookbook Appendix C and VLBA Memo 37 ("Flux Calibration on the VLBA"). We used 3C454.3 or DA193 for bandpass calibration (to flatten the bandpass within each spectral window) and J0132-1654 for phase referencing. The observations alternated between 2-minute scans of the target field and 1-minute scans of the phase reference source. For comparison, we also included 2 short scans on J0140-1532, which was used as a phase reference for VLBA observations of UV Cet by Benz et al. (1998). As part of calibration, we used the AIPS routine *clcor* to phase shift the UV Cet field to track source motion during each 4-hour observation. The calculated source motion due to parallax, proper motion, and orbital motion (ephemeris: Kervella et al. 2016) is, in the format $(\Delta\alpha \cos\delta, \Delta\delta)$: (0.4115, -0.0347) mas/hr on July 4, 2015; (0.3507,-0.0591) mas/hr on July 18, 2015; and (0.1614,-0.0806) mas/hr on September 6, 2015.

Our main phase reference source, J0132-1654, is resolved on a number of baselines. J0140-1532, in contrast, is only marginally resolved. The resolved nature of J0132-1654 meant that without a source model for the fringe fit, there were large offsets

in the gain phases found for adjacent scans on J0132-1654 and J0140-1532 for the Hancock and Mauna Kea antennas. After fringe fitting in AIPS without a source model, we transferred the data into CASA, where we generated a model image for J0132-1654 by first calibrating and imaging only the short baselines, then adding in slightly longer baselines and iterating to create a model with the combined uv coverage of all three epochs. We used this image to correct the gain phases and calibrate the relative amplitudes of different baselines and spectral windows by solving for complex gains for each scan on J0132-1654 and interpolating these gains to the UV Cet field. After shifting the phase center to UV Cet, we used our code *tbavg* to average over the baselines and extract time series for the VLBA data. To measure the total source flux with the time series, we used only baselines shorter than 2 Mm, since source structure and motion were unresolved on these short baselines. Due to concerns about the accuracy of the calibration, so far we have only used the VLBA data to produce time series and identify which binary component is producing radio bursts, but before publication we will use the VLBA data to measure the source size of the quiescent and bursting emission and the spatial offset between them.

5.3 Dynamic spectra and time series of radio bursts

Figures 5.1-5.5 show the Stokes V dynamic spectra of the observations in 2013 and 2015 that contained luminous, long-duration coherent radio bursts. These plots include 8.4-GHz time series for the three epochs with simultaneous VLBA observations. All of these bursts have strong right circular polarization of ∼60% in all frequency bands. The star system also produced some fainter bursts during the three epochs not shown here (two 2-hour blocks in 2013 and one 2-hour block in 2015); these dynamic spectra are shown in Paper I.

The bursts in Figures 5.1-5.5 are highly structured in the time-frequency plane. In spite of this, the 4 bursts from May to September 2015 have similar morphology, with the most intense and complex substructure below 2 GHz. The 2-4 GHz emission in each epoch consists of numerous short-duration features that all share the same positive frequency drift.

5.4 Identification of binary component responsible for radio bursts

The VLBA data and the A-configuration VLA data both enable identification of the binary component responsible for the coherent radio bursts. Only one source is detected in the VLBA data, at 01:39:05.1153408, -17:56:51.7770071 on July 4, 2015, 01:39:05.1246492 -17:56:51.7916119 on July 18, 2015, and 01:39:05.1472030 -

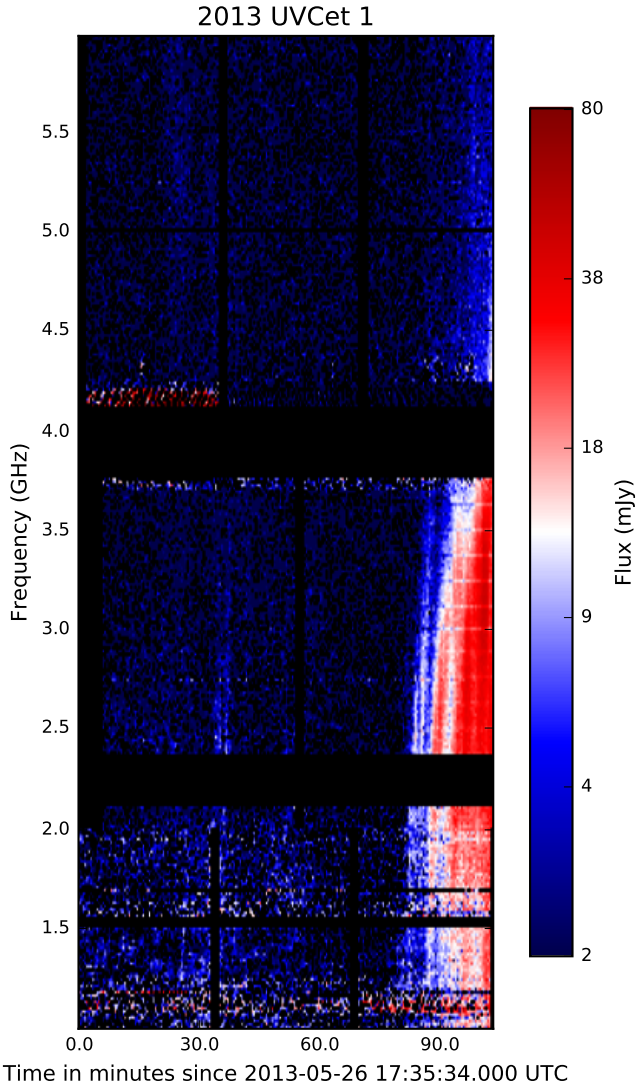

Figure 5.1 1-6 GHz Stokes V dynamic spectrum of a coherent radio burst observed from the UV Cet-BL Cet system in 2013. The spectrum is binned to a resolution of 30 seconds and 16 MHz. The color scaling and the aspect ratio are chosen to match the following dynamic spectra in this paper.

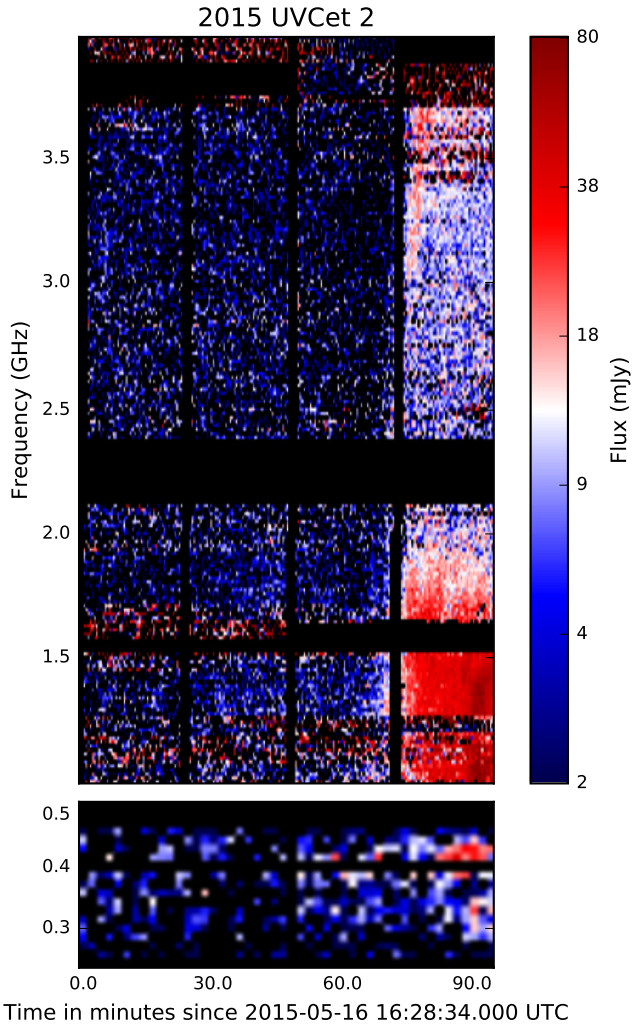

Figure 5.2 0.22-0.48 and 1-4 GHz Stokes V dynamic spectrum of a coherent radio burst observed from the UV Cet-BL Cet system in May 2015. Note that the lower frequency band is stretched to make the burst structure more visible. The spectrum is binned to a frequency resolution of 16 MHz and integrations of 30 seconds for 1-4 GHz and 120 seconds for 0.22-0.48 GHz.

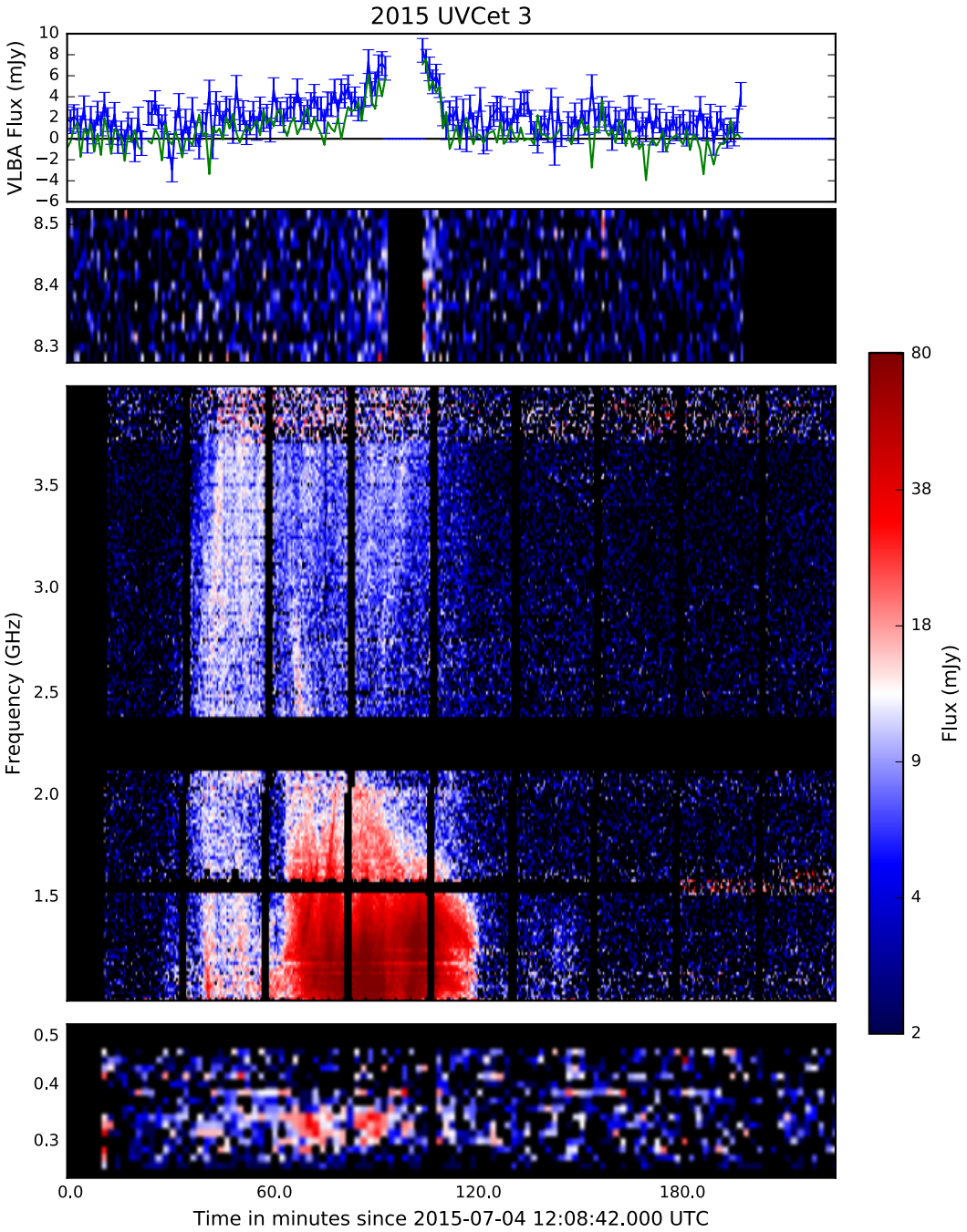

Figure 5.3 Dynamic spectrum and time series for the first VLA+VLBA epoch, in July 2015. The top panel shows the VLBA 8.3-8.5 GHz time series of the total stellar flux in Stokes I (blue) and V (green). The panel below the time series shows the Stokes V dynamic spectrum for the same VLBA data, and the bottom two panels show the 1-4 GHz and 224-482 MHz Stokes V dynamic spectra from the VLA. The plots are aligned in time. There are breaks in frequency coverage between the three dynamic spectrum plots, which have different scaling of the frequency axis and different time binning (120 sec for 0.22-0.48 GHz, 30 sec for 1-4 GHz, 60 sec for 8.3-8.5 GHz). All bands are binned to a frequency resolution of 16 MHz.

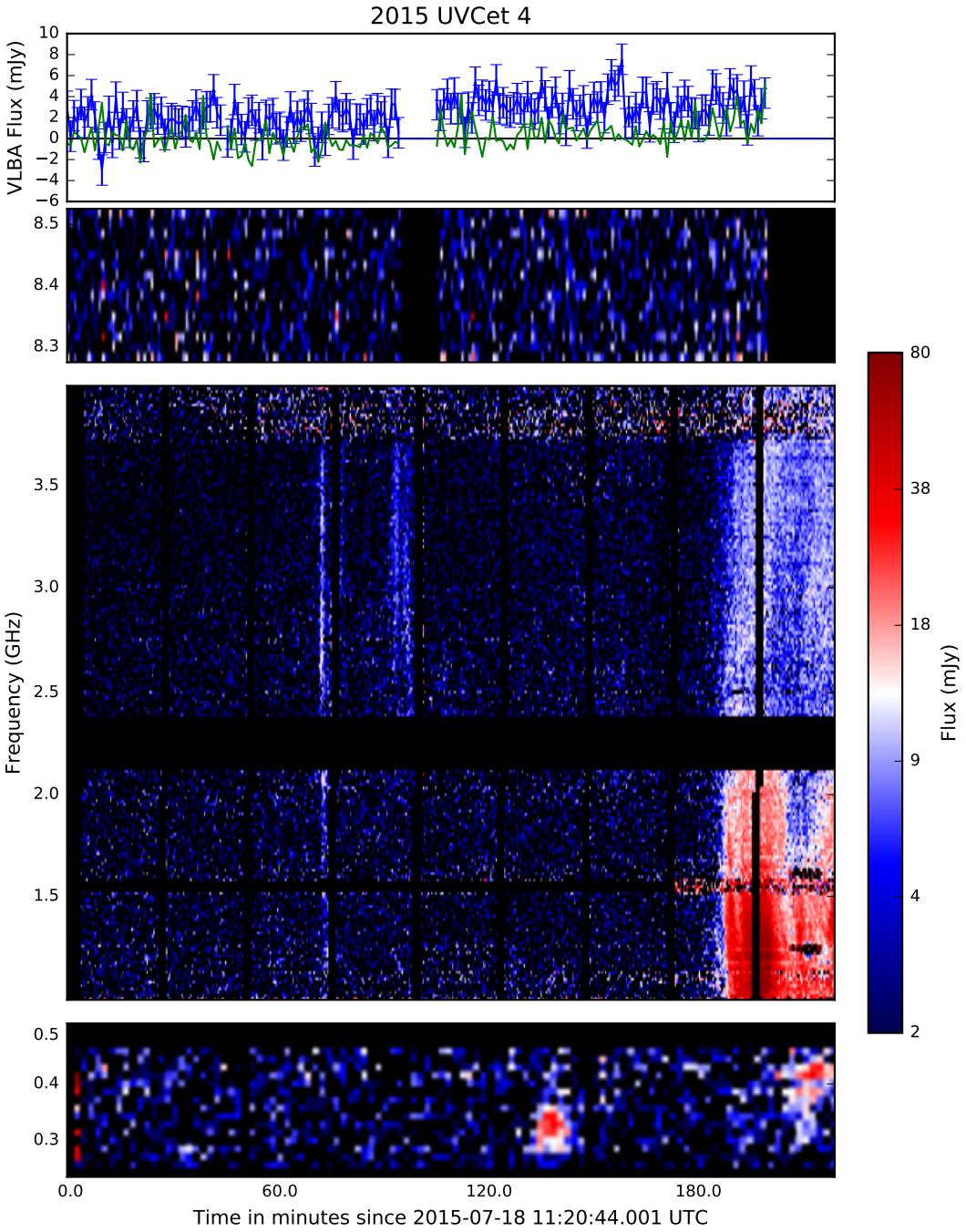

Figure 5.4 0.2-8.5 GHz Stokes V dynamic spectrum and 8.3-8.5 GHz Stokes I and V time series for the second VLA+VLBA epoch, in July 2015, in the style of Figure 5.3.

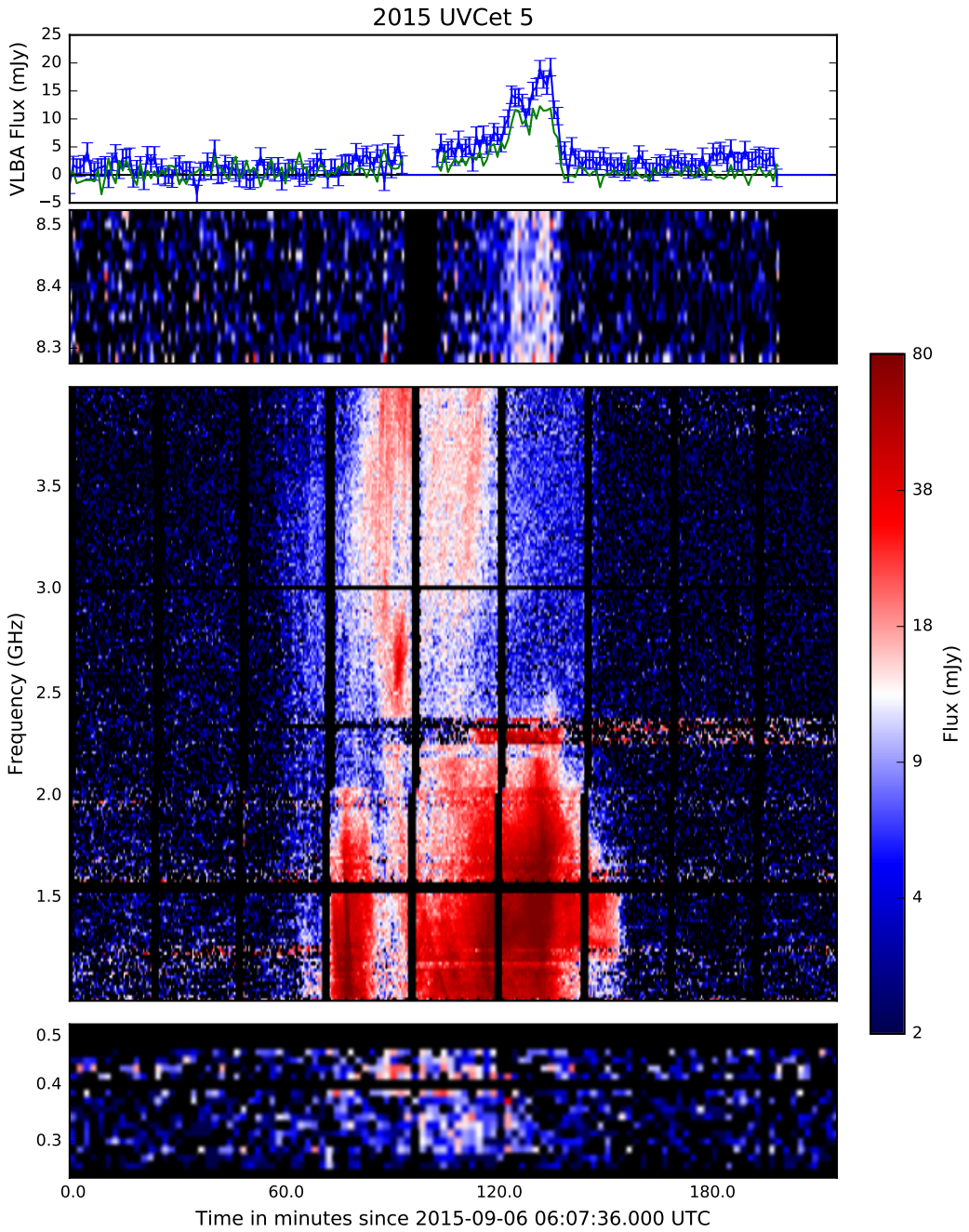

Figure 5.5 Stokes V dynamic spectrum and 8.3-8.5 GHz Stokes I and V time series for the third VLA+VLBA epoch, in September 2015, in the style of Figure 5.3.

17:56:51.8803255 on September 6, 2015. This source, which is close to the projected location for UV Cet based on the coordinates from Benz et al. (1998) and the ephemeris from Kervella et al. (2016), produces mJy level quiescent emission and coherent bursts. The September 6, 2015 VLA data, which used the outer antennas for 2-4 GHz observations, detects only one clear source, close to the predicted position of UV Cet, which is responsible for both the quiescent emission and bursting. Due to similarity of the dynamic spectrum burst morphology observed in epochs 2 through 5 in 2015, we conclude that all of these bursts originate from UV Cet. The 1-4 GHz right circularly polarized burst observed by Hallinan et al. (in prep) also is identified with UV Ceti. Based on the similar luminosity and frequency range, the burst in the first 2013 epoch may also originate from UV Cet.

5.5 Interpretation: UV Cet's radio aurora

5.5.1 Emission mechanism and magnetic field structure of source region

Plasma emission with strong circular polarization is almost certainly at the fundamental frequency rather than the second harmonic (Melrose et al. 1978). Emission at the fundamental plasma frequency is reabsorbed by free-free opacity above 1.5-2 GHz for a 10^7 K corona unless the density decreases on length scales much shorter than the thermal density scale height (see discussion in Paper I). Since UV Cet's radio bursts have strong circular polarization up to 8.5 GHz, the emission is unlikely to be plasma emission; we therefore favor the electron cyclotron maser (ECM) as the emission mechanism for these bursts. However, an opacity argument alone is not sufficient to distinguish between ECM and plasma emission, as in a high-temperature plasma, high-frequency ECM may also face an opacity problem due to gyroresonant absorption by high harmonics, as discussed in Osten & Bastian (2006).

The shared sense of circular polarization (right hand) at all frequencies implies that the emission at all frequencies is in the same mode, x mode or o mode. The emission at the range of observed frequencies is most likely all in the same harmonic, based on the lack of clear harmonic structure as well as the consistent sense of circular polarization.

If the emission is all in the same harmonic, then the ratio of strongest to weakest magnetic field strengths in the source region is $B_{\rm max}/B_{\rm min} = \nu_{\rm max}/\nu_{\rm min} = 8.5/0.22 = 39$. For first harmonic emission, this corresponds to field strengths of 0.08 to 3 kG.

Spectropolarimetric observations by Julien Morin (private communication) in 4-8 epochs per star in 2012 measured positive longitudinal field in all epochs. Assuming that the bursts come from a region with positive longitudinal field, then x-mode is RCP and o-mode is LCP, so the emission is in the x-mode. This is consistent with the prediction for ECM at the first harmonic if $\nu_p/\nu_c < 0.3$. For emission at 224 MHz, this implies plasma densities less than $7\text{x}10^7$ cm^3.

The right circular polarization of the bursts is consistent from 2011 (Hallinan et al., in prep) to 2013 to 2015. The consistent sense of polarization across epochs implies that the source region has the same polarity of longitudinal magnetic field across all epochs. This is evidence that UV Cet has not undergone any magnetic polarity reversals in the period from 2011 to 2015.

The consistent righthand circular polarization at all observed frequencies implies that the entire source region (that is visible to the observer) has the same magnetic field orientation. If the northern pole of UV Ceti's dipole field is tilted towards us, then (on the visible hemisphere) open field lines and field lines connecting the outer magnetosphere should share that magnetic field orientation: the photosphere will contain regions of negative magnetic polarity, but these should be connected to low-lying closed magnetic structures. That the emission originates only from regions with positive longitudinal magnetic polarity means that either the emission comes from a single magnetic field line or that the electrons powering the emission originate at a height above the star where the magnetic field is dominated by the stellar dipole field.

If all the emission is from a region where field strength dominated by dipole field, then $R_{\rm max}/R_{\rm min} = 39^{1/3} = 3.4$. Assuming 8.5 GHz comes from close to stellar surface, the source region spans close to the stellar surface to as far as $3.4R_\star$ from stellar center. If the supply of energetic electrons powering the emission requires closed field lines, this implies that UV Cet possesses a large closed magnetosphere compared to Sun.

5.5.2 Time evolution of auroral pulses

The mechanism for producing UV Ceti's luminous radio bursts must explain the consistent morphology of the four 2015 bursts in Figures 5.1 to 5.5. The most likely explanation for this is that these bursts are auroral pulses, repeating once per rotation period, where the structure in the time-frequency plane is due to rotational modulation of angularly beamed emission. UV Cet's v sin i (Jones et al. 2005)

implies a rotation period less than 6 hours; given the 90-minute burst duration, it is unsurprising that a burst was detected in all three of the 4-hour observations if it repeats once per rotation period.

The smoking gun for a radio aurora would be to confirm that the bursts repeat once per stellar rotation period. UV Cet has no published rotation period. If this is periodic emission, our 4-hour observations with a burst at the end (Figure 5.4), combined with the ~90 minute burst duration observed in other epochs, imply a rotation period greater than 5 hours, and v sin i limits the rotation period to less than 6. We have been allocated time to observe UV Ceti in L band with the Deep Space Network for two 7-hour blocks to search for repeated bursts. These observations will be completed on December 15, 2016.

The existing observations were not sufficient to measure periodicity, in part because of their wide separation in time, and in part because of evolution over time in the burst structure. Even among the 2015 bursts that have similar structures, the morphology is not identical, and it is distinct from the morphology of the burst in the first epoch of 2013 (Figure 5.1) and the 2011 burst in Hallinan et al. (in prep). Long-duration radio observations of UV Ceti have been conducted previously with no clear evidence of periodicity: 6.3 hours of 8.4 GHz observations in 1996 by Benz et al. (1998) and 8.4 hours of 5 GHz and 8.3 GHz observations in 2001 by Smith et al. (2005). Together, this means that while UV Cet has sustained a powerful wideband radio aurora in the past few years, its luminosity spectrum must evolve over time, and there may be times with no auroral pulses whatsoever. Possible causes of the evolving dynamic spectrum morphology and intensity of the bursts include: evolution over time in the underlying magnetic field structure or in the source of high-speed electrons. Variations in the source of auroral current might be due to changes in the longitude of active regions where flares occur, or in analogy to Jupiter, such an effect might be achieved by an undetected satellite whose orbital motion modulates the structure and timing of auroral pulses. In the case of the Jupiter-Io interaction, changes between epochs in the morphology of the burst dynamic spectrum can be modelled based on Jupiter's rotational phase and Io's orbital phase relative to the line of sight (Hess et al. 2008).

5.5.3 Radio luminosity of UV Ceti's aurora

The wide bandwidth of our observations allows us to measure a spectral energy distribution for the coherent bursts and therefore estimate the luminosity of UV

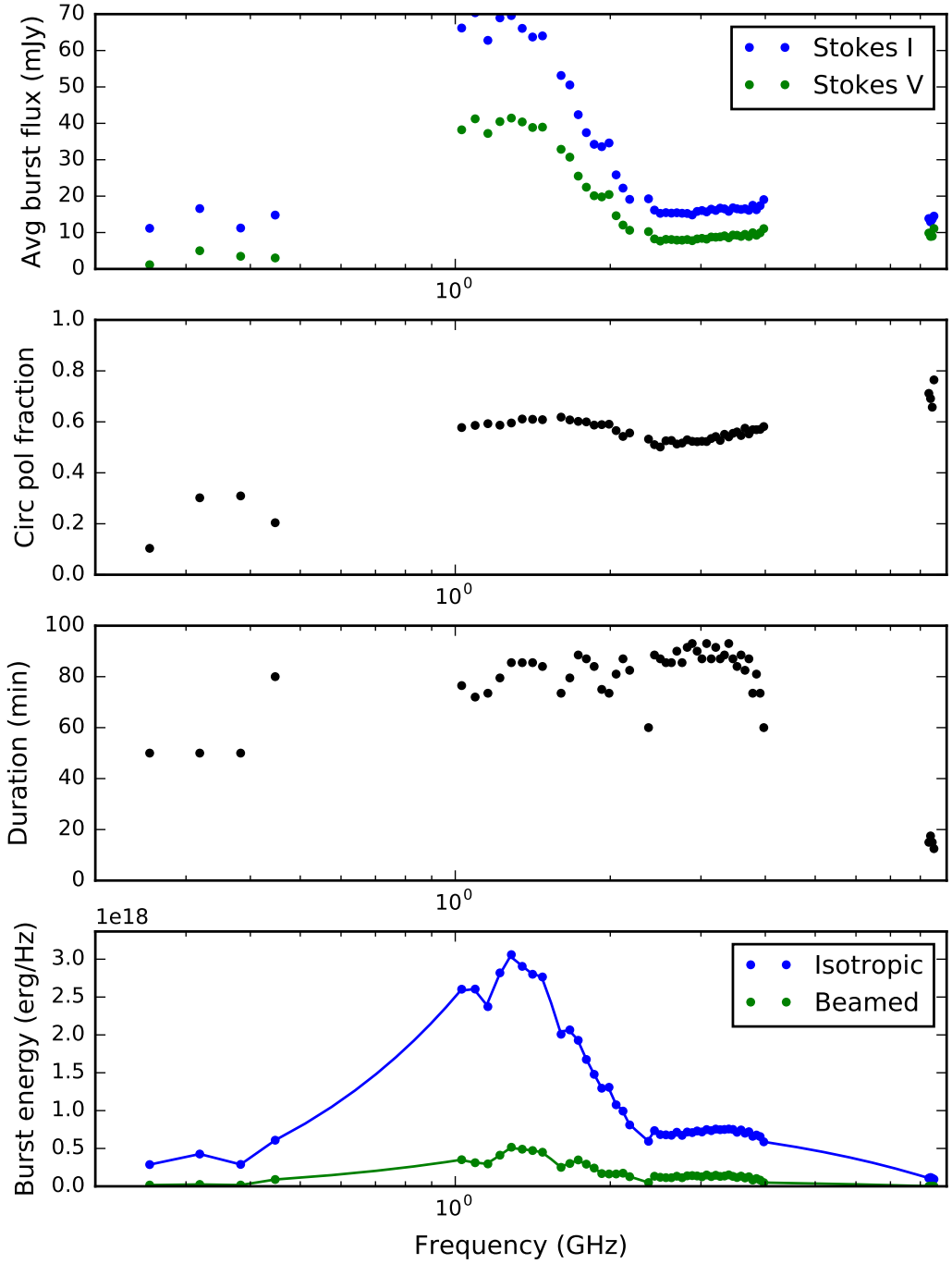

Figure 5.6 0.2-8.5 GHz spectrum of the burst on September 6, 2015. The burst properties were obtained by masking the dynamic spectrum to only include pixels where the Stokes I flux exceeds 6 mJy. (top panel) Stokes I and V flux spectra, averaged over the burst duration. (second panel) Fractional circular polarization r_c, where 1 is full right circular polarization and 0 is unpolarized. (third panel) Duration that burst is brighter than 6 mJy. (fourth panel) Burst energy spectrum assuming isotropic radiation (blue) or beamed radiation (green); see text for details.

Cet's radio aurora. We used the burst on September 6, 2015 for this calculation because our observations have complete time coverage of the burst; other events are cut off at the end or by long calibrator observations in the middle. Figure 5.6 shows the 0.2-8.5 GHz spectrum of the burst, which was calculated by masking the dynamic spectrum to restrict it to times and frequencies where the Stokes I flux exceeds 6 mJy (a few times higher than the quiescent emission). The second panel shows the fractional circular polarization spectrum, the third panel shows the duration of the burst, and the fourth panel shows the total energy radiated in the burst. We integrated across the spectrum, using linear interpolation to fill gaps in our data, to obtain a total burst energy. We calculated the total burst energy two ways: 1) assuming isotropic emission, for the case where the burst is not beamed (blue line in bottom panel), and 2) assuming that the source is beamed (green line in bottom panel). We estimated the beaming angle as θ = (burst duration / stellar rotation period), using the burst durations shown in the third panel and a stellar rotation period of 5.45 hours based on Doppler imaging of starspots reported by John Barnes in a talk at Cool Stars 19. We assumed that the beam is circular, to calculate a beaming solid angle of $\Omega = \pi(\theta/2)^2$, obtaining beaming solid angles of order 1 steradian for the 1-4 GHz burst. Integrating across the energy spectrum for beamed radiation gives a total burst energy of $8.1\text{x}10^{26}$ erg; dividing by the stellar rotation period yields a wideband auroral radio luminosity of $4.2\text{x}10^{22}$ erg/s $= 4.2\text{x}10^{15}$ W.

The time-averaged U-band flare luminosity of the UV Cet-BL Cet system is $3.26\text{x}10^{26}$ erg/s (Panagi & Andrews 1995), which is likely dominated by UV Cet. Osten & Wolk (2015) calculate that for active stars, the U-band flare energy is on average 11% of the bolometric flare energy, so we estimate UV Cet's bolometric time-averaged flare luminosity to be $3.0\text{x}10^{27}$ erg/s. If flare energy release accelerates the high-speed electrons responsible for UV Cet's auroral radio emission, this implies an efficiency of conversion of flare energy to radio auroral emission of ($4.2\text{x}10^{22}$ erg/s)/($3.0\text{x}10^{27}$ erg/s) $\sim 10^{-5}$. It is not surprising that UV Cet has high-speed electrons available to produce long-term coherent radiation: the non-thermal nature of UV Cet's quiescent radio emission may be due to the same population of electrons. The question remains as to what is the source of this high-speed electron population: Is it flaring, typically interpreted as the source of the non-thermal incoherent radio emission and thermal X-ray emission whose correlation is captured by the Güdel-Benz relation (Benz & Güdel 1994a)? Or is it a mechanism known to drive auroral currents on Solar System planets? Possible mechanisms for driving auroral currents

include breakdown of corotation between the star's magnetic field and surrounding plasma, and magnetic interaction with a close-in satellite; these possibilities are discussed in the context of brown dwarfs by Hallinan et al. (2015). Trigilio et al. (2011) put forth another possible mechanism for the aurora of magnetic A star CU Vir, magnetic reconnection of a stellar wind in a current sheet.

5.6 Conclusions

We have conducted radio observations of flare star UV Cet in 2013 and 2015, detecting a series of luminous, wideband right circularly polarized bursts. We favor electron cyclotron maser as the emission mechanism in order to explain the burst's strong polarization at high frequencies. Based on spectropolarimetric observations of a positive longitudinal field on the star, the righthand circular polarization is x-mode, consistent with ECM in a low-density environment. The consistency of the time-frequency structure of bursts observed over 4 months in 2015 provides evidence that UV Cet produces a rotationally modulated radio aurora; this hypothesis will be tested by ongoing 1.5-GHz observations with the Deep Space Network. Based on the duty cycle of emission, we measure a beaming angle of order 1 steradian, and calculate the time-averaged 0.2-8.5 GHz luminosity of UV Cet's radio aurora to be 4×10^{22} erg/s. The consistent sense of circular polarization at all frequencies suggests that the aurora is powered by a current source in the large-scale magnetic field. The consistent sense of circular polarization across all epochs indicates that the magnetic polarity of the star's large-scale field is constant for at least 4.5 years, and likely decades in the context of a history of predominantly right circularly polarized bursts from this source.

These observations add a luminous radio aurora to the list of manifestations of extreme magnetic activity displayed by UV Cet and not by its twin BL Cet. Is this a consequence of UV Cet's more vigorous flaring activity, or is it another symptom of the "hidden variable" that also causes UV Cet to flare more frequently than BL Cet and sustain a more powerful non-thermal radio corona? This hidden variable could be a dramatically different magnetic field topology, perhaps due to different states of a bistable or slowly-evolving convective dynamo, or it could be a close-in planet that interacts with the stellar magnetosphere and provides a supply of electrons into the large-scale stellar magnetic field. In the latter scenario, explored for star-planet interaction by Hess & Zarka (2011), evolution of the auroral pulses over time depends on the orbital phase of the satellite.

5.7 Acknowledgements

This work includes contributions of ideas and data from a number of collaborators who will be co-authors on the upcoming publication. I collaborated with Gregg Hallinan and Stephen Bourke on the analysis and interpretation of VLA and VLBA data. Julien Morin and Benjamin Tessore provided the longitudinal magnetic field measurements from spectropolarimetry data. Cristina Garcia-Miro, Charles Naudet, Tom Kuiper and Joe Lazio have led the Deep Space Network observations to search for a periodic radio signal. Paul Gardner is conducting optical photometric observations of UV Ceti simultaneous to the DSN observations, and Navtej Singh has provided a reduction pipeline for the optical photometry.

This material is based upon work supported by the National Science Foundation under Grant No. AST-1311098.

The National Radio Astronomy Observatory is a facility of the National Science Foundation operated under cooperative agreement by Associated Universities, Inc. This work made use of the Swinburne University of Technology software correlator, developed as part of the Australian Major National Research Facilities Programme and operated under license.

This research has made use of the SIMBAD database, operated at CDS, Strasbourg, France.

J.R.V. thanks the Troesh family and the PEO International Scholar Award program for financial support of her graduate research.

Chapter 6

COHERENT RADIO STORMS AND RESOLVED FLARES ON AD LEONIS

Abstract

Magnetically active M dwarfs release orders of magnitude more energy in flares than the Sun, with poorly understood consequences for stellar mass loss. M3 dwarf AD Leonis is a well-observed flare star that has been used as a template for modeling the effects of stellar flares on planetary atmospheres. We use radio observations to track dynamic processes in AD Leo's corona: continuum spectroscopy to detect high-speed electrons and measure the velocity of bulk plasma motion, and very long baseline imaging to resolve evolving coronal structure. The pole-on orientation of AD Leo makes it well-suited to search for stellar eruptions in the star's equatorial plane with VLBI. We present 12 hours (3 epochs of 4 hours) of simultaneous VLA and VLBA observations, using the VLA for wide-bandwidth spectroscopy covering 224-482 MHz and 1-4 GHz, and the VLBA for 8.28-8.54 GHz imaging. The first two epochs have a coherent radio "storm": 100% left circularly polarized 1.1-1.6 GHz emission with a sharp spectral profile; this emission lasts all four hours of both epochs and perhaps for the two weeks between epochs, indicating a continuous supply of high-speed electrons in a closed magnetic structure. The second and third epoch both have short-duration events with a downwards sweep in frequency, a potential signature of source motion away from the star. The 1-8.5 GHz emission is predominantly left circularly polarized, whereas both detected 224-482 MHz events are right circularly polarized. The 8.4-GHz radio corona shows enhanced emission throughout the first epoch, which is resolved into two components with a separation of 0.8 stellar diameters, with flares occurring in both components separated by 30 minutes. While AD Leo shows vigorous and frequent signatures of magnetic activity at all frequencies observed, the events at different radio frequencies, and thus different coronal heights, have no immediately apparent interconnection.

6.1 Introduction

Magnetically active M dwarfs flare regularly and energetically, with potentially dramatic consequences for planetary atmospheres. Solar observations have found that flare energy is correlated with coronal mass ejection (CME) kinetic energy (Yashiro

& Gopalswamy 2009) and weakly with solar energetic particle flux at Earth (Kahler 2013). If these relationships apply to flare stars, then CMEs occur at a tremendous, perhaps implausible, rate (Drake et al. 2013; Osten & Wolk 2015), potentially completely eroding planetary atmospheres (Khodachenko et al. 2007; Lammer et al. 2007). Energetic CMEs form shock fronts, which accelerate protons to relativistic speeds; a proton event associated with a large (10^{34} erg) stellar flare may almost entirely deplete the ozone from a planetary atmosphere (Segura et al. 2010).

M3 dwarf AD Leo is a prolific source of energetic flares (Lacy et al. 1976). A 10^{34} erg flare on AD Leo was observed spectroscopically and photometrically in the ultraviolet and optical (Hawley & Pettersen 1991), providing a template for theoretical predictions of the effects of M dwarf activity on planetary atmospheres and habitability (Buccino et al. 2007; Segura et al. 2010; Venot et al. 2016).

These energetic flares are powered by AD Leo's strong magnetic field. Observations of magnetically sensitive line profiles in Stokes I, which is sensitive to the average field strength along the line of sight (independent of field polarity), reveal that the star is strongly magnetized, with consistent measured average surface fields across decades of 2.8 kG (Saar & Linsky 1985) to 2.9 kG (Reiners & Basri 2007; Shulyak et al. 2014). Modeling of these data provide estimates of the magnetic field coverage: Saar & Linsky (1985) estimate that 73% of the star was covered in an average field strength of 3.8 kG, and Shulyak et al. (2014) use broad line wings to infer maximum surface magnetic fields of 6.5 kG covering 10-20% of the star. Spectropolarimetric observations of Stokes V line profiles, which are sensitive to the large-scale line-of-sight magnetic flux (opposite polarity small-scale magnetic structures cancel out), detect 7% of the magnetic flux detected in Stokes I (Reiners & Basri 2009b). Morin et al. (2008) used the periodic time variation of the Stokes V line profile to reconstruct the large-scale magnetic field of the star via Zeeman-Doppler Imaging (ZDI), finding that in both 2007 and 2008 the magnetic dipole field was aligned with the rotational axis, at an inclination of 20° to the line of sight, with the southern magnetic pole visible with maximum inferred large-scale field strength of 1.3 kG.

AD Leo's well-characterized magnetic field structure provides the context for interpreting its radio emission. It produces persistent non-thermal microwave emission, attributed to incoherent gyrosynchrotron emission. This quiescent, variable emission has low-level values of order 250μJy at 5 GHz, in rough agreement with the Güdel-Benz relation, which describes the correlation between the radio and X-ray

luminosity of active stars (Gudel et al. 1993). Very long baseline imaging (VLBI) so far has not resolved AD Leo's radio corona, implying a source size less than 1.4 stellar diameters for a small flare at 1.7 GHz (Benz et al. 1995), and a conservative upper limit of 1.8 stellar diameters at 8.4 GHz during a period of quiescence with a small flare (Pestalozzi et al. 2000). However, VLBI observations have at times resolved the coronae of other active M dwarfs, including YZ CMi (Pestalozzi et al. 2000) and UV Cet (Benz et al. 1998; Bower et al. 2009), showing that the bright non-thermal continuum radio emission often comes from large-scale features in the magnetosphere. Modelling of the decay timescale of large flares on AD Leo suggests that they occur in magnetic loops with size comparable to the stellar photosphere (e.g., Mullan et al. 2006), which has an angular size of 0.8 mas, making AD Leo a promising target for further VLBI observations.

In addition to non-thermal continuum radio emission, AD Leo produces intense coherent radio bursts, where the coherent emission mechanism is identified by rapid time variability, high brightness temperature, strong (up to 100%) circular polarization, and/or narrowband/sharp spectral structure. Solar and stellar coherent radio bursts are attributed to one of two mechanisms: plasma emission, at the first or second harmonic of the local plasma frequency; or electron cyclotron maser (ECM) emission, at a low harmonic of the local cyclotron frequency. For both emission mechanisms, a moving source produces a distinctive spectral signature: as the source propagates through regions with different plasma density or magnetic field strength, the emission frequency varies. With a model for the density and magnetic field strength of the stellar corona, frequency drift rates of coherent radio bursts can be used to calculate speeds of coronal sources, a technique applied to detect solar CME shock fronts and high-speed electrons. Solar radio bursts, reviewed in Bastian et al. (1998), are classified by their morphology in the dynamic spectrum, including duration and frequency drift rate. Solar Type II radio bursts, produced at the shock fronts of coronal mass ejections, sweep through a decade in frequency on the relatively long timescale of minutes, tracing their outwards motion at speeds of hundreds to thousands of km/s. Solar Type III radio bursts sweep through a decade in frequency on the timescale of seconds or less, reflecting source speeds of order 0.1c, associated with high-speed electrons streaming away from the acceleration site, which is a magnetic reconnection point in a flare or the shock front of a CME; when the accelerated electrons occur on open field lines, the bursts extend to very low frequencies as the electrons move away from the Sun. Solar Type II and Type III bursts are both correlated with solar energetic proton events at Earth (Kouloum-

vakos et al. 2015), so searching for analogous radio bursts on nearby stars can shed light on the space weather environment (CMEs and energetic particles) experienced by planets around those stars.

AD Leo is known to produce intense coherent bursts at 1 to 5 GHz (e.g. Lang et al. 1983) and luminous bursts at hundreds of MHz that are likely coherent as well (Spangler & Moffett 1976). The bursts have a wide range of characteristics, including many events with rapid time variability and short duration and also some long-duration events where the coherent nature is identified by narrow bandwidth and strong circular polarization (White et al. 1986). A number of AD Leo radio bursts have been observed with dynamic radio spectroscopy (Güdel et al. 1989; Bastian et al. 1990; Lecacheux et al. 1993; Abada-Simon et al. 1994, 1997; Stepanov et al. 2001), with fractional bandwidth $\Delta\nu/\nu < 0.1$, with frequent detections of rapid time variability and high positive and negative frequency drift rates. Osten & Bastian (2006, 2008) extended the fractional bandwidth of dynamic spectroscopy of AD Leo by observing bursts at 1.12-1.62 GHz. Osten & Bastian (2006) report short duration events with drift rates implying upwards and downwards source motion at relativistic speed that provide evidence for density variations on scales an order of magnitude smaller than the thermal density scale height, and another event with a slower drift rate implying an outwards source speed of 1200-12000 km/s, the right order of magnitude for a coronal shock front. The upgraded Karl G. Jansky Very Large Array (VLA) now makes it possible to greatly extend the bandwidth of stellar dynamic spectroscopy, offering the possibility of tracking coronal sources across coronal regions varying by an order of magnitude in plasma density or magnetic scale height.

This is Paper III in a three-part series. We present here three epochs of 4 hours each of simultaneous observations of AD Leo with the Karl G. Jansky Very Large Array (VLA) and the Very Long Baseline Array (VLBA). The VLA observations provide sensitive wide-bandwidth spectroscopy of coherent stellar radio bursts, covering 0.224-0.482 and 1-4 GHz simultaneously. The VLA observations belong to a 58-hour survey of active M dwarfs, described in Paper I. Paper II presents an analogous data set, wide-bandwidth radio spectroscopy with high-resolution imaging, for flare star UV Ceti. High resolution imaging with the VLBA, covering 8.288-8.544 GHz, is described here for AD Leo.

6.2 Observations

The three 4-hour observations occurred in 2015 on July 5, July 19, and September 5. We used the VLA in subarray mode to observe three bands simultaneously, P band (0.224-0.482 GHz), L band (1-2 GHz), and S band (2-4 GHz). After calibration, we shifted the phase center to the target star, subtracted background sources from the complex visbilities and averaged over all baselines to measure the flux of the target star, producing Stokes I and V dynamic spectra showing the dependence of the stellar flux on time and frequency. The data calibration and production of dynamic spectra are described in more detail in Paper I.

The simultaneous VLBA observations covered 8.288-8.544 GHz, a bandwidth of 256 MHz, in dual polarization. The observations were cross-correlated using the DifX correlator (Deller et al. 2007) with a channel resolution of 0.5 MHz and an integration time of 2 seconds. Time and bandwidth smearing limit the field of view to a few arcseconds, preventing any sources other than the target from contributing to the visibilities. The correlation was performed with a phase center of 10:19:35.707, +19:52:11.43 for July 5 and 19, 2015 and 10:19:35.721, +19:52:11.32 for September 5, 2015; in all epochs the phase center is close enough to the star that the effects of time and bandwidth smearing on the measured stellar flux are negligible. The observations included 1-3 scans on a bright calibrator, OJ287 and/or 4C39.25, for bandpass calibration and repeated observations of J1024+1912 as a phase reference source, cycling between 2 minute scans on AD Leo and 1 minute scans on the phase reference source.

We calibrated the data in AIPS using the VLBA utilities, following the procedure outlined in the AIPS Cookbook Appendix C and VLBA Memo #37, "Flux Calibration on the VLBA." We used used routine VLBAFRGP to fringe-fit on J1024+1912 without a source model (assuming a point source) and interpolate its rate and phase solutions to apply to the target field. We used AIPS routine **clcor** to correct the expected drift of the source over the course of the 4-hour observing blocks due to proper motion and parallax, based on prior measurements of these quantities. The drifts we subtracted from each epoch were, in the format ($\Delta\alpha \cos\delta$, $\Delta\delta$): (0.0368,-0.0595) mas/hr on July 5, 2015; (0.0596,-0.0638) mas/hr on July 19, 2015; and (0.0825,-0.0532) mas/hr on September 5, 2015.

After calibrating, we imaged to determine the location of AD Leo in each epoch and shifted the phase center to the location of peak flux before averaging to 6-second integrations and 8-MHz channels. We then transferred the data to CASA. In CASA,

we imaged the phase reference source, using this as a model for a complex gain calibration on the phase reference source to correct the relative amplitudes of the spectral windows and polarizations, solving for one solution per scan and interpolating to apply these solutions to the AD Leo field. The Los Alamos antenna was entirely flagged at this stage for July 19, 2015 due to rapidly variable amplitudes. We used our code **tbavg** to average over the baselines to produce Stokes I and V time series for the star. To measure the total stellar flux in the time series, we produced the time series using only short baselines on which the star was not resolved: baselines shorter than 2 Mm on July 5 and September 5, 2015, and shorter than 4 Mm on July 19, 2015. We divided the data into half hour intervals to produce clean images in Stokes I and V as well as producing a clean image of the full duration of each epoch.

6.3 Coherent emission

Figures 6.1 to 6.3 show the 0.2-4 GHz Stokes V dynamic spectra and the 8.4-GHz Stokes I and V time series for the three epochs. For the dynamic spectra, we show only Stokes V because the Stokes I dynamic spectra are strongly contaminated by a bright background source in the AD Leo field. We detected strongly circularly polarized, likely coherent, emission in all three epochs. Comparing to the lack of bright coherent bursts in six 2-hour blocks of VLA-only data, presented in Paper I, it seems to be a lucky coincidence that we detected luminous bursts in all 3 epochs of the simultaneous VLA and VLBA observations.

6.3.1 Long-duration coherent radio storms

The first two epochs both have radio "storms": bright radio bursts with nearly 100% left circular polarization (LCP) that last for the entire 4-hour observation, but with variable spectral structure over that time. The intense emission is restricted in bandwidth, covering roughly 1.1 to 1.6 GHz in both epochs, with a sharp cutoff in intensity at these boundaries, and weaker (few mJy) LCP emission above and below these frequencies across the 1-4 GHz range. In both epochs, the intense emission has narrowband substructure that gradually drifts upwards in frequency, with multiple bright features that repeat a similar drift at different times. Figure 6.4 shows the spectrum of Stokes I and V and fractional circular polarization averaged over the duration of the first epoch. The wide bandwidth of our observations enables detection of both the low and high frequency cutoffs of long-duration coherent emission from AD Leo. Previous observations of narrowband coherent emission on AD Leo

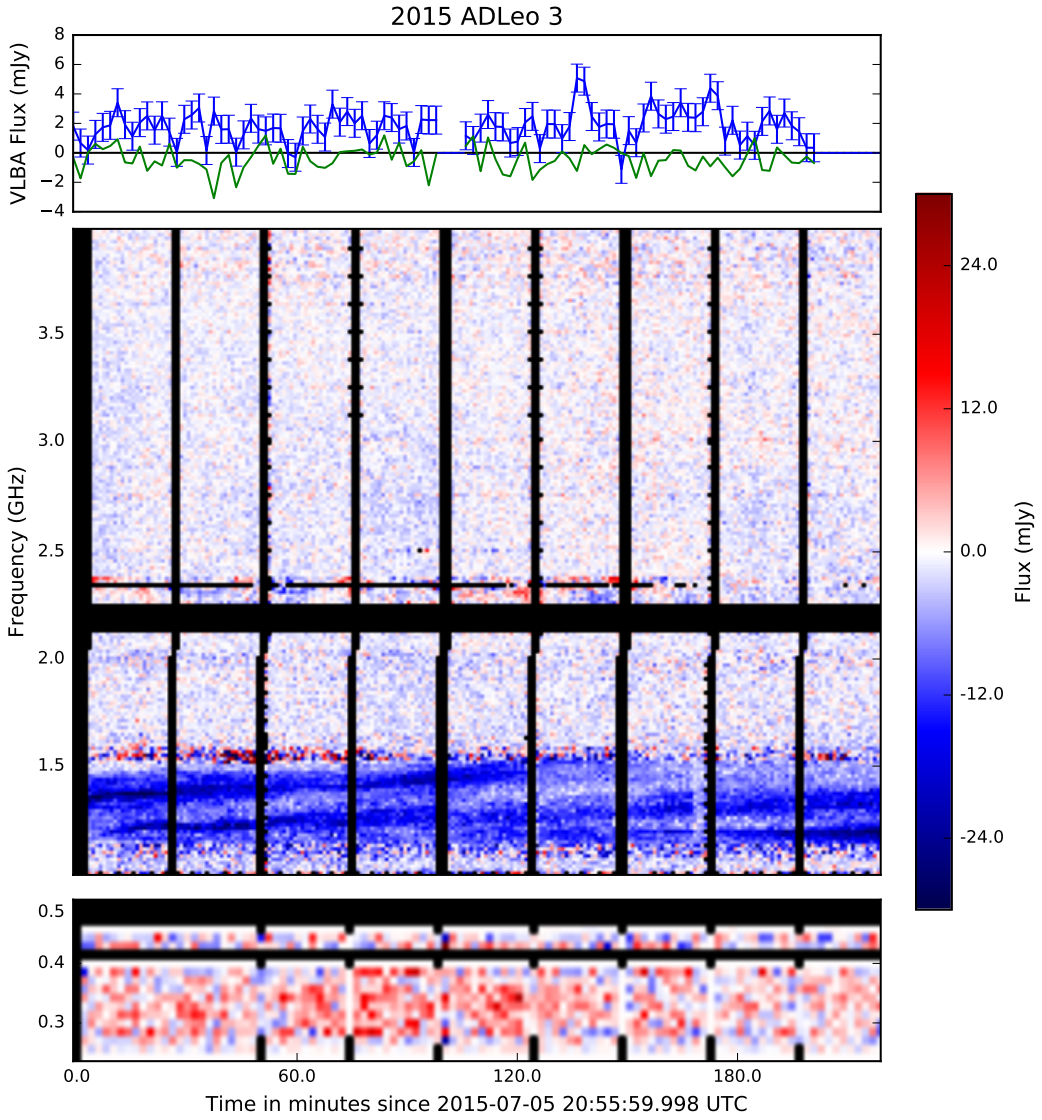

Figure 6.1 Stokes V 0.2-4 GHz dynamic spectrum and 8.3-8.5 GHz Stokes I and V times series for the observation on July 5, 2015. In the upper panel, the Stokes I flux is shown in blue and Stokes V in green. Error bars on Stokes V are not shown but are similar to Stokes I. The dynamic spectrum is binned to a frequency resolution of 16 MHz for all bands, and a time resolution of 60 sec for 1-4 GHz and 120 sec for 0.22-0.48 GHz and 8.3-8.5 GHz. Note that 0.22-0.48 GHz is stretched on the frequency axis compared to 1-4 GHz to make structure in the low-frequency band more visible.

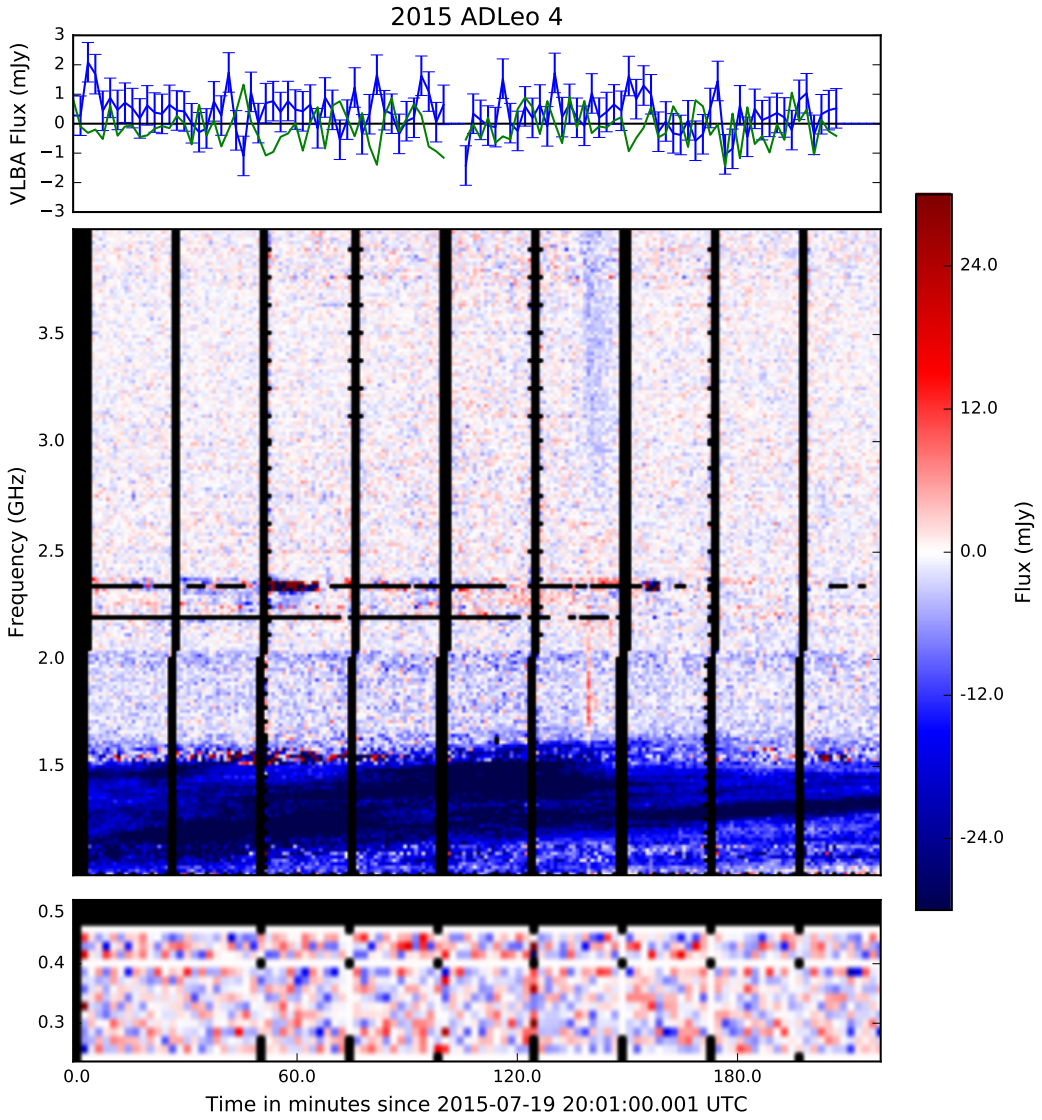

Figure 6.2 Stokes V dynamic spectrum and 8.3-8.5 GHz Stokes I and V times series for the second epoch, in the style of Figure 6.1.

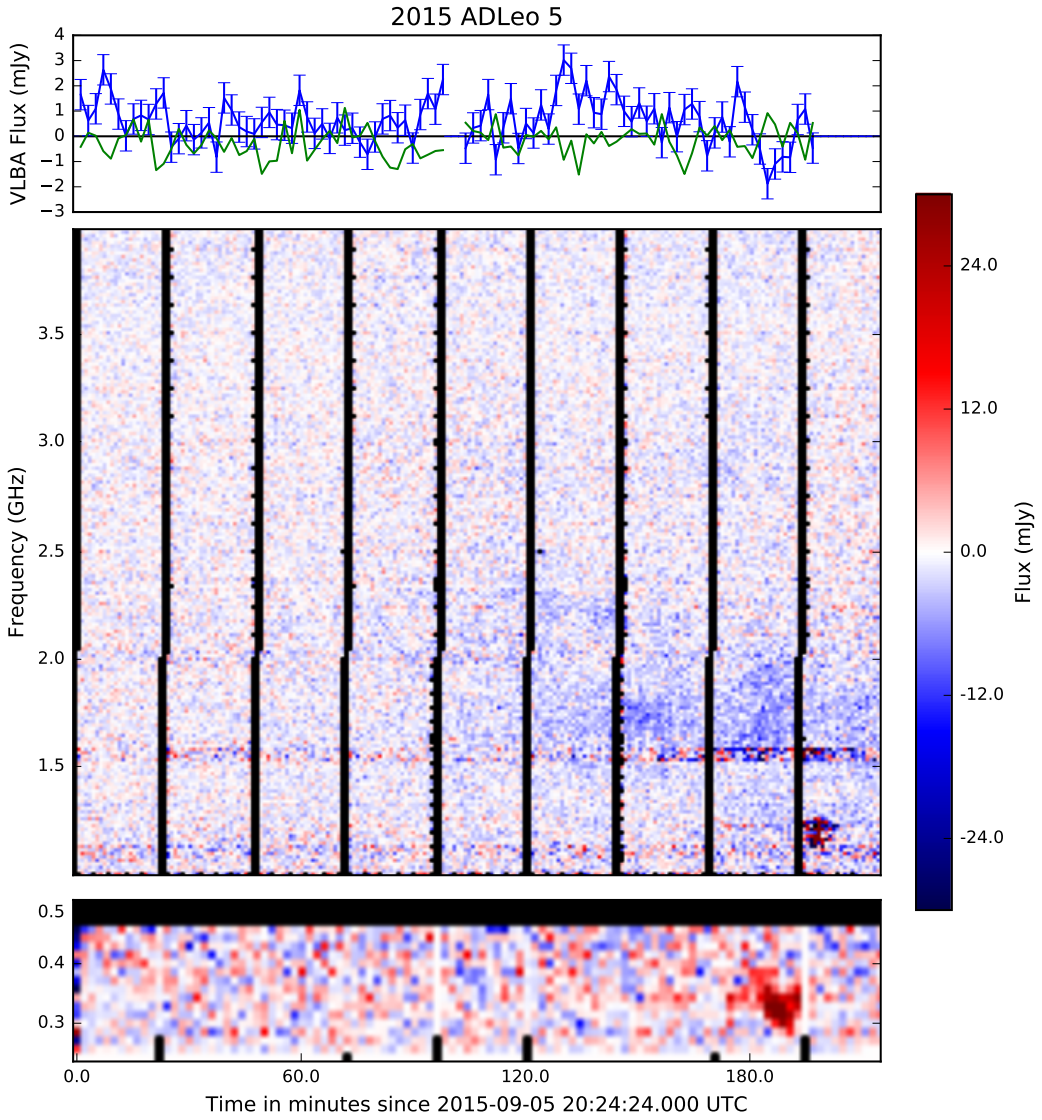

Figure 6.3 Stokes V dynamic spectrum and 8.3-8.5 GHz Stokes I and V times series for the third epoch, in the style of Figure 6.1.

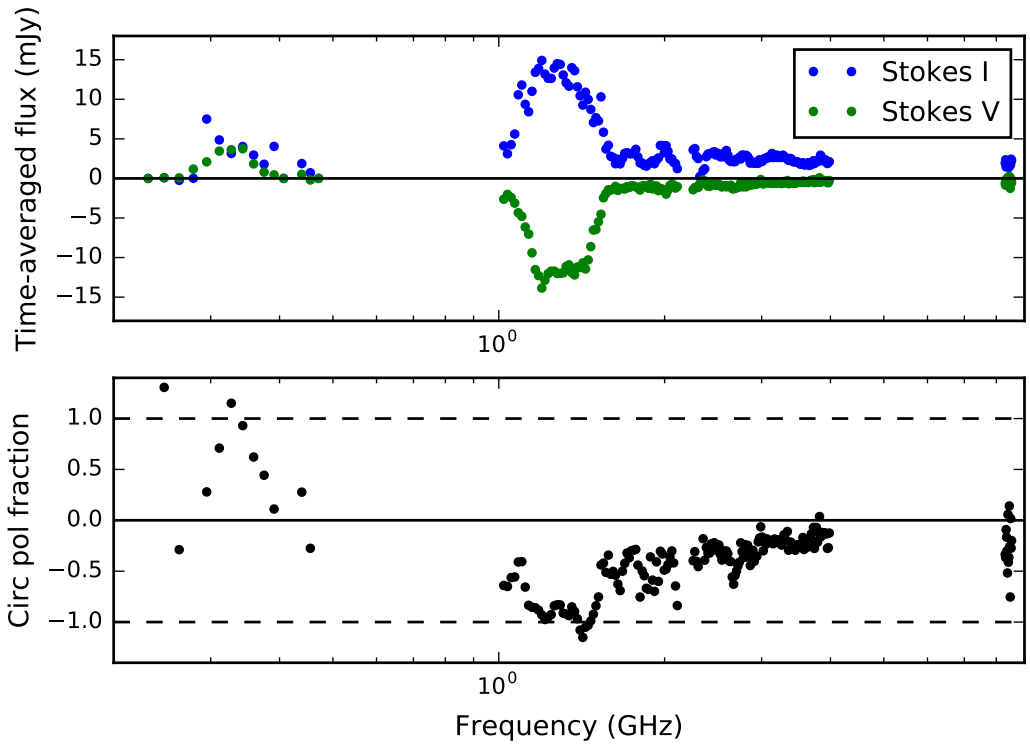

Figure 6.4 0.2-8.5 GHz spectrum of AD Leo averaged over the 4-hour observation on July 5, 2015. This is the time-averaged version of the dynamic spectrum shown in Figure 6.1. The spectrum is binned to a resolution of 16 MHz. Notable features are the flip in the sense of polarization from low to high frequencies, the ~100% polarization of the burst at 1.1-1.6 GHz, and the sharp dropoff in intensity above and below those frequencies.

include a long-duration event reported by White et al. (1986), in the form of a 2-hour long burst detected at 1.415 GHz and not 1.515 GHz; and short-duration narrowband coherent spikes whose full bandwidth was measured by Osten & Bastian (2006).

The first epoch is also detected at 224-482 MHz but with the reverse sense of polarization, with broadband slowly time-variable RCP emission; in an image of the entire 224-482 MHz band averaged over the full 4 hours, we measure a Stokes I flux of 4.5±1.4 mJy and Stokes V of 2.7±0.2 mJy, so the low frequency transient emission has at least ~60% right circular polarization. The star is undetected at 224-482 MHz in the second epoch, with 3σ upper limits on source flux of 4.2 mJy in Stokes I and 0.7 mJy in Stokes V.

The latter half of the third epoch also contains strongly left circularly polarized

emission at 1-4 GHz, at the lower (few mJy) intensities seen in the broadband LCP emission in the earlier epochs. This epoch, 2 months after the first epoch, does not show the intense 1.1-1.6 GHz emission seen in the first two epochs, which are separated by 2 weeks. The similar frequency structure, frequency drift features, and intensity of the 1.1-1.6 GHz emission in the first two epochs suggests that this luminous event may be ongoing between the 2 epochs over the course of at least 2 weeks.

Based on the strong circular polarization and narrowband frequency structure, the 1.1-1.6 GHz feature is most likely coherent emission, either plasma emission or electron cyclotron maser. For both emission mechanisms, the frequency depends only on conditions in the source region (plasma density or magnetic field strength), so the bandwidth indicates the range of conditions in the source region. The sharp dropoff in intensity below 1.1 and above 1.6 GHz indicates that the bright 1.1-1.6 GHz feature likely comes from a closed magnetic field structure, where there is a limited range of physical conditions. The ratio of $\nu_{\rm max}/\nu_{\rm min} = 1.45$ for the bright emission corresponds to $n_{\rm e,max}/n_{\rm e,min} = 2.1$ (implying a source height of 0.75 density scale heights) for plasma emission or $B_{\rm max}/B_{\rm min} = 1.45$ for ECM. Solar Type I bursts sometimes have a narrowband coherent emission component, albeit with a much smaller fractional bandwidth than seen here, where the restricted bandwidth is attributed to the range of physical conditions in the source region, where the source region is a closed magnetic structure. An alternative explanation for the restricted bandwidth of these bursts is that the emission is directionally beamed, with the source geometry causing only the 1.1-1.6 GHz emission to be directed into our line of sight.

The sense of circular polarization of coherent radio bursts depends on the orientation of the magnetic field in the source region relative to the line of sight. Zeeman Doppler Imaging of AD Leo by by Morin et al. (2008) in 2007 and 2008 found that AD Leo has a strong dipole field aligned with its rotational axis, which is at a 20° inclination, almost pole-on. The magnetic field structure was very similar between the two years, with a strong polar spot with maximum flux of 1.3 kG with the longitudinal magnetic field pointing into the star. If the source region in 2015 has the same magnetic field orientation, then x-mode waves from directly above the pole of the star correspond to LCP emission and o-mode waves to RCP emission. Since the star is seen pole-on, emission from the stellar limb should have the opposite sense of polarization.

There is a flip in polarization between 1-4 GHz (LCP) and 0.224-0.482 GHz (RCP), seen in both epochs 3 and 5. Previous detections of coherent bursts at >1 GHz on AD Leo also include strongly right polarized emission (e.g. Osten & Bastian 2008). The flip in polarization between high and low frequencies during the epochs observed here can be attributed to one of three possibilities:

1. *Flip in longitudinal magnetic field direction between source regions.* If all the emission is via the same mechanism and in the same mode, then the flip in polarization is due to a flip in longitudinal magnetic field direction between the high- and low-frequency source regions. Given the pole-on viewing angle, a possible explanation is that the high frequency emission comes from the strongly magnetized low corona above the magnetic pole, and the low-frequency emission comes from above the stellar limb, where the large-scale magnetic dipole field of the star has reversed direction relative to the line of sight; this configuration would imply x-mode emission, consistent with electron cyclotron maser in a strongly magnetized, low-density plasma.

2. *Change in emission mechanism.* The sense of circular polarization depends on the emission mechanism. Fundamental plasma emission is expected to be o-mode because the plasma frequency is below the minimum frequency for x-mode propagation (Dulk 1985). ECM is expected to be x-mode and first harmonic in the low-density limit (Melrose et al. 1984). The high-frequency LCP and low-frequency RCP mode emission seen on AD Leo may be analogous to the Sun, where the conditions for ECM occur only in strongly magnetized regions of the low corona (Régnier 2015; Morosan et al. 2016) and low-frequency coherent emission is generally attributed to plasma radiation.

3. *Single emission mechanism with emission in different modes due to variation in source conditions.* For ECM, the mode of emission depends on the ratio of plasma frequency to cyclotron frequency (Melrose et al. 1984), the ambient density of Langmuir waves (Zhao et al. 2015), and the energy distribution of the exciting electrons (Zhao et al. 2016). (Stepanov et al. 1999) predict that plasma radiation at the second harmonic can have o-mode polarization in regions where the squared ratio of plasma frequency to cyclotron frequency ν_p^2/ν_c^2 is between 1 and 5, due to preferential absorption of x-mode by gyroresonant absorption at high harmonics, with lower frequencies from less strongly magnetized regions reverting to moderate x-mode polarization.

Morin et al. (2008) connect the rotational modulation of AD Leo's spectropolarimetric signature between 2007 and 2008 to measure a rotation period of 2.2399±0.0006 days. If this rotation period is accurate, the start time of the July 5 and 19 observations is separated by 83°in rotational phase, and the 4-hour duration corresponds to 27°of rotational phase. If this emission is continuous between the two epochs and rotationally modulated, it is detected for >30% of the stellar rotation period.

Coherent emission mechanisms require a velocity inversion, an excess of high-speed electrons. The long-duration coherent emission at 1.1-1.6 GHz requires an ongoing supply of high-speed electrons for at least 4 hours at a time and perhaps for the entire 2 weeks between the first and second epochs. Two possible scenarios that could supply these high speed electrons are:

- Gradual emergence of magnetic flux in the stellar photosphere which causes ongoing magnetic reconnection in closed magnetic field structures in the corona, as seen in Type I solar storms. Accelerated electrons move away from the magnetic reconnection site with higher speed electrons streaming ahead, forming electron beams with a velocity inversion. Coherent Type I bursts are narrowband and strongly polarized; the narrow bandwidth corresponds to the range of physical parameters in the closed magnetic structure that is interacting with the emerging flux.

- A large-scale current system which creates a velocity inversion when electrons are mirrored at magnetic footpoints. Such a current system could be driven by the interaction of the star's large-scale magnetic field with ambient plasma ejected from the star or a close-in planet, analogous to the radio aurorae of planets and brown dwarfs. In this scenario, the high frequency cutoff is analogous to the sharp upper frequency cutoff in Jupiter's decametric emission, corresponding to the maximum field strength in the emitting region above the magnetic pole. In this scenario, the lower frequency cutoff might be due to source geometry (consistent with scenario #1 listed above for the explanation of the reversed sense of polarization observed at low frequencies).

6.3.2 Short-duration radio bursts

In addition to the long-duration radio "storms" described above, AD Leo produced a few shorter bursts that show frequency drift over time, which can be caused by source motion. In epoch 2, two features are seen in Figure 6.2 occurring at roughly 140 minutes from the start of the observations, an RCP burst from 1.6-2 GHz and

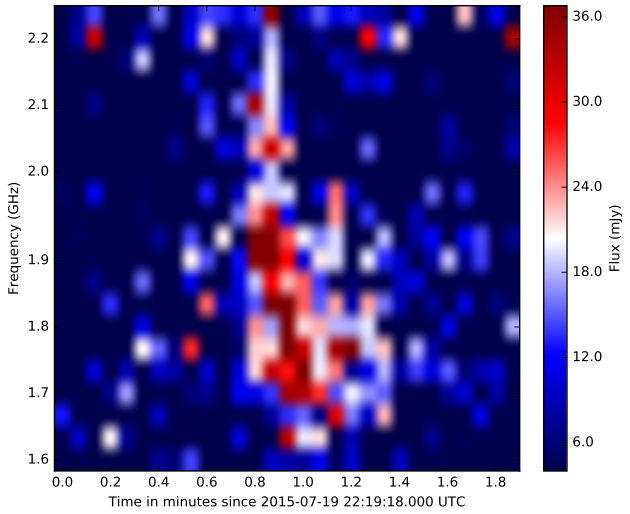

Figure 6.5 RCP dynamic spectrum of a short-duration burst during the second epoch. Note that the color scale consists of entirely positive flux values, unlike the other dynamic spectrum plots in this paper for which the color scale is symmetric about zero.

an LCP burst from 2.5-4 GHz. The LCP feature starts about 15 seconds earlier than the RCP, with a bright leading edge of emission at frequencies from 2.5-4 GHz and a slow decline in intensity over 5 minutes; the low intensity and broad time and frequency profiles mean the burst has no discernable frequency drift. The RCP burst, highlighted in Figure 6.5 is more intense and short, with a duration of about 30 sec and a negative frequency drift of approximately 120 MHz/sec. If the frequency drift is due to source motion, then $\nu/\dot{\nu}$ provides an estimate of the timescale for the source to traverse a scale length in density or magnetic field strength (depending on whether emission is at the plasma frequency or the cyclotron frequency). For the RCP burst in epoch 2, $\nu/\dot{\nu} \sim 15$ sec.

In the third epoch, a 290-360 MHz RCP burst with peak flux of 80 mJy and a duration of 5 minutes occurred at 190 minutes after the observation start time. Figure 6.6 shows the Stokes V dynamic spectrum of the event. Based on visual inspection, the event has a tentative negative frequency sweep of 0.17 MHz/sec, corresponding to $\nu/\dot{\nu} \sim 2000$ sec. This drift cannot be explained within the framework for interpreting solar Type II bursts associated with coronal mass ejection shock fronts, because a density scale height of order 100,000 km would imply a speed of order 50 km/s, much too low to form a shock in the solar corona (where typical Alfvén speeds are hundreds of km/s), let alone in the strongly magnetized environment around

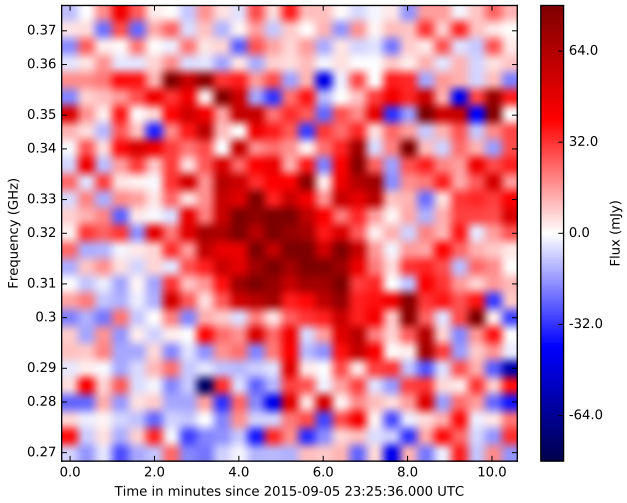

Figure 6.6 Stokes V dynamic spectrum of a short-duration burst during the third epoch.

AD Leo.

For all the observed short-duration events, the restricted bandwidth of the event, with a clear lower frequency cutoff, means that even if the frequency drift is due to outwards source motion, there is no evidence that the disturbance continues to propagate outwards beyond the end of the burst.

6.4 Location and size of the 8.4-GHz radio corona

After producing clean images using the full 4 hours of VLBA data from each epoch, we used the CASA Viewer tool **gaussfit** to measure the time-averaged source location, size, and flux. Our measurements of the star's position are: (July 5, 2015) 10:19:35.7223055, +19.52.11.3708542; (July 19, 2015) 10:19:35.7232330, +19.52.11.3517819; (September 5, 2015) 10:19:35.7288399, +19.52.11.2847967. Statistical errors on the positions are of order 40 μas for epoch 1, 70 μas for epoch 2, and 100 μas for epoch 3, but these errors do not include systematic error introduced by phase referencing and uncertainty on the absolute position of the phase reference source.

In the first epoch, the star's quiescent emission is at high levels with an integrated flux of 2.1±0.1 mJy in Stokes I with moderate left circular polarization of 20% in the total flux. The Stokes V emission, left circularly polarized at -400±50 μJy, was unresolved. The image of the stellar emission over the full epoch is resolved with angular size 1.25±0.13 x 0.99±0.31 mas, or 1.6 x 1.3 stellar diameters. If these

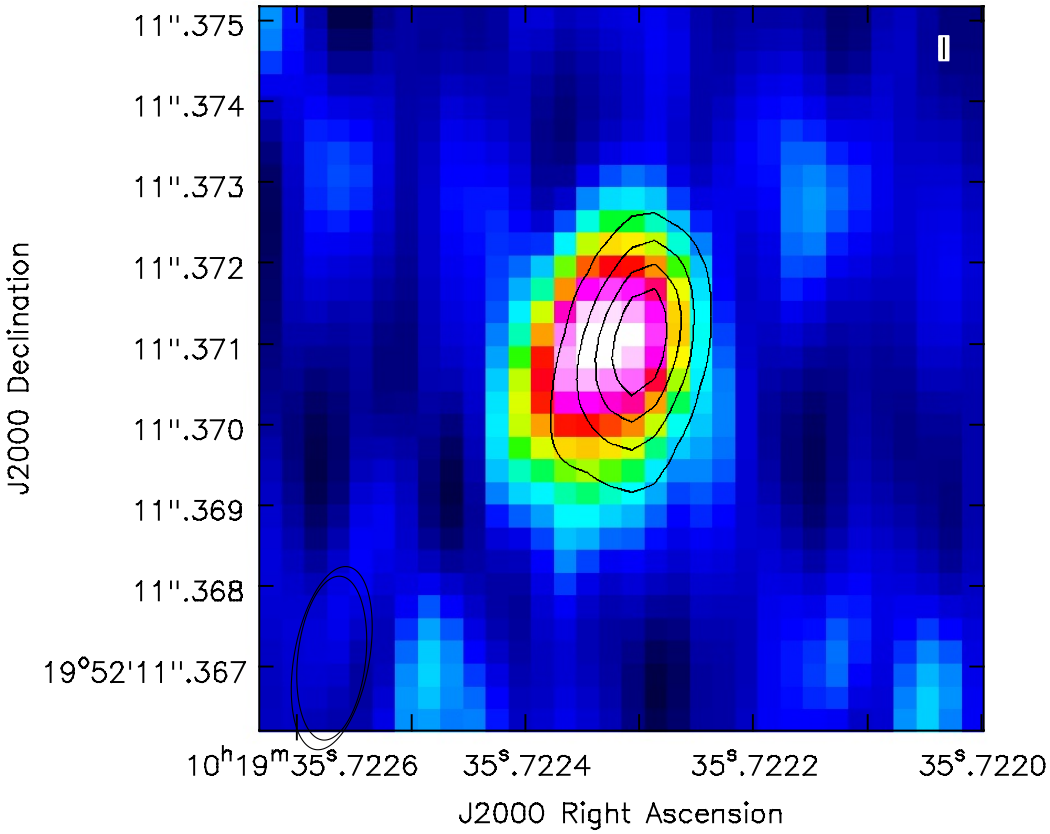

Figure 6.7 Two 8.2-8.5 GHz flares during epoch 1. Flare 1 (contours, seen in Figure 6.1 time series at ~ 140 min after observation start) is aligned with the location of the quiescent Stokes I peak, and flare 2 (color image; occurs 30 min later) is aligned with the location of the quiescent Stokes V peak. The peak flux of both flares is ~3-4 mJy.

truly reflect the extent of the source they imply a brightness temperature of 3×10^6 K; however this value may be higher given that the source structure is perhaps not well described by a Gaussian fit. Indeed, inspection of the images of 30-minute intervals during the observations suggests that this extended structure may be attributed to two components separated in the east-west direction by ~600 μas, or 80% of the photospheric diameter. The west component dominates the Stokes I emission in quiescence and is unpolarized, with Stokes V emission centered on the east component throughout the observations. There are two unpolarized few-mJy flares apparent in the 8.4-GHz time series in Figure 6.1: the first of these, at ~140 min after the observation start time, is centered on the western component, and the second, about 40 minutes later, on the eastern component; these two events are shown together in Figure 6.7. These preliminary results will be verified and further characterized

prior to publication, with modeling of the visibilities to determine whether each of the components is resolved.

In the second and third epochs, the stellar quiescent emission is at typical low-level quiescent fluxes for AD Leo (as reported by Gudel et al. 1993). The time-averaged flux is 410±30 μJy in Stokes I with a marginal Stokes V detection of -60±25 μJy. The measured source size with **gaussfit** is marginally resolved in one direction, with an extent in that direction of 800±300 μas. The VLBA data from the latter half of the third epoch are of poor quality, with low and rapidly varying amplitudes for a number of antennas. Using only the first 1.5 hours of the third epoch, we obtain a Stokes I flux of 700±100 μJy and a Stokes V detection of -230 ± 40 μJy, giving 30% left circular polarization.

The low to moderate degree of circular polarization observed in most epochs is consistent with the expected levels for gyrosynchrotron emission. While it is possible that the heightened 8.4-GHz "quiescent" emission of the first epoch is associated with the 1.1-1.6 GHz coherent storm, such an interpretation is called into question by the low-level 8.4-GHz emission observed in the second epoch while the 1.1-1.6 GHz coherent storm persisted.

The 8.4-GHz stellar emission is unpolarized or left circularly polarized in all of our VLBA observations. The sense of polarization is consistent with the long-duration coherent emission observed at 1-2 GHz. Gyrosynchrotron is expected to be polarized in the x-mode (Dulk 1985), indicating that the left polarized emission imaged for the eastern feature in the first epoch should emerge from a region with negative longitudinal magnetic field, as we expect directly above the pole of the star, over the center of the photosphere for our line of sight. We speculate therefore that of the features observed in the VLBA imaging of the first epoch, the eastern feature, which is fainter and polarized and is the location of the later flare, is located above the stellar magnetic pole near the center of the stellar disk, while the western feature, which is brighter and unpolarized and is the location of the earlier flare, is located above the stellar limb.

6.5 Conclusions

As part of a search for stellar eruptions, we have conducted simultaneous wide-bandwidth dynamic radio spectroscopy and very long baseline imaging of active M dwarf AD Leo. The dynamic spectroscopy over 0.2-4 GHz, an unprecedented wide bandwidth for stellar observations, offers the possibility of tracking electron

acceleration sites (including the shock fronts of fast coronal mass ejections) across regions varying by more than an order of magnitude in density or magnetic field strength. The very long baseline imaging achieves a resolution comparable to the size of the photosphere, enabling measurement of the location of flare emission relative to the quiet radio corona. Our observations do not find evidence of stellar eruptions, but should not be taken to rule out their presence. Instead, they provide a novel view of AD Leo's dynamic radio corona, which sustains diverse manifestations of stellar activity at different radio wavelengths.

The wide bandwidth of the dynamic spectra enabled measurement of the bandwidth of coherent bursts and comparison of the sense of polarization across the frequency spectrum. A 100% left circular polarization coherent radio "storm" is detected throughout the 4-hour observations on both July 5 and July 19, 2015, with a sharp dropoff in emission intensity observed below 1.1 GHz and above 1.6 GHz; these cutoffs in emission frequency are likely due to a limited range of source conditions in the source region, as expected for emission from a closed magnetic structure. The storm shows bright narrowband substructure that drifts gradually upwards in frequency, with multiple features showing similar drift rates. The shared properties of these events highlight the possibility that this coherent storm is sustained over the course of the two weeks between epochs. We detect two shorter-duration (minutes-long) events with a potential downwards frequency sweep that may indicate source motion away from the star, but these events drift across a relatively narrow portion of the overall dynamic spectrum, providing no evidence that the disturbances move beyond the closed stellar magnetosphere. The detected stellar emission is predominantly left circularly polarized at 1-8.5 GHz and right circularly polarized at 0.22-0.48 GHz, indicating that the line-of-sight magnetic field flips direction between the source regions for the two frequency ranges, or that the two frequency ranges are due to different wave modes (x vs o mode).

In the first epoch, AD Leo's 8.4-GHz corona, which shows heightened levels of quiescent emission and two flares during the 4-hour observation, is resolved into two components separated by 0.8 stellar diameters, with one flare occurring co-located with each quiescent component. These observations demonstrate the potential of VLBI to trace the spatial distribution of energy release in the coronae of nearby active stars. There is no obvious connection between the 8.4-GHz coronal structure and flares, attributed to incoherent gyrosynchrotron emission, and the morphology and timing of coherent emission at 0.22-0.48 and 1-4 GHz, which probe different

coronal heights. We therefore recommend caution in using observations of energy release at low heights (photosphere to low corona) to predict eruptive events or other phenomena that would pass through the outer corona.

6.6 Acknowledgements

This research was conducted in collaboration with Gregg Hallinan and Stephen Bourke, who will be co-authors on the upcoming publication.

This material is based upon work supported by the National Science Foundation under Grant No. AST-1311098.

The National Radio Astronomy Observatory is a facility of the National Science Foundation operated under cooperative agreement by Associated Universities, Inc. This work made use of the Swinburne University of Technology software correlator, developed as part of the Australian Major National Research Facilities Programme and operated under license.

This research has made use of the SIMBAD database, operated at CDS, Strasbourg, France.

J.R.V. thanks the Troesh family and the PEO International Scholar Award program for financial support of her graduate research.

Chapter 7

CONCLUSIONS

In this thesis, I set out to characterize the impact of stellar activity on planets using radio observations of stellar atmospheres. My targets ran the gamut from stars with magnetic activity almost identical to the Sun's to stars whose extreme magnetic activity combines characteristics of the Sun and planets.

Radio facilities have now reached the sensitivity and bandwidth needed to detect the quiet radio Sun at stellar distances. I used the upgraded VLA to detect the thermal radio emission from nearby solar-type stars with solar levels of magnetic activity, setting upper limits on stellar winds and measuring disk-averaged brightness temperatures of 10^4 K, which when combined with ALMA and optical/infrared observations will provide a temperature profile of the atmospheres of these stars from the photosphere through the temperature minimum to the chromosphere. The Square Kilometer Array will greatly extend the distance over which we can observe the quiet radio emission from stars, enabling tracking of stellar magnetic activity cycles on solar-type stars out to 50 pc (White 2004).

Solar and stellar radio bursts far outshine the quiet Sun and have long been detected on nearby stars. Technological improvements including wideband feeds and high-clock-speed digital hardware now enable characterization of these stellar radio bursts with wide-bandwidth dynamic spectroscopy, which offers the potential to track coronal sources moving outwards across multiple density scale heights. I worked on the Starburst project, a facility designed to make use of wideband feeds and digital hardware for spectroscopic monitoring of nearby active stars, with tasks including project management, identification of scientific and technical requirements, control code, and commissioning. To prepare to propose multi-wavelength campaigns with Starburst, I conducted a 58-hour survey of active M dwarfs with the VLA, taking advantage of the upgraded VLA's wide bandwidth to characterize the rate and frequency structure of coherent radio bursts on active M dwarfs, finding that the population of luminous coherent bursts on active M dwarfs observed from 0.2 to 6 GHz peaks in intensity and frequency at 1 GHz, suggesting that this population is largely associated with disturbances confined to the low stellar corona; there is no analog to this population of coherent bursts on the Sun. This result em-

phasizes that to search for eruptive stellar events on magnetically active stars, it will be beneficial to push the search to increasingly low radio frequencies, which probe further distances from the star. Ideally, we can observe these frequencies with a wide instantaneous bandwidth, to track sources across a wide range of distances from the star and to balance the trade-off between lower frequency and sensitivity.

One of the goals for Starburst was to trigger VLBA observations to image flaring and eruptive stellar coronae; as a pathfinder for this, I conducted 8.4-GHz VLBA imaging of flare stars UV Cet and AD Leo simultaneous to 24 hours of the VLA dynamic spectroscopy survey. On UV Cet, I stumbled across a radio aurora, with coherent radio bursts with consistent circular polarization and slowly-evolving structure across years, whose ultra-wide bandwidth is powered by current systems in the star's large-scale magnetosphere. I am still improving the calibration of the VLBA data for imaging, but initial results suggest that the 8.4-GHz coherent radio bursts on UV Cet, which must originate near the stellar photosphere, are offset from the quiescent radio emission by $\sim$2 photospheric diameters. Considering the abundance of GHz-frequency coherent radio bursts seen from active M dwarfs, radio aurorae may be a pervasive phenomenon. I would like to conduct radio dynamic spectroscopy of the most rapidly rotating nearby M dwarfs to search for more auroral emitters, targeting stars whose large-scale fields have been mapped by Zeeman Doppler Imaging, and follow up with VLBI of the stellar magnetosphere to measure the locations of coherent radio bursts and characterize the non-thermal electron populations in the large-scale magnetosphere of these stars, providing constraints on the mechanisms that may accelerate the high-speed electrons that power aurorae and other long-duration coherent radio bursts. ALMA observations open a new window on the high-energy tail of the non-thermal electron population, with unexpectedly bright radio emission detected from some young M dwarfs (Hallinan, private communication; MacGregor et al. 2013).

UV Cet's radio aurora extends to low frequencies, which means that when using coherent radio bursts to search for extrasolar CMEs, we must find a way of distinguishing between auroral pulses and eruptive events, even at low frequencies. Searching for periodic repetition is one way of distinguishing but it requires lots of observing time and/or carefully scheduled observations for stars with periods longer than a few hours. Simultaneous optical observations also provide a means of distinguishing between auroral pulses and radio bursts from coronal shock fronts, since large stellar eruptions are expected to be associated with flares, whereas there

is no particular expectation of such an association for auroral pulses. As explored by Crosley et al. (2016), simultaneous optical observations also provide the opportunity to measure the relationship between large flares and stellar eruptions on active stars, calibrating the relationship used to predict CME rates by Osten & Wolk (2015).

On AD Leo, VLA dynamic spectroscopy and VLBA imaging during a period of heightened activity revealed diverse processes in the stellar corona, including a coherent radio storm that likely lasted more than 2 weeks and originated from a relatively small closed magnetic structure, an inversion in sense of polarization between radio emission above and below 1 GHz, and two resolved components of the 8.4-GHz stellar corona separated by almost a stellar diameter. The ability of the VLBA to resolve coronal structures on length scales smaller than the stellar photosphere will be complemented in the next few years by the Gaia mission's sub-mas astrometry, enabling measurement of the relative locations of the stellar photosphere and radio corona. UV Cet and AD Leo are not in the Tycho-Gaia catalog so they do not have proper motion- and parallax-corrected positions in Gaia's recent Data Release 1, but I am reaching out to members of the Gaia team to see if positions could be calculated for these stars. Bringing Gaia positions together with the large-scale magnetic fields measured by Zeeman Doppler Imaging will allow calculation of the stellar magnetic field in the emitting regions of the stellar radio corona, enabling confirmation of the emission mechanism (thought to be mildly relativistic synchrotron at s$\sim$10) and shedding light on the question of why persistent non-thermal radio emission occurs on large scales in the coronae of active stars with no such analog in the Sun. Radio stars also provide an alternative source type to radio galaxies for tying together the VLBA-based ICRF coordinate reference frame and the Gaia coordinate reference frame (Malkin 2016), although radio stars' variable spatial structure may limit the effectiveness.

The Starburst program came to an early end due to structural instabilities in the antennas, but I am eager to continue my involvement in development and commissioning of radio astronomy projects. I am starting a Jansky fellowship at the National Radio Astronomy Observatory in Charlottesville, VA, where I plan to collaborate with Tim Bastian, a leader in the field of solar and stellar radio astronomy. Tim and I have discussed opportunities for me to become involved in commissioning solar observations with ALMA and with low frequency bands on the VLA. I am particularly interested in commissioning polarization calibration on the VLA, which will

prove invaluable for flare star observations, especially in light of a tentative detection of linear polarization in UV Ceti's coherent radio bursts (a detection I omitted from this thesis due to my concerns about errors in polarization calibration).

One of the advantages planned for the Starburst program was its large amount of observing time, with the opportunity to observe ~20 hours a day for years. If extreme 10^{34} erg flares occur on active M dwarfs once per month, we should observe for more than one month to search for the accompanying extreme CMEs that would disrupt planetary atmospheres. This long observing time can be achieved by long-duration targeted observations, as planned for Starburst, or by observations with a field of view that is wide enough to contain multiple M dwarfs. The Owens Valley Long Wavelength Array station, which observes from 20-80 MHz, is an all-sky instrument, combining large field of view and lots of observing time (currently, the limit on the amount of observing time is the vast amount of data generated), making it ideal for searching for stellar space weather events. The upcoming thesis of Marin Anderson will feature an all-sky transient search in Stokes I and V during 100 hours of observing time, adding up to a total of 55000 hours of observations of M dwarfs within 25 pc. The Owens Valley LWA is soon to enter continuous buffered observing, saving high-resolution data for times corresponding to triggers from other transient facilities. I hope to work with the LWA team to extract time series or dynamic spectra for the entire K2 campaigns for upcoming campaign fields that contain nearby flare stars, particularly CN Leo/Wolf 359, a known source of highly energetic flares. I will also work with Gregg Hallinan and collaborator Paul Gardner to schedule simultaneous observations with a small optical telescope when I have scheduled flare star observations on various radio facilities; for nearby active M dwarfs, even a small telescope can detect the multi-magnitude flares most likely to be associated with CMEs. These observations will help build up a framework for the interpretation of stellar coherent radio bursts, improving our ability to use them as diagnostics of energetic processes in stellar coronae. This framework and the diagnostic ability of stellar coherent radio bursts should prove very fruitful in the era of the Square Kilometer Array.

BIBLIOGRAPHY

Aarnio, A. N., Matt, S. P., & Stassun, K. G. 2013, Astronomische Nachrichten, 334, 77, DOI: 10.1002/asna.201211778

Abada-Simon, M., Lecacheux, A., Aubier, M., & Bookbinder, J. A. 1997, A&A, 321, 841

Abada-Simon, M., Lecacheux, A., Louarn, P., et al. 1994, A&A, 288, 219

Aschwanden, M. J., Poland, A. I., & Rabin, D. M. 2001, ARA&A, 39, 175, DOI: 10.1146/annurev.astro.39.1.175

Audard, M., Güdel, M., & Skinner, S. L. 2003, ApJ, 589, 983, DOI: 10.1086/374710, eprint: astro-ph/0303492

Baliunas, S. L., Donahue, R. A., Soon, W. H., et al. 1995, ApJ, 438, 269, DOI: 10.1086/175072

Baliunas, S., Sokoloff, D., & Soon, W. 1996, ApJ, 457, L99, DOI: 10.1086/309891

Bastian, T. S. 1990, Sol. Phys., 130, 265, DOI: 10.1007/BF00156794

Bastian, T. S., Benz, A. O., & Gary, D. E. 1998, ARA&A, 36, 131, DOI: 10.1146/annurev.astro.36.1.131

Bastian, T. S., & Bookbinder, J. A. 1987, Nature, 326, 678, DOI: 10.1038/326678a0

Bastian, T. S., Bookbinder, J., Dulk, G. A., & Davis, M. 1990, ApJ, 353, 265, DOI: 10.1086/168613

Benz, A. O., Alef, W., & Guedel, M. 1995, A&A, 298, 187

Benz, A. O., Conway, J., & Güdel, M. 1998, A&A, 331, 596

Benz, A. O., & Güdel, M. 1994a, A&A, 285, 621

—. 1994b, A&A, 285, 621

Bouvier, A., & Wadhwa, M. 2010, Nature Geoscience, 3, 637, DOI: 10.1038/ngeo941

Bower, G. C., Bolatto, A., Ford, E. B., & Kalas, P. 2009, ApJ, 701, 1922, DOI: 10.1088/0004-637X/701/2/1922, arXiv: 0907.1680 [astro-ph.EP]

Boyajian, T. S., McAlister, H. A., van Belle, G., et al. 2012, ApJ, 746, 101, 101, DOI: 10.1088/0004-637X/746/1/101, arXiv: 1112.3316 [astro-ph.SR]

Buccino, A. P., Lemarchand, G. A., & Mauas, P. J. 2007, Icarus, 192, 582, DOI: 10.1016/j.icarus.2007.08.012, eprint: astro-ph/0701330

Canto Martins, B. L., Das Chagas, M. L., Alves, S., et al. 2011, A&A, 530, A73, A73, DOI: 10.1051/0004-6361/201015314, arXiv: 1103.5332 [astro-ph.EP]

Condon, J. J., Cotton, W. D., Fomalont, E. B., et al. 2012, ApJ, 758, 23, 23, DOI: 10.1088/0004-637X/758/1/23, arXiv: 1207.2439 [astro-ph.CO]

Crosley, M. K., Osten, R. A., Broderick, J. W., et al. 2016, ApJ, 830, 24, 24, DOI: 10.3847/0004-637X/830/1/24, arXiv: 1606.02334 [astro-ph.SR]

Deller, A. T., Tingay, S. J., Bailes, M., & West, C. 2007, PASP, 119, 318, DOI: 10.1086/513572, eprint: astro-ph/0702141

Demory, B.-O., Ségransan, D., Forveille, T., et al. 2009, A&A, 505, 205, DOI: 10.1051/0004-6361/200911976, arXiv: 0906.0602 [astro-ph.SR]

di Folco, E., Absil, O., Augereau, J.-C., et al. 2007, A&A, 475, 243, DOI: 10.1051/0004-6361:20077625, arXiv: 0710.1731

Donahue, R. A., Saar, S. H., & Baliunas, S. L. 1996, ApJ, 466, 384, DOI: 10.1086/177517

Donati, J.-F., Forveille, T., Collier Cameron, A., et al. 2006, Science, 311, 633, DOI: 10.1126/science.1121102, eprint: astro-ph/0602069

Donati, J.-F., & Landstreet, J. D. 2009, ARA&A, 47, 333, DOI: 10.1146/annurev-astro-082708-101833, arXiv: 0904.1938 [astro-ph.SR]

Drake, J. J., Cohen, O., Yashiro, S., & Gopalswamy, N. 2013, ApJ, 764, 170, 170, DOI: 10.1088/0004-637X/764/2/170, arXiv: 1302.1136 [astro-ph.SR]

Drake, S. A., Simon, T., & Brown, A. 1993, ApJ, 406, 247, DOI: 10.1086/172436

Dulk, G. A. 1970, ApJ, 159, 671, DOI: 10.1086/150341

—. 1985, ARA&A, 23, 169, DOI: 10.1146/annurev.aa.23.090185.001125

Fontenla, J. M., Balasubramaniam, K. S., & Harder, J. 2007, ApJ, 667, 1243, DOI: 10.1086/520319

Gaidos, E. J., Güdel, M., & Blake, G. A. 2000, Geophys. Res. Lett., 27, 501, DOI: 10.1029/1999GL010740

Gary, D. E., & Linsky, J. L. 1981, ApJ, 250, 284, DOI: 10.1086/159373

Gary, D. E., Linsky, J. L., & Dulk, G. A. 1982, ApJ, 263, L79, DOI: 10.1086/183928

Gosling, J. T., Hildner, E., MacQueen, R. M., et al. 1976, Sol. Phys., 48, 389, DOI: 10.1007/BF00152004

Gray, R. O., Corbally, C. J., Garrison, R. F., et al. 2006, AJ, 132, 161, DOI: 10.1086/504637, eprint: astro-ph/0603770

Gray, R. O., Graham, P. W., & Hoyt, S. R. 2001a, AJ, 121, 2159, DOI: 10.1086/319957

Gray, R. O., Napier, M. G., & Winkler, L. I. 2001b, AJ, 121, 2148, DOI: 10.1086/319956

Greaves, J. S., Wyatt, M. C., Holland, W. S., & Dent, W. R. 2004, MNRAS, 351, L54, DOI: 10.1111/j.1365-2966.2004.07957.x

Güdel, M. 1992, A&A, 264, L31

—. 2002, ARA&A, 40, 217, DOI: 10.1146/annurev.astro.40.060401.093806, eprint: arXiv:astro-ph/0206436

Güdel, M., & Benz, A. O. 1993, ApJ, 405, L63, DOI: 10.1086/186766

Güdel, M., Benz, A. O., Bastian, T. S., et al. 1989, A&A, 220, L5

Güdel, M., Guinan, E. F., & Skinner, S. L. 1998, in Astronomical Society of the Pacific Conference Series, Cool Stars, Stellar Systems, and the Sun, ed. R. A. Donahue, & J. A. Bookbinder, Vol. 154, 1041

Güdel, M., Schmitt, J. H. M., & Benz, A. O. 1994, Science, 265, 933, DOI: 10.1126/science.265.5174.933

Gudel, M., Schmitt, J. H. M., Bookbinder, J. A., & Fleming, T. A. 1993, ApJ, 415, 236, DOI: 10.1086/173158

Guedel, M. 1990, A&A, 239, L1

Guedel, M., Benz, A. O., Schmitt, J. H. M., & Skinner, S. L. 1996, ApJ, 471, 1002, DOI: 10.1086/178027

Hallinan, G., Antonova, A., Doyle, J. G., et al. 2008, ApJ, 684, 644, DOI: 10.1086/590360, arXiv: 0805.4010

Hallinan, G., Bourke, S., Lane, C., et al. 2007, ApJ, 663, L25, DOI: 10.1086/519790, arXiv: 0705.2054

Hallinan, G., Littlefair, S. P., Cotter, G., et al. 2015, Nature, 523, 568, DOI: 10.1038/nature14619, arXiv: 1507.08739 [astro-ph.SR]

Harrison, R. A. 1995, A&A, 304, 585

Hawley, S. L., & Pettersen, B. R. 1991, ApJ, 378, 725, DOI: 10.1086/170474

Heintz, W. D. 1974, AJ, 79, 819, DOI: 10.1086/111614

Henry, T. J., Kirkpatrick, J. D., & Simons, D. A. 1994, AJ, 108, 1437, DOI: 10.1086/117167

Hess, S. L., & Zarka, P. 2011, A&A, 531, A29, A29, DOI: 10.1051/0004-6361/201116510

Hess, S., Cecconi, B., & Zarka, P. 2008, Geophys. Res. Lett., 35, L13107, L13107, DOI: 10.1029/2008GL033656

Hey, J. S. 1946, Nature, 157, 47, DOI: 10.1038/157047b0

Holmberg, J., Nordström, B., & Andersen, J. 2007, A&A, 475, 519, DOI: 10.1051/0004-6361:20077221, arXiv: 0707.1891

Howard, R. A. 2006, Washington DC American Geophysical Union Geophysical Monograph Series, 165, 7, DOI: 10.1029/165GM03

Jones, H. R., Pavlenko, Y., Viti, S., et al. 2005, MNRAS, 358, 105, DOI: 10.1111/j.1365-2966.2005.08736.x, eprint: astro-ph/0412387

Judge, P. G., Solomon, S. C., & Ayres, T. R. 2003, ApJ, 593, 534, DOI: 10.1086/376405

Kahler, S. W. 2013, ApJ, 769, 35, 35, DOI: 10.1088/0004-637X/769/1/35

Kaiser, M. L., Zarka, P., Kurth, W. S., Hospodarsky, G. B., & Gurnett, D. A. 2000, J. Geophys. Res., 105, 16053, DOI: 10.1029/1999JA000414

Kellett, B. J., Bingham, R., Cairns, R. A., & Tsikoudi, V. 2002, MNRAS, 329, 102, DOI: 10.1046/j.1365-8711.2002.04972.x

Kervella, P., Mérand, A., Ledoux, C., Demory, B.-O., & Le Bouquin, J.-B. 2016, ArXiv e-prints, arXiv: 1607.04351 [astro-ph.SR]

Khodachenko, M. L., Ribas, I., Lammer, H., et al. 2007, Astrobiology, 7, 167, DOI: 10.1089/ast.2006.0127

Kitchatinov, L. L., Moss, D., & Sokoloff, D. 2014, MNRAS, 442, L1, DOI: 10.1093/mnrasl/slu041, arXiv: 1401.1764 [astro-ph.SR]

Kouloumvakos, A., Nindos, A., Valtonen, E., et al. 2015, A&A, 580, A80, A80, DOI: 10.1051/0004-6361/201424397, arXiv: 1507.03776 [astro-ph.SR]

Kouloumvakos, A., Patsourakos, S., Hillaris, A., et al. 2014, Sol. Phys., 289, 2123, DOI: 10.1007/s11207-013-0460-z, arXiv: 1311.5159 [astro-ph.SR]

Kowalski, A. F., Hawley, S. L., Holtzman, J. A., Wisniewski, J. P., & Hilton, E. J. 2010, ApJ, 714, L98, DOI: 10.1088/2041-8205/714/1/L98, arXiv: 1003.3057 [astro-ph.SR]

Krucker, S., Giménez de Castro, C. G., Hudson, H. S., et al. 2013, A&A Rev., 21, 58, 58, DOI: 10.1007/s00159-013-0058-3

Kundu, M. R., Jackson, P. D., White, S. M., & Melozzi, M. 1987, ApJ, 312, 822, DOI: 10.1086/164928

Lacy, C. H., Moffett, T. J., & Evans, D. S. 1976, ApJS, 30, 85, DOI: 10.1086/190358

Lammer, H., Lichtenegger, H. I., Kulikov, Y. N., et al. 2007, Astrobiology, 7, 185, DOI: 10.1089/ast.2006.0128

Lang, K. R., Bookbinder, J., Golub, L., & Davis, M. M. 1983, ApJ, 272, L15, DOI: 10.1086/184108

Lecacheux, A., Rosolen, C., Davis, M., et al. 1993, A&A, 275, 670

Lim, J., Carilli, C. L., White, S. M., Beasley, A. J., & Marson, R. G. 1998, Nature, 392, 575, DOI: 10.1038/33352

Linsky, J. L., & Gary, D. E. 1983, ApJ, 274, 776, DOI: 10.1086/161490

Liseau, R., Montesinos, B., Olofsson, G., et al. 2013, A&A, 549, L7, L7, DOI: 10.1051/0004-6361/201220776, arXiv: 1212.3954 [astro-ph.SR]

Loukitcheva, M., Solanki, S. K., Carlsson, M., & Stein, R. F. 2004, A&A, 419, 747, DOI: 10.1051/0004-6361:20034159

MacGregor, M. A., Wilner, D. J., Rosenfeld, K. A., et al. 2013, ApJ, 762, L21, L21, DOI: 10.1088/2041-8205/762/2/L21, arXiv: 1211.5148 [astro-ph.EP]

MacQueen, R. M., Eddy, J. A., Gosling, J. T., et al. 1974, ApJ, 187, L85, DOI: 10.1086/181402

Malkin, Z. 2016, MNRAS, 461, 1937, DOI: 10.1093/mnras/stw1488, arXiv: 1603.08670 [astro-ph.IM]

Mamajek, E. E., & Hillenbrand, L. A. 2008, ApJ, 687, 1264, DOI: 10.1086/591785, arXiv: 0807.1686

Mason, B. D., Wycoff, G. L., Hartkopf, W. I., Douglass, G. G., & Worley, C. E. 2013, VizieR Online Data Catalog, 1, 2026

Massardi, M., Ekers, R. D., Murphy, T., et al. 2011, MNRAS, 412, 318, DOI: 10.1111/j.1365-2966.2010.17917.x, arXiv: 1010.5942 [astro-ph.CO]

Mellott, M. M., Huff, R. L., & Gurnett, D. A. 1986, J. Geophys. Res., 91, 13732, DOI: 10.1029/JA091iA12p13732

Melrose, D. B. 1991, ARA&A, 29, 31, DOI: 10.1146/annurev.aa.29.090191.000335

Melrose, D. B., Dulk, G. A., & Hewitt, R. G. 1984, J. Geophys. Res., 89, 897, DOI: 10.1029/JA089iA02p00897

Melrose, D. B., Dulk, G. A., & Smerd, S. F. 1978, A&A, 66, 315

Mooley, K. P., Hallinan, G., Bourke, S., et al. 2016, ApJ, 818, 105, 105, DOI: 10.3847/0004-637X/818/2/105, arXiv: 1601.01693 [astro-ph.HE]

Morin, J., Donati, J.-F., Petit, P., et al. 2008, MNRAS, 390, 567, DOI: 10.1111/j.1365-2966.2008.13809.x, arXiv: 0808.1423

Morin, J., Donati, J.-F., Petit, P., et al. 2010, MNRAS, 407, 2269, DOI: 10.1111/j.1365-2966.2010.17101.x, arXiv: 1005.5552 [astro-ph.SR]

Morosan, D. E., Zucca, P., Bloomfield, D. S., & Gallagher, P. T. 2016, A&A, 589, L8, L8, DOI: 10.1051/0004-6361/201628392, arXiv: 1604.04788 [astro-ph.SR]

Mullan, D. J., Mathioudakis, M., Bloomfield, D. S., & Christian, D. J. 2006, ApJS, 164, 173, DOI: 10.1086/502629

Murphy, T., Chatterjee, S., Kaplan, D. L., et al. 2013, PASA, 30, e006, e006, DOI: 10.1017/pasa.2012.006, arXiv: 1207.1528 [astro-ph.IM]

Murphy, T., Sadler, E. M., Ekers, R. D., et al. 2010, MNRAS, 402, 2403, DOI: 10.1111/j.1365-2966.2009.15961.x, arXiv: 0911.0002 [astro-ph.GA]

Neupert, W. M. 1968, ApJ, 153, L59, DOI: 10.1086/180220

Nita, G. M., Gary, D. E., Lanzerotti, L. J., & Thomson, D. J. 2002, ApJ, 570, 423, DOI: 10.1086/339577

Orchiston, W. 2005, Journal of Astronomical History and Heritage, 8, 3

Osten, R. A., & Bastian, T. S. 2006, ApJ, 637, 1016, DOI: 10.1086/498410, eprint: astro-ph/0509815

—. 2008, ApJ, 674, 1078, DOI: 10.1086/525013, arXiv: 0710.5881

Osten, R. A., & Wolk, S. J. 2015, ApJ, 809, 79, 79, DOI: 10.1088/0004-637X/809/1/79, arXiv: 1506.04994 [astro-ph.SR]

Panagi, P. M., & Andrews, A. D. 1995, MNRAS, 277, 423, DOI: 10.1093/mnras/277.2.423

Perley, R. A., & Butler, B. J. 2013a, ApJS, 204, 19, 19, DOI: 10.1088/0067-0049/204/2/19, arXiv: 1211.1300 [astro-ph.IM]

—. 2013b, ApJS, 206, 16, 16, DOI: 10.1088/0067-0049/206/2/16, arXiv: 1302.6662 [astro-ph.IM]

Pestalozzi, M. R., Benz, A. O., Conway, J. E., & Güdel, M. 2000, A&A, 353, 569, eprint: astro-ph/9912159

Régnier, S. 2015, A&A, 581, A9, A9, DOI: 10.1051/0004-6361/201425346, arXiv: 1507.07350 [astro-ph.SR]

Reiners, A., & Basri, G. 2007, ApJ, 656, 1121, DOI: 10.1086/510304, eprint: astro-ph/0610365

—. 2009a, A&A, 496, 787, DOI: 10.1051/0004-6361:200811450, arXiv: 0901.1659 [astro-ph.SR]

—. 2009b, A&A, 496, 787, DOI: 10.1051/0004-6361:200811450, arXiv: 0901.1659 [astro-ph.SR]

Riddle, A. C. 1970, Sol. Phys., 13, 448, DOI: 10.1007/BF00153563

Route, M. 2016, ApJ, 830, L27, L27, DOI: 10.3847/2041-8205/830/2/L27, arXiv: 1609.07761 [astro-ph.SR]

Saar, S. H., & Linsky, J. L. 1985, ApJ, 299, L47, DOI: 10.1086/184578

Scaife, A. M., & Heald, G. H. 2012, MNRAS, 423, L30, DOI: 10.1111/j.1745-3933.2012.01251.x, arXiv: 1203.0977 [astro-ph.IM]

Scalo, J., Kaltenegger, L., Segura, A. G., et al. 2007, Astrobiology, 7, 85, DOI: 10.1089/ast.2006.0125

Schmitt, J. H. M., & Liefke, C. 2004, A&A, 417, 651, DOI: 10.1051/0004-6361:20030495, eprint: arXiv:astro-ph/0308510

Scuderi, S., Panagia, N., Stanghellini, C., Trigilio, C., & Umana, G. 1998, A&A, 332, 251

Segura, A., Walkowicz, L. M., Meadows, V., Kasting, J., & Hawley, S. 2010, Astrobiology, 10, 751, DOI: 10.1089/ast.2009.0376, arXiv: 1006.0022 [astro-ph.EP]

Shulyak, D., Reiners, A., Seemann, U., Kochukhov, O., & Piskunov, N. 2014, A&A, 563, A35, A35, DOI: 10.1051/0004-6361/201322136, arXiv: 1401.5250 [astro-ph.SR]

Smith, K., Güdel, M., & Audard, M. 2005, A&A, 436, 241, DOI: 10.1051/0004-6361:20042054, eprint: astro-ph/0503022

Southworth, G. C. "Microwave Radiation from the Sun (with Erratum)", 1945, in, Classics in Radio Astronomy, 1982, ed. W. T. Sullivan III, 168

Spangler, S. R., & Moffett, T. J. 1976, ApJ, 203, 497, DOI: 10.1086/154105

Stepanov, A. V., Kliem, B., Krüger, A., Hildebrandt, J., & Garaimov, V. I. 1999, ApJ, 524, 961, DOI: 10.1086/307835

Stepanov, A. V., Kliem, B., Zaitsev, V. V., et al. 2001, A&A, 374, 1072, DOI: 10.1051/0004-6361:20010518, eprint: astro-ph/0106369

Teixeira, T. C., Kjeldsen, H., Bedding, T. R., et al. 2009, A&A, 494, 237, DOI: 10.1051/0004-6361:200810746, arXiv: 0811.3989

Thalmann, J. K., Veronig, A., & Su, Y. 2016, ApJ, 826, 143, 143, DOI: 10.3847/0004-637X/826/2/143, arXiv: 1605.03703 [astro-ph.SR]

Treumann, R. A. 2006, A&A Rev., 13, 229, DOI: 10.1007/s00159-006-0001-y

Trigilio, C., Leto, P., Umana, G., Buemi, C. S., & Leone, F. 2011, ApJ, 739, L10, L10, DOI: 10.1088/2041-8205/739/1/L10, arXiv: 1104.3268 [astro-ph.SR]

van Leeuwen, F. 2007, A&A, 474, 653, DOI: 10.1051/0004-6361:20078357, arXiv: 0708.1752

Venot, O., Rocchetto, M., Carl, S., Roshni Hashim, A., & Decin, L. 2016, ApJ, 830, 77, 77, DOI: 10.3847/0004-637X/830/2/77, arXiv: 1607.08147 [astro-ph.EP]

Vida, K., Kriskovics, L., Oláh, K., et al. 2016, A&A, 590, A11, A11, DOI: 10.1051/0004-6361/201527925, arXiv: 1603.00867 [astro-ph.SR]

Vidotto, A. A., Donati, J.-F., Jardine, M., et al. 2016, MNRAS, 455, L52, DOI: 10.1093/mnrasl/slv147, arXiv: 1509.08751 [astro-ph.SR]

Villadsen, J., Hallinan, G., Bourke, S., Güdel, M., & Rupen, M. 2014, ApJ, 788, 112, 112, DOI: 10.1088/0004-637X/788/2/112, arXiv: 1405.2341 [astro-ph.SR], URL: http://adsabs.harvard.edu/abs/2014ApJ...788..112V,

West, A. A., Hawley, S. L., Bochanski, J. J., et al. 2008, AJ, 135, 785, DOI: 10.1088/0004-6256/135/3/785, arXiv: 0712.1590

White, S. M. 2004, New Astronomy Reviews, 48, 1319, DOI: 10.1016/j.newar.2004.09.014, eprint: arXiv:astro-ph/0409157

White, S. M., Kundu, M. R., & Jackson, P. D. 1986, ApJ, 311, 814, DOI: 10.1086/164820

White, S. 2013, personal communication

Whittam, I. H., Riley, J. M., Green, D. A., et al. 2013, MNRAS, 429, 2080, DOI: 10.1093/mnras/sts478, arXiv: 1211.5300 [astro-ph.CO]

Wild, J. P., Murray, J. D., & Rowe, W. C. 1954, Australian Journal of Physics, 7, 439, DOI: 10.1071/PH540439

Wilsing, J., & Scheiner, J. 1896, Annalen der Physik, 295, 782, DOI: 10.1002/andp.18962951215

Winglee, R. M. 1985, J. Geophys. Res., 90, 9663, DOI: 10.1029/JA090iA10p09663

Wood, B. E., Müller, H.-R., Zank, G. P., Linsky, J. L., & Redfield, S. 2005, ApJ, 628, L143, DOI: 10.1086/432716, eprint: astro-ph/0506401

Wright, J. T., Marcy, G. W., Butler, R. P., & Vogt, S. S. 2004, ApJS, 152, 261, DOI: 10.1086/386283, eprint: astro-ph/0402582

Yashiro, S., & Gopalswamy, N. 2009, in IAU Symposium, Universal Heliophysical Processes, ed. N. Gopalswamy, & D. F. Webb, Vol. 257, 233, DOI: 10.1017/S1743921309029342

Zhao, G. Q., Feng, H. Q., & Wu, D. J. 2015, Physics of Plasmas, 22.10, 102105, 102105, DOI: 10.1063/1.4932325

—. 2016, Physics of Plasmas, 23.5, 052109, 052109, DOI: 10.1063/1.4948713, arXiv: 1611.04451 [physics.plasm-ph]